Alma Mater Studiorum · Università di Bologna

Scuola di Scienze

Corso di Laurea Magistrale in Fisica

Study of Cosmic Nuclei fluxes with AMS-02: implication for Dark Matter Search

Relatore:

Prof. Andrea Contin

Correlatore:

Dott. Nicolò Masi

Presentata da:

Nicoletta Belloli

Sessione II

Anno Accademico 2013/2014

Abstract

L'Alpha Magnetic Spectrometer (AMS-02) é un rivelatore per raggi cosmici (CR) progettato e costruito da una collaborazione internazionale di 56 istituti e 16 paesi ed installato il 19 Maggio del 2011 sulla Stazione Spaziale Internazionale (ISS).
Orbitando intorno alla Terra, AMS-02 sará in grado di studiare con un livello di accuratezza mai raggiunto prima la composizione dei raggi cosmici, esplorando nuove frontiere nella fisica delle particelle, ricercando antimateria primordiale ed evidenze indirette di materia oscura.
Durante il mio lavoro di tesi, ho utilizzato il software GALPROP per studiare la propagazione dei CR nella nostra Galassia attraverso il mezzo interstellare (ISM), cercando di individuare un set di parametri in grado di fornire un buon accordo con i dati preliminari di AMS-02. In particolare, mi sono dedicata all'analisi del processo di propagazione di nuclei, studiando i loro flussi e i relativi rapporti .
Il set di propagazione ottenuto dall'analisi é stato poi utilizzato per studiare ipotetici flussi da materia oscura e le possibili implicazioni per la ricerca indiretta attraverso AMS-02.

Contents

1 Introduction **3**

2 Propagation of Cosmic Rays in the Galaxy **5**

2.1 Origin of Cosmic Rays 7

2.2 Spectroscopy: Physics of Cosmic Nuclei 10

2.3 Acceleration and Propagation Mechanism 12

2.3.1 Diffusion Halo Model 18

2.3.2 Weighted Slab Model 24

2.3.3 Leaky Box Model 25

2.4 Cosmic Rays at the Top of the Atmosphere 26

3 Dark Matter Physics **30**

3.1 ΛCDM Model 31

3.1.1 Friedmann Equations 32

3.1.2 Universe Classification 33

3.1.3 Dark Matter Production in the ΛCDM Model 35

3.2 Dark Matter Candidates after the Higgs Boson Discovery 38

3.3 Dark Matter Search in Space with AMS-02 54

3.3.1 Experimental Results from PAMELA and Fermi 54

3.3.2 Indirect Dark Matter Search 55

4 AMS-02 **62**

4.1 The Experiment: Goals and Measurements 63

4.2 Transition Radiation Detector (TRD) 64

4.3 Time of Flight (TOF) 65

4.3.1 How it works 66

4.3.2 Electronics 70

4.4 The Magnet 72

4.5 Silicon Tracker 73

4.6 Ring Imaging Cherenkov (RICH) . . . 74
4.7 ECAL . . . 77
4.8 ACC, TAS and Star Tracker . . . 79

5 The GALPROP Software 82
5.1 GALPROP Model . . . 82
5.2 Galaxy Structure . . . 83
5.2.1 Galactic Source Distribution . . . 85
5.2.2 Interstellar Gas Distribution . . . 85
5.3 Galactic Magnetic Field . . . 87
5.4 Isotopic Abundances . . . 87
5.5 Propagation Equation . . . 88
5.6 Iniection Spectra and Diffusion Coefficients . . . 90
5.7 Modulation in the Heliosphere . . . 94
5.8 Dark Matter in Galprop . . . 95

6 Analysis of Nuclei Fluxes: a Comparison between Data and Theory 97
6.1 Analysis Strategy . . . 97
6.2 Choice of the Propagation Set with Galprop . . . 101
6.2.1 Galaxy Geometry and Propagation Mechanisms . . . 101
6.2.2 Spectral Indices . . . 115
6.2.3 Primary Abundances at Source . . . 121
6.2.4 Nuclear Cross Sections . . . 125
6.2.5 Solar Modulation and overall uncertainty . . . 128
6.3 Galprop Results . . . 133
6.3.1 Chi-Squared Test . . . 134
6.4 Dark Matter Physics with GALPROP and PPPC4DMID . . . 138
6.4.1 The PPPC4DMID Software . . . 143

7 Conclusion 154

Bibliography 156

Chapter 1

Introduction

I carried out my thesis project with the Bologna INFN research group, responsible for the Time of Flight (TOF), for the AMS-02 experiment (Alpha Magnetic Spectrometer).
AMS-02 is a space born detector for cosmic rays (CR), built to work as an external module of the International Space Station (ISS). It was installed on 19 May 2011 aboard of the ISS, during the flight of the mission STS-134 of the Shuttle Endeavour. The experiment is an improved version of a precedent experiment, AMS-01, which flew on board of the Shuttle Discovery on June 1998.
The main goals of the experiment are: the precision measurement of the CR fluxes and composition, the detection of possible dark matter signals and the discovery of antimatter.
During my thesis I focused on the study of CR propagation through the Interstellar Medium (ISM) up to the top of the atmosphere. The main task of my work was to identify a propagation set able to give the best fit of the AMS preliminary data and able to give some hints about the DM production, maintaining a good agreement with the avaible data.
After a brief introduction on my work, in the second chapter I will give a general description of cosmic rays propagation in the galaxy.
In the third chapter I will introduce the Dark Matter physics, discussing on the main candidates and how we can look for DM with AMS-02.
The fourth chapter is devoted to the structure of the AMS-02, highlighting the importance of each detector that composes the experiment.
In the fifth chapter I will treat in detail the software I worked with for the study of CR propagation, GALPROP, describing the tuning parameters I used for my study.
In the sixth chapter I will explain the main procedure of analysis I used for the com-

parison between data and theory for the study of nuclear fluxes and ratios, showing the fallout one can obtain on dark matter physics.
Here it was chosen to show only preliminary data for nuclei: these data are still under study by the collaboration and not yet published in an official paper.

Figure 1.1: *AMS-02 orbiting the Earth on ISS[98].*

Chapter 2

Propagation of Cosmic Rays in the Galaxy

In August 1912, Austrian physicist Victor Hess made a historic balloon flight that opened a new window on matter in the universe. As he ascended to 5300 meters, he measured the rate of ionization in the atmosphere and found that it increased to some three times that at sea level. He concluded that penetrating radiation was entering the atmosphere from above. He had discovered cosmic rays (CR). Studies of cosmic rays opened the door to a world of particles beyond the confines of the atom, indeed until the advent of high energy particle accelerators in the early 1950s, this natural radiation provided the only way to investigate the growing particle scenario. These

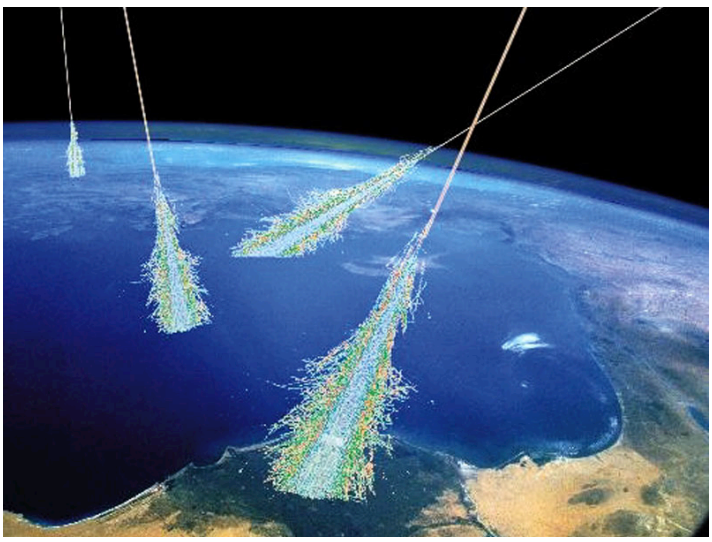

Figure 2.1: *Primary cosmic rays interaction with Earth atmosphere[4].*

high energy particles arriving from outer space are stable charge particles and nuclei, mainly (89%) protons (nuclei of hydrogen, the lightest and most common element in

the universe) but they also include nuclei of helium (10%) and other particles and heavier nuclei (1%). We can divide the CR into two type: primary cosmic rays, that are the ones accelerated by astrophysical sources, and secondary cosmic rays, the ones that are produced when the primary arrive at Earth and collide with the nuclei in the upper atmosphere, creating more particles[1]. Particles such as protons, electrons and nuclei produced in the stars (Fe, He, C, O) are primary cosmic rays, instead antiprotons, positrons and other nuclei as Li, Be and B are secondary. The energies of primary cosmic rays range for 13 order of magnitude, from around 10^8 eV (the energy of a relatively small particle accelerator) to as much as 10^{21} eV, far higher than the beam energy of the Large Hadron Collider. The rate at which these particles arrive at

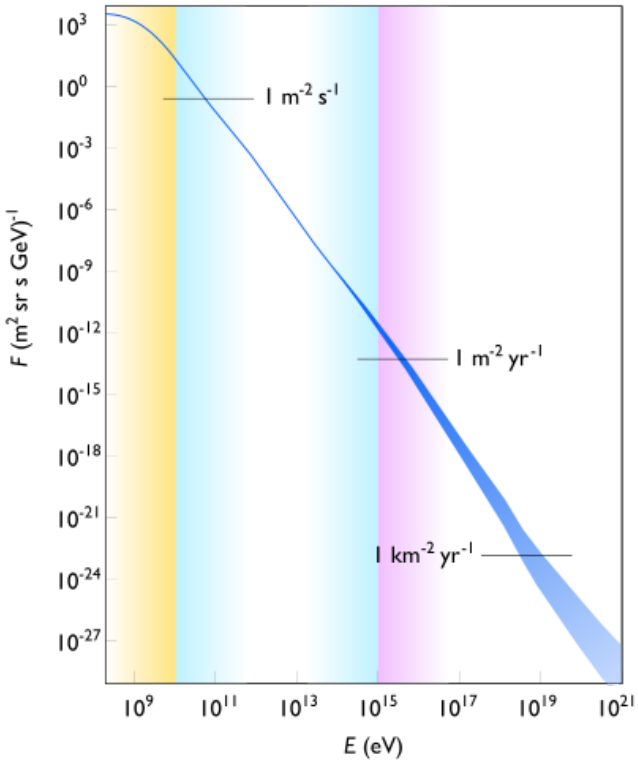

Figure 2.2: *Cosmic ray flux[4].*

the top of the atmosphere falls off with increasing energy, from about 10000 per m^2/s at 1 GeV to less than one per $km^2/century$ for the highest energy particles (see Fig. 2.2). In the highest energy region $E \simeq 10^{19}$ eV the Greisen-Zatsepin-Kuzmin (GZK) suppression is expected on the flux, due to inelastic interactions of cosmic rays with the CMB photons. The flux of cosmic rays can be described using a power law:

$$\frac{dN(\gamma)}{dE} = E^{-\gamma} \tag{2.1}$$

where N is the number of observed events, E is the primary particle energy and γ is the spectral index (≈ 2.7 for energy up to $3 \cdot 10^{15}$ eV). It varies twice, the first variation

(called *knee*) at 10^{15} and the second (called *ankle*) at 10^{19} eV. Such a dependence of the differential flux on the energy is highly constraining for propagation models and will be used in the forthcoming sections for the interpretation of a plenty of important results. In the low energy region the CR flux is modulated by the solar wind and by the Earth magnetic field effects[3]. In the following sections CR production sources, acceleration and diffusion processes along with nuclei physics will be discussed; processes involving gamma rays and neutral particles will not be considered in detail since in the present work we focused on massive charged cosmic rays.

2.1 Origin of Cosmic Rays

In this section we want to find out some quantities useful to identify possible sources for CR. The first argument is the one relative to the power needed to mantain CR in a stationary condition in the Galaxy: this power has to be compared with the one of a possible source. If we assume that the energy density is the same as the local one

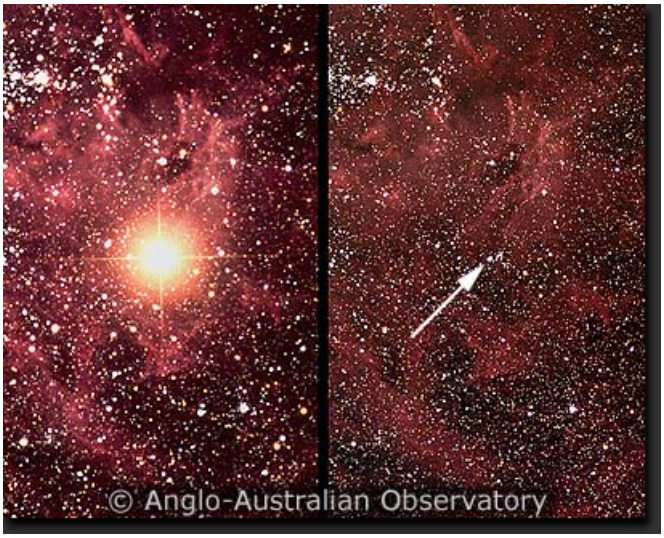

Figure 2.3: *The 1987A supernova before and after (on the left) its collapse[182].*

(namely $\rho_{IG} \simeq 1eV/cm^3$) all over the galactic disk, that the volume of the galactic disk is

$$V_D = \pi R^2 d \simeq \pi(15kpc)^2(200pc) \simeq 4 \cdot 10^{66} cm^3 \tag{2.2}$$

and that τ_R is the residence time of cosmic rays in the disk

$$\tau_R = 6 \cdot 10^6 years \tag{2.3}$$

then the power required to supply all the galactic cosmic rays turns out to be

$$P_{CR} = \frac{\rho_E V_D}{\tau_R} \simeq 5 \cdot 10^{40} erg/s \tag{2.4}$$

It has been observed along the centuries that there are about three supernovas per century, that means a mean occurrence of one every 30 years. For 10 $M_{\odot}$ ejected from a type II supernova with a velocity $v \simeq 5 \cdot 10^8 cm/s$, we figure out a total power

$$P_{SN} \simeq 3 \cdot 10^{42} erg/s \tag{2.5}$$

that, even if affected by great uncertainties, make supernovas the most plausible source of galactic cosmic rays (see Fig. 2.3). Other possible minor sources that contribute to the observed spectrum can be identified in pulsars, compact objects in close binary systems, and in stellar wind[4].

Another important aspect to keep in mind is the residence time of cosmic rays in the Galaxy, it can be estimated in the contest of the leaky box model (see Fig. 2.4) [1] to be

$$\xi = \rho_{IG} \cdot c \cdot \tau \tag{2.6}$$

$$\tau = \frac{\xi}{\rho_{IG} \cdot c} = \frac{4.8 \cdot g \cdot cm^{-2}}{1.6 \cdot 10^{-24} g \cdot cm^{-3} \cdot 3 \cdot 10^{10} cm \cdot s^{-1}} \simeq 10^6 years \tag{2.7}$$

where ξ is the mean amount of matter traversed by a CR particle (we will show how to get this value in the next section), while ρ_{IG} is the nominal disk density. Even if the

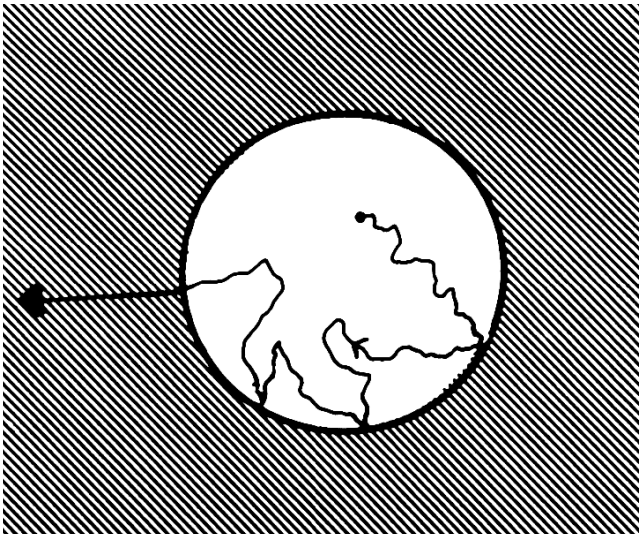

Figure 2.4: *Schematical view of the Leaky box model for the CR diffusion in the confinement volume[4].*

age of cosmic rays is longer than the resident time, a percentage of the lifetime can

[1] The *leakyboxmodel* , as will be discussed later in detail, describes the free diffusion of high energy particles in a volume and their reflection on the boundary surface that delimits the volume from the intergalactic space. For each reflection on the boundary the particle has a certain probability of escaping from the residence volume and after a time τ_e it will escape from the confinement region.

be spent in the halo, so that what is important for the above estimation of the source power requirement is the equilibrium state in the volume V_D, that is determined by the observed energy density, independently from the halo size. From an experimental point of view, the resident time can be estimated using the ratio of two isotopes: a radioactive one on a stable one (for example ^{10}Be on ^{7}Be, it is a pure secondary element and has a $\tau \simeq \tau_R$ where in this case τ is the mean life of Be and τ_R is the residence time for CR in the Galaxy).

The third quantity to study for the identification of CR origin is the chemical composition of the cosmic rays, that will be discussed in detail in the next section.

Until now we have been focused on the possible source for "low" energy CR, up to $E \simeq 10^{15}$ eV; we will see in the following that for higher energy CR new sources are necessary, indeed the SN collapse origin can supply energy up to $\simeq 10^5$ GeV, not able to explain higher energy CR present in the spectrum.

A possible candidate for CR in the range $10^{15} < E < 10^{19}$ eV is the acceleration from pulsar: a pulsar is a young neutron star that quickly turns around its axis (see Fig. 2.5). It is characterised by a density close to the nuclear one, its mass is $\simeq 1.4 M_{\odot}$,

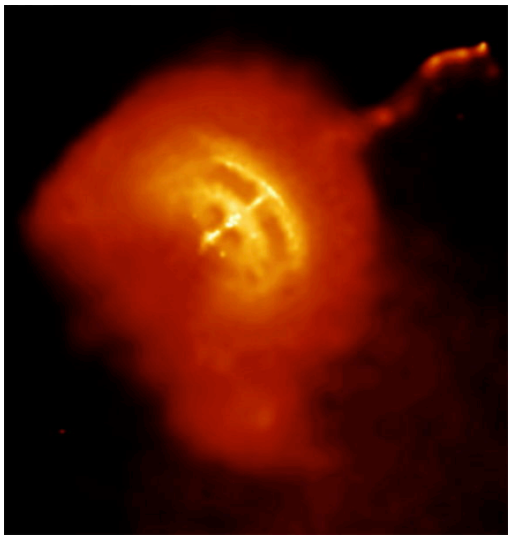

Figure 2.5: *The Vela Pulsar and its surrounding pulsar wind nebula[183].*

its radius is $\simeq 10$ Km and its magnetic field about $\simeq 10^8$ T. Pulsar can supply energy to CR using electromagnetic induction, matching different parameters, it's possible to estimate the maximum energy achievable for a unitary particle, that is $\simeq 10^{19}$ eV. It's not totally understood if the stationary CR flux can be produced by only few pulsars, for energy $10^{15} < E < 10^{19}$ eV, but what is clear is that the existence of CR with $E > 10^{19}$ needs another kind of source to be explained. These high energy cosmic rays are not confined in our Galaxy: one candidate for the production of these CR are the

active galactic nuclei or AGN (see Fig. 2.6).The AGN standard model predicts that the energy for the CR acceleration is obtained from the fall of matter into a supermassive black hole (BH), $10^6 M_{\odot} < M_{BH} < 10^{10} M_{\odot}$ [2]. When the matter fall into the BH, because of its angular momentum, an accretion disk is produced around it, the friction produced converts the matter into a plasma that moving produces a high intensity magnetic field. The final products of this process are ultrarelativistic jets of charged particles: for this reason AGN could be possible a source for high energy cosmic rays.

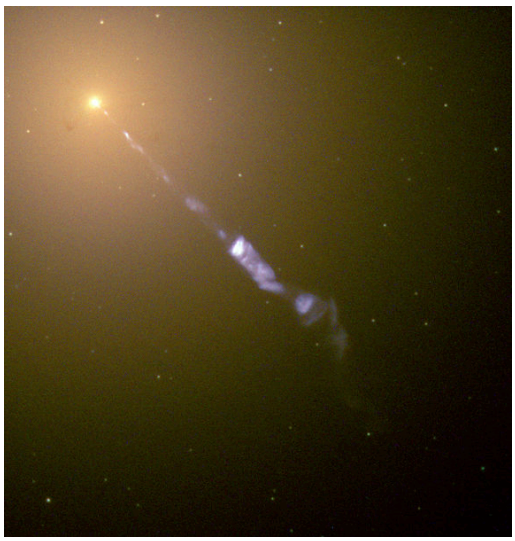

Figure 2.6: *Hubble Space Telescope image of a 5000-light year long jet being ejected from the active nucleus of the active Galaxy M87, a radio Galaxy. The blue synchrotron radiation of the jet contrasts with the yellow starlight from the host Galaxy[184].*

2.2 Spectroscopy: Physics of Cosmic Nuclei

The above considerations suggest that the main component of primary cosmic ray is represented by the material ejected during a supernova explosion (supernova remnants). It follows that CR composition should reflect the products of nuclear reactions that occur inside the stars. However this is not completely true because when a cosmic ray crosses the Galaxy, it may interact with interstellar medium and initiate a nuclear reaction [12], giving rise to a plenty of other elements: this mechanism is called spallation. This process can be studied using a model that provides the production rate of light elements (L) during the propagation of medium CR elements (M) in the Galaxy, that interact with the intersellar medium, mainly composed of protons.
The initial conditions for this model are: the mean amount of matter traversed by CR

- $\xi = \rho_{IG} l$,

the initial amount of light nuclei is 0 because they are catalysts for nucleosynthesis star reactions

- $N_L(0) = 0$,

the initial amount of medium nuclei

- $N_M(0) = N_M^0$,

the spallation probability estimated from cross sections

- $P_{M \to L} = 28\%$

The equations that describes the spallation process are:

$$\frac{dN_M(\xi)}{d\xi} = -\frac{N_M(\xi)}{\lambda_M} \tag{2.8}$$

$$\frac{dN_L}{d\xi} = -\frac{N_L(\xi)}{\lambda_L} + \frac{P_{M \to L \cdot N_M(\xi)}}{\lambda_M} \tag{2.9}$$

where $\lambda_M = \frac{1}{N_A \cdot \sigma_M} = 6\ gcm^{-2}$ and $\lambda_L = \frac{1}{N_A \cdot \sigma_L} = 8.4\ gcm^{-2}$.
Solutions for the previous equations are respectively:

$$N_M(\xi) = N_M^0 \cdot e - \frac{\xi}{\lambda_M} \tag{2.10}$$

$$N_L(\xi) = \frac{P_{M \to L}}{\lambda_M} \cdot N_M^0 (\frac{\lambda_M \cdot \lambda_L}{\lambda_L - \lambda_M})(e - \frac{\xi}{\lambda_L} - e - \frac{\xi}{\lambda_M}) \tag{2.11}$$

Using the experimental result 0.25 for the ratio $\frac{L}{M}$, we find that the mean amount of matter traversed by CR in the Galaxy (corresponding to $\frac{L}{M} = 0.25$), is $\xi = 4.8 gcm^{-2}$ (see Fig. 2.7). As a consequence of the spallation process, if we compare the elemental abundance of the Solar System with the cosmic ray elemental abundance measured at Earth, then we observe a discrepancy regarding the elements that are not final products of stellar nucleosynthesis (see Fig. 2.8). Considering the Solar System somehow representative of a typical CR source, we can see a over-abundance of cosmic rays in the Li-Be-B group ($3 \leq Z \leq 5$) as well as in the sub-Iron group ($22 \leq Z \leq 25$). Both these elemental groups are not typical products of nucleosynthesis processes [11]. From Fig. 2.9, a less pronounced odd-even effect is also observable in cosmic rays. Whereas

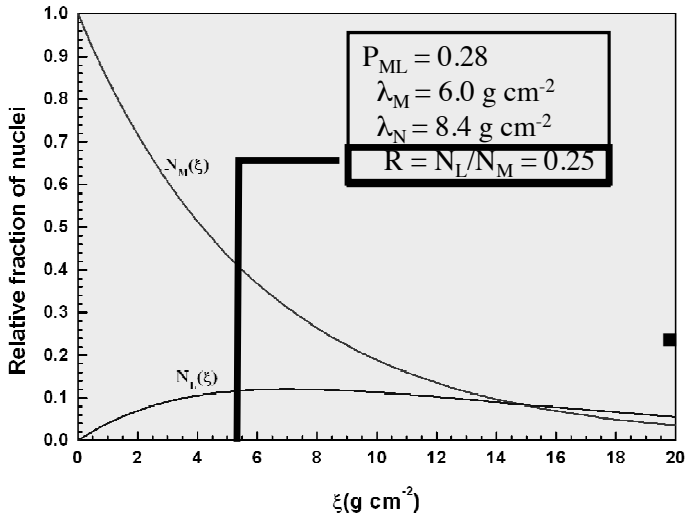

Figure 2.7: *Results for the ξ value for the mean traversed medium from the spallation model[4].*

odd-nuclei are weakly bounded and can be destroyed in the stellar thermonuclear reactions, even nuclides are much more stable and then more abundant at the source. Even-nuclei spallation can then contribute to a secondary fraction of the odd-nuclei abundance. A thorough study of this effect and the corresponding cross sections is of fundamental importance for understanding several aspects of the CR propagation. The importance of distinguishing between primary and secondary cosmic rays, resides in the possibility of connecting different type of cosmic ray to different aspects of propagation as we will deepen in the upcoming sections. In particular we will present in detail the study of nuclear ratios, that is the physics of the secondary to primary cosmic rays, such as B/C along with primary to primary, suchg as C/O. Knowing the relative abundances of the various primary and secondary nuclei, fundamental parameters for propagation models can be determined, such as the diffusion coefficient, the Alfvén speed or the convection speed, that will be defined using the Galprop software.

2.3 Acceleration and Propagation Mechanism

There are different mechanisms avaible to construct a model able to explain the cosmic rays acceleration and diffusion, such as dynamic, hydrodynamic or magnetohydrodynamic and also different possible sources for the CR production, such as stellar wind, SN explosions, SN remnants, GRB or active galactic nuclei for high energy CR. Nevertheless all the listed mechanisms and sources have to take into account the principal features associated to cosmic rays, as already mentioned i.e. the power necessary to

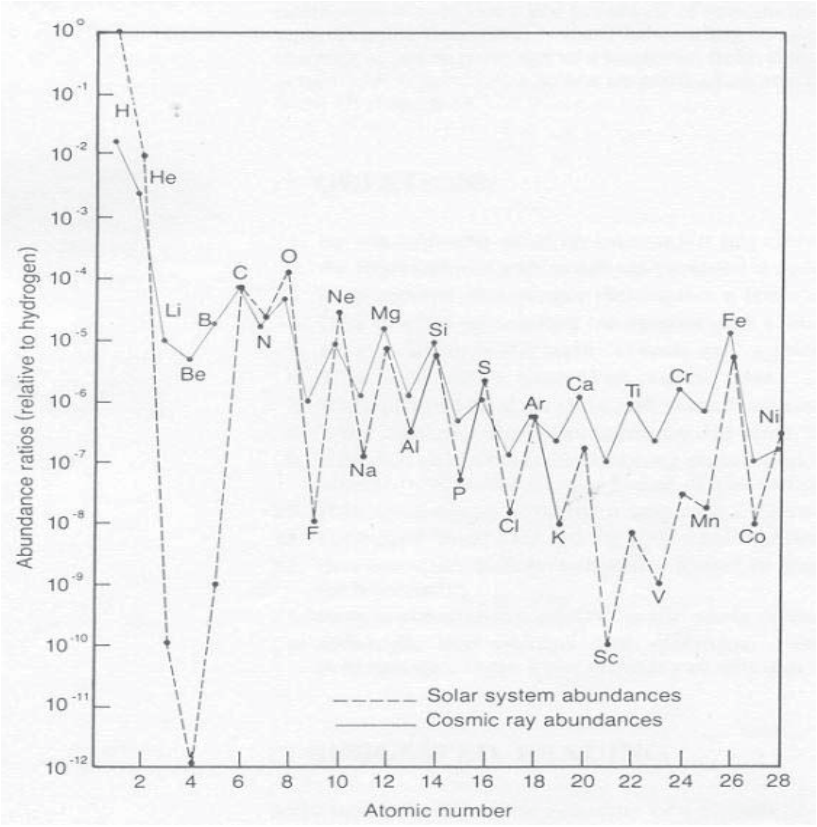

Figure 2.8: *Elemental aboundaces in the Solar System compared with cosmic rays composition[185].*

maintain CR in a stationary condition, the CR chemical composition and residence time of the cosmic rays in the Galaxy: from these parameters the source spectrum can be extrapolated.

One of the milestone for cosmic ray studies is the explanation of an effective mechanism of particle acceleration suggested by Enrico Fermi in 1949[14]. This model predicts that the CR charge particles, undergo a stochastic acceleration through continuous interactions with a shock wave (SW), a conglomerate of high density and high energy matter, produced after a SN explosion. This mechanism supplies a selective acceleration (many particles at low energy and few particles at high energy) and can explain the CR spectrum up to 10^5 GeV for higer energies other mechanism are necessary[3]. After the collapse, the shock wave undergoes a radial expansion characterized by a not relativistic velocity $V_{SW} \simeq 10^{-2}c$. In each interaction with the shock wave the CR particles raise their energy and, because of the magnetic field, they undergo circular trajectories that make them interact again and again with the SW, raising their energy each time. Let's consider two reference systems (the Laboratoy one and the SW system), and the interaction between a CR particle in the upstream region and a SW (notice that the

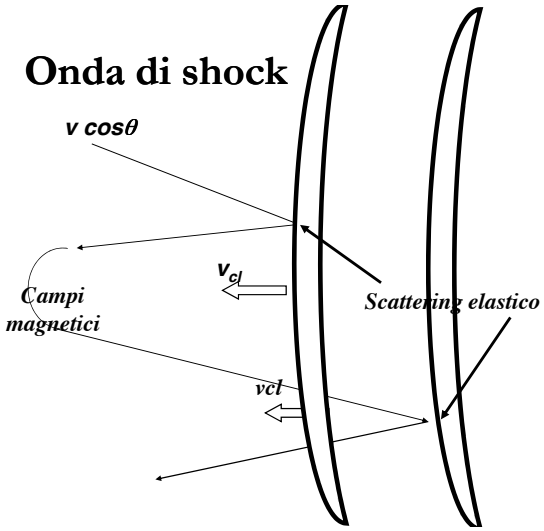

Figure 2.9: *Schematical view of a CR particle with the shock wave produced after a SN collapse[185].*

scattering in the second system is elastic), with $V_{SW} \simeq 10^{-2}c$, $M_{SW} \gg m_{CR}$: in the plane shock wave approximation, we can estimate the energy gained by the particle for each interaction (see Fig. 2.10). Using relativistic relations we obtain:

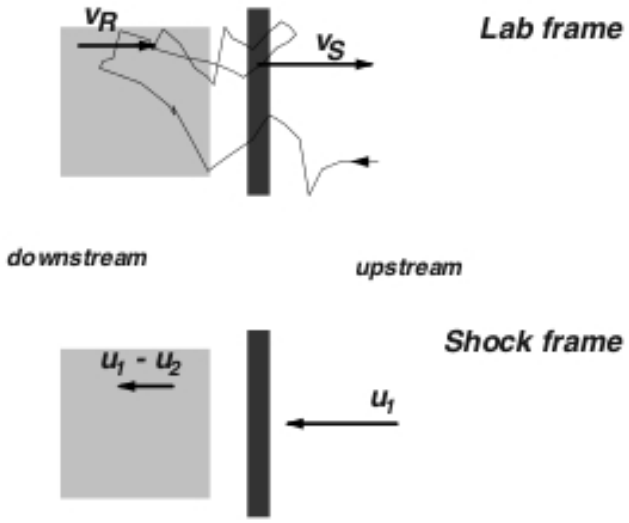

Figure 2.10: *Scattering between a CR particle and a shock wave in two reference systems[4].*

$$E' = E(1 + 2 \cdot \frac{V v \cos\theta}{c^2} + 2\frac{V^2}{c^2}) \tag{2.12}$$

where E is the particle energy before the scattering, V is the SW velocity, v is the particle velocity, c is the speed of light and $\cos\theta$ is the cosine of the angle between the particle direction and the SW direction. From this relation we can calculate the

energy gain

$$\Delta E = E' - E \simeq (2 \cdot \frac{V \cos\theta}{c}) \tag{2.13}$$

and the mean value for the ratio of final and initial energy

$$< \frac{E'}{E} >= (1 + 2 \cdot \frac{V \cos\theta}{c}) = (1 + \frac{4}{3}\frac{V}{c}) \equiv B \tag{2.14}$$

where in the last relation we substituted the cosine mean value.
We finally obtain that after a single scattering the CR particle has a mean energy

$$< E' >= B < E > \tag{2.15}$$

and a probability to remain in the upstream region P.
After K scattering the mean energy will be

$$E' = B^K \cdot E \tag{2.16}$$

and the mean number of particles will be

$$N' = P^K \cdot N \tag{2.17}$$

so that the energy distribution for the interacting particles will be

$$\frac{dN}{dE} \propto E^{\alpha-1} \equiv E^{\gamma} \tag{2.18}$$

We can write the spectral index as

$$\gamma = \alpha - 1 \equiv \frac{lnP}{lnB} - 1 \tag{2.19}$$

with

$$P = 1 - \bar{P} = 1 - \frac{F'}{F} = 1 - (\frac{\rho \cdot v_D \cdot A}{\rho \cdot c \cdot A}) \simeq 1 - (\frac{\rho \cdot V \cdot A}{\rho \cdot c \cdot A}) = 1 - \frac{V}{c} \tag{2.20}$$

where F and F' are the downstream and upstream particle fluxes.
So we finally obtain for the spectral index

$$\gamma = \frac{ln(1 - \frac{4V}{3c})}{ln(1 + \frac{4V}{3c})} - 1 \simeq \frac{-\frac{4V}{3c}}{\frac{4V}{3c}} - 1 \simeq -2 \tag{2.21}$$

from this result we can observe that the values obtained with Fermi model are in completely agreement with the experimental ones[3].
The maximum energy available from a SN with $M \simeq 10 M_{\odot}$, $\rho_{IG} \simeq 1 p/cm^3$ and $V_{SW} \simeq 10^9 cm/s$ is

$$E_{max} = Z \cdot 2.4 \cdot 10^5 GeV \tag{2.22}$$

where Z is the atomic number of the accelerating species. We observe that the achievement of this energy produces a change in the spectral index (knee). For energy higher than E_{max}, as already said, new sources have to be introduced, to make this model complete.

Until now we discussed the acceleration mechanism able to supply the characteristic energy to cosmic rays, now we want to discuss in detail which are the mechanisms that make CR moving through the Galaxy and which interactions they undergo during the propagation.
The CR propagation in the Galaxy is dominated by particle motion in the galactic magnetic field and through ionized gas that together form a magnetic-hydrodynamic fluid (MHD). Cosmic rays move in helical trajectories around the large scale field lines and interact with its small irregularities (Alfvén waves), that act as collisionless scattering centers. The galactic magnetic field extends out of the disk in a larger halo that designs the region where the diffusion takes place. Therefore a cosmic ray particle, in its travel from source to Earth, may accede to regions where the propagation conditions are different. Thus, a complete treatment of cosmic ray transport, has to consider diffusion in the full magnetic halo region. The CR propagation is generally described by a transport equation which includes source distribution, particle diffusion in the galactic magnetic field, energy losses, nuclear interactions, decays and acceleration processes. Hereafter kinetic energy per nucleon will be used (just energy for short). The most known formulation was proposed by the Ginzburg-Syrovatskii [15] with the following transport equation:

$$\frac{\partial N_j}{\partial t} = \nabla\cdot(\mathbf{D}\nabla N_j) - \nabla\cdot(\mathbf{V}_C N_j) - \frac{\partial}{\partial E_j}[b_j(E)N_j(E)] - p_j N_j + \sum_{k>j}[N_k \cdot p_{k\to j}] + Q_j(E,\mathbf{r},t) \tag{2.23}$$

Many physical processes are contained in the equation. The physical meaning for the various terms is outlined as follows:

- **CR Density**

  $N_j(E,\mathbf{r},t)$ is the density of particles of jth kind, and is defined as

  $$N_j(E,\mathbf{r},t) = \frac{1}{\nu}\int \phi_j(E,\mathbf{r},t,\hat{\omega})\cdot d\Omega \tag{2.24}$$

  Here $\phi_j(E,\mathbf{r},t,\hat{\omega})$ is the cosmic ray flux in the $\hat{\omega}$ direction and $d\Omega$ is the solid angle element.

- **Diffusion**

  The first term on the right side of the equation describes the diffusion of par-

ticles in the turbulent magnetic field. The process is governed by the diffusion coefficient D. A common simplified parametrization for the diffusion coefficient D is

$$D = \frac{1}{3}\lambda_D \nu \tag{2.25}$$

where ν is the particle velocity and λ_D is the diffusion mean free path.

- **Convection**

  The particle convection in a galactic wind with velocity V_C is described in the second right term of the equation. CR may not only diffuse in our Galaxy, they can also be carried by magnetohydrodynamic waves. The effect of this galactic wind is to dilute the energy of the particles located in the disk in a larger volume, so that the adiabatic expansion results in a kind of energy loss (adiabatic deceleration), depending on the wind velocity $V_C = V_C(t, \mathbf{r})$.

- **Energy losses**

  The third right term of the equation represents the continuous energy losses

$$b_j(E) = -\frac{dE}{dt} \tag{2.26}$$

  expresses the mean rate at which the particle j changes their energy. The only processes relevant for nuclei are ionization and Coulomb losses in ionized plasma. Other effects like bremsstrahlung, inverse Compton and synchrotron radiation are important only for light particles ($e^{\pm}$).

- **Decay and break up**

  The term $p_j N_j$ represents the destruction rate due to collision and decay with

$$p_j = n\nu\sigma_j + \frac{1}{\gamma\tau_j} \tag{2.27}$$

  where τ_j is the lifetime of nucleus j for radioactive decay. The interstellar gas (hydrogen and helium) density is parametrized with $n = n(x)$ and σ_j is the total inelastic cross section for the processes $N_j + ISM \longrightarrow anything$.

- **Spallation**

  The sum $\sum_k$ describes the production of type j nuclei from interactions of different types k nuclei. Only heavier nuclei ($k > j$) are usually considered in the sum. The process probability is also given in terms of production cross sections $\sigma_{k\to j} \equiv \sigma(N_k + ISM \longrightarrow N_j + anything)$ as

$$P_j = n\beta c\sigma_{k\to j} + \frac{1}{\gamma\tau_{k\to j}} \tag{2.28}$$

where the contribution from heavier radioactive nuclei k to the nuclear channel j is also considered. No energy migration $E_k \longrightarrow E_j$ is considered in this term, as long as kinetic energy per nucleon is conserved in spallation. This is the main reason why theoretical models use the kinetic energy per nucleon as a fundamental quantity.

- **Source distribution**
  Last term in the equation is the primary source term. In the most general case it may be time and space dependent, even though stationarity and cylindrical symmetry are often invoked to simplify the problem.

Solving the transport equation requires the complete analysis of a system of coupled equations. Together with the possibility of working out an analytical/numerical solution, an assumption that all the parameters are well known or needed to be known is mandatory, and additional assumptions have to be done for defining the boundary conditions for the equation. Hence, different models of CR propagation in the Galaxy can be represented using the equation written above, with specific boundary conditions and approximations. Three often used propagation models are presented in the following: the Diffusion Halo Model (DHM), the Weighted Slab Model (WSM) and the Leaky Box Model (LBM).

2.3.1 Diffusion Halo Model

The most realistic physical scenario for CR propagation is a diffusion model in which the diffusion-transport equation is solved by taking into consideration all the physical processes, involved together with observational physical constraints, such as cosmic rays nuclear ratios[18]. This physical constraints generally assume that cosmic ray sources are placed in the thin galactic disc, where most of the interstellar gas is located. Cosmic rays are assumed free to diffuse out, in the whole halo region, where they are able to spend considerable portion of their lifetime. Escaping the halo is also allowed and out of the considered region the CR density becomes zero. Since cosmic rays travel with relativistic speed, the long residence time requires that they cannot move rectilinear to outer space: during this period they undergo many scatterings, without loosing too much energy, and interact with gas, producing secondary particles. This way, using light nuclei ratios, we can fix some parameters and then improve the accuracy of some software (e.g. Galprop) to obtain numerical solutions for cosmic rays propagation[24,25]. As already mentioned, this model predicts a CR diffusion toward

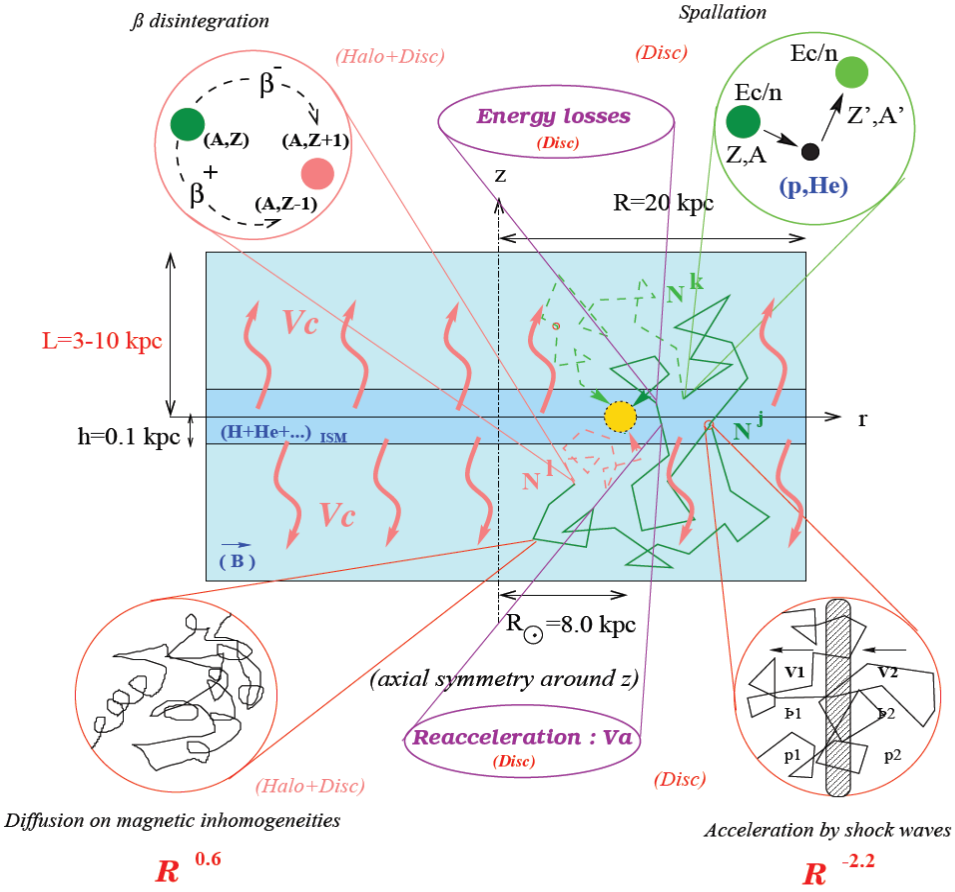

Figure 2.11: *Schematical view of the Galaxy with CR propagation steps in a diffusive halo model context[95].*

the halo, that means that there is a gradient of CR density away from the galactic disk. Consequently, a constant streaming of CR particles is produced. This streaming is determined by the energy dependence of the diffusion coefficient D(E) and the halo size.

Solutions for the transport equation,written according to this model, can be expressed using the Bessel series expansion, assuming a cylindrical symmetry for the galactic halo, as

$$\psi(E, r, z) = \sum_{i=1}^{\infty} P_i(z, E) J_0(\frac{\alpha_i r}{R}) \tag{2.29}$$

where $\phi = \frac{dN}{dE}$ is the distribution function, J_0 is the zero order Bessel function and goes to zero for α_i, P_i are the Fourier transform using cylindrical coordinates and R is the cylindrical radius. The basic quantities exploited to develop the model are explained in detail in the following:

- **Geometry of the Halo Model**:

  The exact shape and dimensions of the boundary are not know, but direct ob-

servation done using the radio halo of external galaxies, suggest that it could be considered as an infinitely thin disc ($h \simeq 100$ pc, $R \simeq 20$ kpc and $h \ll L$) containing stars and gas (90 % H and 10 % He), followed by a radially expanded halo with a greater thickness. Sources and interactions are confined to the thin disk and diffusion takes place indipendently respect to space coordinates. The Solar System is located in the galactic disk at $z = 0$ and at a distance $\simeq 8.5$ kpc from the center of the system (see Fig. 2.11).

- **Gas distribution**:
  The spatial density and composition of the interstellar gas (ISM) is a rather homogeneous mixture of hydrogen, helium, ionized gas and dust located in a narrow disk with average density of $\simeq 1\ particle/cm^3$ [17].

- **Source distribution**:
  The most common used source spatial distribution is flat (Q(r) = 1) or radial distribution $Q(r) \propto \sqrt{r} \cdot e^{1-\frac{r}{r_0}}$, with $r_0 = 8.5$ kpc. However, the difference between a flat and a radial distribution is a mere rescaling of the propagation parameter, i.e. not significant if one consider these parameters as effective in a consistent framework [18,19]. The source energy spectrum is determined by the acceleration processes at work. There is a strong belief that this spectrum is a power law in rigidity $Q(r) \propto R^{-\alpha}$.

- **Diffusion coefficient**:
  Considering an isotropic diffusion, a good approximation for the diffusion coefficient is a constant function of the space coordinates, or at least a two value function for diffusion in the disk and in the halo. Its energy dependence is usually expressed as a power law in rigidity $D = K_0 \beta R^{2-\kappa}$, where κ is the spectral index of the turbolence spectrum, K_0 is a normalization constant and $\delta = 2 - \kappa$ is a redefinition of the spectral index. The last two parameters are both related to the ISM properties and are determinated indirectly using CR observations[26].

- **Reacceleration**:
  Since in real astrophysics environment propagation can be more complex than a simple diffusion, reacceleration of CR particles can also be included. This acceleration is continuous and due to magnetic field inhomogeneities (see Fig. 2.12). The process can be studied in terms of a diffusion in momentum space, provided that the hydromagnetic turbulence may be regarded as homogeneous, and time

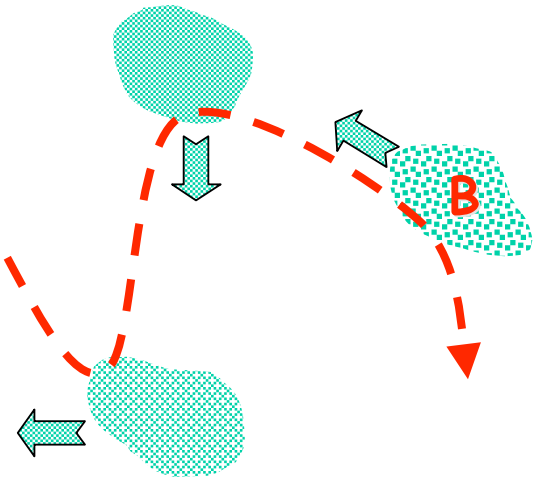

Figure 2.12: *Schematical view of the reacceleration process[186].*

independent. This involves an additional term in the transport equation:

$$\frac{1}{p^2}\frac{\partial}{\partial p}[p^2 D_{pp}\frac{\partial N_j}{\partial p}] \tag{2.30}$$

where D_{pp} is the diffusion coefficient that acts in the momentum space. If we idealize the magnetized fluid elements as hard spheres with masses much larger than those of the particles, we can write D_{pp} for elastic collisions as:

$$D_{pp} = \frac{V_a^2}{3\lambda c\beta}p^2 \tag{2.31}$$

where V_a and $c\beta$ are respectively the velocities of the fluid elements (Alfvén velocity) and particles, and λ is the mean free path against collisions with the fluid elements. The Alfvén velocity represents the velocity by which a perturbation in the magnetic field propagates along the magnetic field lines. Expressing the (spatial) diffusion coefficient as $D = \frac{1}{3}\lambda_D \nu$, a relation between D and D_{pp} can be established:

$$D_{pp} = \frac{V_a^2 p^2}{9D} \tag{2.32}$$

- **Energy losses from interaction between nuclei and ISM**:
  There are three kind of energy losses that are important for CR nuclei: Coulomb energy losses in a ionized plasma, dominated by scattering off the thermal electrons, ionization losses in the ISM neutral matter and adiabatic losses from convective (or galactic) wind. The Coulomb energy losses can be written as

$$(\frac{dE}{dt})_{coul} \approx -4\pi r_e^2 m_e c^2 Z^2 n_e ln(\Delta\frac{\beta^2}{x_m^3+\beta^3}) \tag{2.33}$$

where r_e and m_e are respectively the electron radius and mass, $n_e \simeq 0.33 cm^{-3}$ is the interstellar electron density, Z and M are charge and mass number for incoming nuclei and $ln\Delta \simeq 40 \div 50$ is the Coulomb logarithm.
The relativistic expression for ionization losses can be written as

$$(\frac{dE}{dt})_{ion} \approx -\frac{2\pi r_e^2 m_e c^3 Z^2}{\beta} \sum_{s=H,He} n_s B_s \tag{2.34}$$

where

$$B_s \equiv ln(\frac{2m_e c^2 \beta^2 \gamma^2 Q_{max}}{I_s^2}) - 2\beta^2 \tag{2.35}$$

and

$$Q_{max} \equiv \frac{2m_e c^2 \beta^2 \gamma^2}{1 + [2\gamma m_e / M]} \tag{2.36}$$

where I_s is the excitation/ionization mean potential of the considered atom, $M \gg m_e$ is the incident nucleon mass and n_s is the density of the target atom in the ISM. As already run over, among the phenomena affecting the CR propagation there's the effect induced by the medium as it moves away from the disk with a velocity V_C. This mechanism is called convective or galactic wind and its main effect is to dilute the energy of the particle located in the disk into a larger volume, this adiabatic expansion results in a third type of energy loss that depends on $\nabla \cdot V_C$. This wind, that occours only on the galactic disk, is considered to be perpendicular to the disk plane and to have a constant magnitude throughout the diffusive volume. The energy loss due to this process can be written as

$$(\frac{dE}{dt})_{adiab} = -E_k(\frac{2m + E_k}{m + E_k})\frac{V_C}{3h} \tag{2.37}$$

- **Galactic magnetic field**:
  According to radio synchrotron, optical polarization and Zeeman splitting data, the galactic magnetic field is composed of two components: a regular one with an average value of few μG that is parallel to the galactic plane and responsible for confinement, and a stochastic one which is responsible for charged nuclei diffusion and has about the same intensity as the previous one[27]. The average strength of the total magnetic field in the Milky Way is about 6 μG near the Sun and increases to 20-40 μG in the Galactic center region. The overall field structure follows the optical spiral arms and a radial distribution is a good approximation for it[17].

- **Solar modulation**:
  Cosmic rays that are detected in Earth atmosphere had to penetrate the Solar

cavity, a process by which they lose energy. This phenomenon is called Solar modulation and may be pictured as follows. The Sun emits low energy particles in the form of a fully ionized plasma having $v \simeq 400 kms^{-1}$, mainly electrons and protons with $E \simeq 0.5$ MeV. Once the plasma has left the corona, the dynamic pressure dominates over the magnetic pressure through most of the Solar System, so that the magnetic field lines are driven out by the plasma. The combination of the outflowing particles motion with the Sun's rotation leads to a spiral pattern for the flow. This Solar wind shields the Solar cavity from penetration of low energy CR. The region of space in which the solar wind is dominant is called heliosphere. The charged particles that penetrate the heliosphere are diffused and energetically influenced by the expanding solar wind. As this effect involves all the cosmic rays that are detected at Earth (or in near space), it must be taken into account. For practical purposes it can be used the force field approximation [28,29,30]. The final result of this approximation is a shift in the total energy

$$\frac{E^{TOA}}{A} = \frac{E^{IS}}{A} - \frac{|Z|\,\phi}{A} \tag{2.38}$$

where E^{TOA} is the energy at the top of the atmosphere, E^{IS} is the total interstellar energy, Z and A are respectively the charge and atomic number of the nucleus and ϕ is the solar modulation parameter, its value varies according to the eleven years solar cycle ranging between $300 \div 1500$ MV, and its determination is totally phenomenological.

- **Geomagnetic cut − off**:
  The last obstacle for cosmic rays before being detected by an Earth orbiting detector is the Earth magnetosphere, that extends its influence on the cosmic radiation modulating the low energy part of the observed spectra (up to $\simeq 15 \div 20$ GV of rigidity). To first approximation, the geomagnetic field can be represented as an offset and tilted dipole field with moment M = $8.1 \cdot 10^{25}$ $G \cdot cm^3$, an inclination of 11° to the Earth rotation axis and a displacement of about 400 km with respect to the Earth center. Because of the offset, the geomagnetic field, for a fixed altitude from the ground, is characterized by distortion, the highest of which is in the South Atlantic, where the field strength is the weakest. The charged particles penetrate deeper in this region and the radiation becomes stronger. This high radiation phenomenon (Fig. 2.13) is the so called South Atlantic Anomaly (SAA). The most important aspect for CR measurements is the determination of the geomagnetic cut-off, as it prevents CR from reaching the detector: it is maximum at the geomagnetic equator ($\simeq 15$ GV) and vanishes at

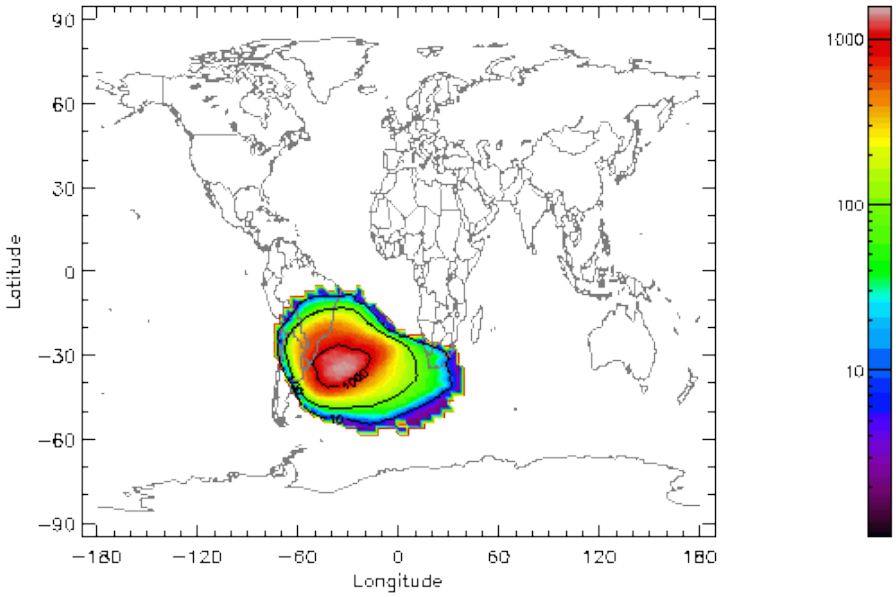

Figure 2.13: *Chromatic view of the south atlantic anomaly projected on the Earth surface, the color is related to CR rate[38].*

poles.

2.3.2 Weighted Slab Model

The principal idea of the weighted slab model is to choose a geometry for the Galaxy and to replace the time and space dependence of the fluxes in terms of matter thickness traversed [22]. In this model the abundance of a nuclear or particle species depends on the inelastic collisions between particles and ISM and on the production rate due to the spallation with heavier nuclei [3]. It is convenient to introduce the density of matter traversed by the particle $x = \rho l$, expressed in $g \cdot cm^2$ and called grammage. Nuclei of the same species with a given energy do not have necessarily the same propagation history, so that a probability distribution of grammage is associated with all the species; the function *G(x)*, called path length distribution, is then introduced. $G(x)$ is the probability that a nucleus j has crossed the grammage x. The corresponding density N_j is given by:

$$N_j = \int_0^\infty \tilde{N}_j(x) \cdot G(x)\, dx \tag{2.39}$$

where the unweighted functions $\tilde{N}_j$ are the CR densities after traversing a matter slab with thickness x. Since the grammage is directly related to the destruction rate and corresponding cross sections (total σ_j and partials σ_{kj}), the $\tilde{N}_j$ can be simply

determined from the equation:

$$\frac{d\tilde{N}_j}{dx} = \frac{1}{\bar{m}}[\sum_{k>j}(\sigma_{k\to j}N_k) - \sigma_j] \tag{2.40}$$

where $\bar{m}$ is the average ISM mass and the initial condition $\tilde{N}_j(0) = Q_j(E)$ must be imposed. In WSM framework the $G(x)$ function is derived empirically, in order to account for data, and all information on the CR propagation have then to be inferred in terms of grammage. The G(x) can also be determined through the choice of the propagation model, in this sense the WSM represents a general technique. Indeed the grammage can be used in any propagation equation (DHM, LBM) [24]. For instance, inserting Eq.(2.20) into the transport equation leads to:

$$n\beta c\frac{\partial G}{\partial x} - \nabla \cdot (D\nabla G) = f(\mathbf{r}, t) \cdot \delta(x) \tag{2.41}$$

which describes the propagation for point-like sources δ(x) spatially distributed according to $f(\mathbf{r}, t)$ (convection and energy losses are neglected here). The CR densities N_j are then given by Eq.(2.20), more precisely:

$$N_j(\mathbf{r}) = \int_0^\infty \tilde{N}_j(x) \cdot G(\mathbf{r}, x) \cdot dx \tag{2.42}$$

where the separation between the nuclear part $N_j(x)$ and the astrophysical part $G(\mathbf{r}, x)$ is apparent. This model is quite satisfactory in the high energy limit and for a particle-independent diffusion coefficient, where it becomes equivalent to the direct solution of the diffusion equation (2.21). It is also easy adaptable for every geometrical model of the Galaxy and for all spatial source distributions. The WLB allows to link Leaky Box Model (LBM) with more realistic descriptions, explaining why LBM works so well.

2.3.3 Leaky Box Model

The Leaky Box Model, introduced in the sixties and today still largely used, can be viewed as a further simplified version of the WSM, i.e. an extremely simplified version of the diffusion model. The basic assumption is that diffusion takes places rather rapidly. The distribution of cosmic rays in the whole box (i.e. Galaxy) is homogeneous, they are free to propagate in the Galaxy with a certain escape time from the system. The production rate from the sources and the escaping rate allow to maintain a stationary flux in the Galaxy[3]. Starting from the WSM formulation (Eq. 2.22), it consists in the substitutions:

$$\nabla \cdot (D\nabla N_j) \leftrightarrow \frac{N_j}{\tau_{esc}} \tag{2.43}$$

where τ_{esc} is the escape time of cosmic rays from the Galaxy, and with the average of every quantities (e.g. $n \leftrightarrow \bar{n}$). The result is the basic LBM equation:

$$\frac{\partial N_j}{\partial t} = Q_j - \frac{N_j}{\tau_{esc}} - \bar{n}\beta c\sigma_j N_j + \sum_{k>j}[\bar{n}\beta c\sigma_{k\to j} N_j] \tag{2.44}$$

The characteristic escape time τ_{esc} has to be determined experimentally and it is a purely phenomenological quantity. In this model, other energy changing processes and convection are neglected. The physical interpretation of the LBM is that cosmic rays move freely in a containment volume, with a constant probability per time unit $P = \tau_{esc}^{-1}$. The number of escaped particles per unit time is proportional to the number of particles present in the box. The other processes (decays, break up and spallation) may also be viewed in terms of characteristic times:

$$\tau_{int}^{j} = \bar{n} \cdot \beta c \cdot \sigma_j \tau_{int}^{k\to j} = \bar{n} \cdot \beta c \cdot \sigma_{k\to j} \tag{2.45}$$

For steady state solutions $\frac{dN_j}{dt} = 0$, the resulting equation system for the various nuclei j are purely algebraic:

$$\frac{N_j}{\tau_{esc}} + \frac{N_j}{\tau_{int}^{j}} = Q_j + \sum_{k>j} \frac{N_k}{\tau_{int}^{k\to j}} \tag{2.46}$$

The characteristic time τ_{esc} is often replaced by λ_{esc}, which characterizes the amount of matter traversed by CR before escaping from the ISM:

$$\lambda_{esc} = \bar{m} \cdot \bar{n} \cdot \beta c \cdot \tau_{esc} \tag{2.47}$$

where $\bar{n}$ refers to the mean interstellar gas density through which the particle penetrates, $\bar{m}$ means the mean mass of the gas, and βc is the velocity of the particle. Analogous substitutions can be done for τ_{int}^{j} and $\tau_{int}^{k\to j}$, providing the mean interaction lengths for decay or break up λ_{int}^{j} and fragmentation λ_{int}^{kj}. As these latter processes are obviously particle dependent, it should be noted that the escape time or length is the same for all the nuclear species, i.e. this formulation assumes that all nuclei have the same propagation history. Clearly this model is only an approximation which does not give indications of the main physical processes. Despite the simplicity of its physical framework, the LBM permits a direct analysis of flux measurements in function of only three fundamental parameters: the escape time, the mean matter density and the source abundances. This is largely sufficient for many purposes, because it reproduces very well the main observed features of secondary to primary CR ratios.

2.4 Cosmic Rays at the Top of the Atmosphere

At the final stage of their travel toward the Earth, cosmic rays are influenced by two local phenomena: the solar wind, which composes the heliosphere and extends up

to the boundaries of the Solar System, and the geomagnetic field, which is present in the Earth magnetosphere. Both the effects produce a distortion of the interstellar spectra measured at Earth. Two different approaches are traditionally followed by the CR physics community for these two phenomena. The solar wind influence on CR is studied by the theoretical community as well as other propagation aspects, i.e. the experimental measurements are usually presented uncorrected for this effect. Thus, low energy measurements are not representative of interstellar flux, and, since the solar wind varies with a eleven year timescale, experimental data coming from different epochs are not directly comparable unless solar modulation is accounted. On the contrary, the geomagnetic modulation is considered as part of the experimental conditions: take into account this effect is responsibility of experimentalists. Measured fluxes must therefore be corrected in order to quote the geomagnetically demodulated spectra.

The Geo Magnetic Field (GMF) extends its influence on the cosmic radiation modulating the low energy part of the observed spectra ($\leq$ 10 GeV/n). In first approximation, as already mentioned, the GMF can be represented as an offset and tilted dipole field with moment M = $8.1 \cdot 10^{25}\ G \cdot cm^3$, an inclination of 11° to the Earth rotation axis and a displacement of about 400 km with respect to the Earth center. Charged particles traversing the magnetic field experience the Lorentz force that produces a curved path for low rigidity particles. Cosmic rays can thus be prevented form reaching the detector, depending on their rigidity and incoming direction [33,35]. For a CR particle directed toward the Earth, the screening is determined by its rigidity, the detector location in the GMF and its incoming direction with respect to the field. Conversely, for given arrival direction and location, there will exist a minimum value of the particle rigidity R_C for which galactic CR are allowed to penetrate the magnetosphere and be detected. In the dipole approximation, the rigidity cut-off RC was analytically evaluated by Stormer [36] that found the relation:

$$R_C = \frac{M \cos^4 \lambda}{R_e^2[1 + (1 \pm \cos^3 \lambda \cos \phi \sin \xi)^{1/2}]^2} \tag{2.48}$$

where M is the dipole moment. The arrival direction is defined by ξ and ϕ, respectively the polar angle from local zenith and the azimuthal angle. The $\pm$ sign applies to negatively/positively charged particles. The arrival location is defined by the geomagnetic coordinates (R, λ), a commonly used coordinate system relative to the dipole axis, where R is the distance from the dipole center, usually expressed in Earth radii units ($R = r/R_\oplus$), and λ is the latitude along the dipole. These quantities come from the

simple dipole field description, where the components of the field are:

$$B_r = -\frac{M}{r^3} 2 \sin\lambda B_\lambda = \frac{M}{r^3} \cos\lambda \tag{2.49}$$

and the field lines have the form $r \propto \cos^2\lambda$. For vertical incidence ($\xi = 0$) the azimuthal dependence of the cut-off simply vanished, putting in evidence the cutoff behaviour as a function of the geomagnetic latitude:

$$R_{VC} = \frac{M}{4R^2} \cos^4\lambda \equiv \frac{M_0}{R^2} \cos^4\lambda \tag{2.50}$$

where $M_0 = 15$ if R_{VC} is measured in GV . The cut-off is maximum at the geomagnetic equator, with a value of approximately 15 GV, and vanishes at the poles. A more

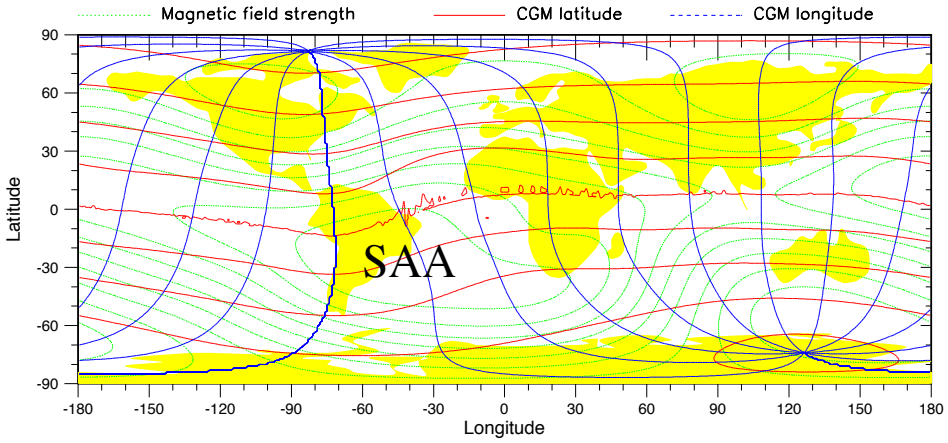

Figure 2.14: *The CGM coordinate grid projected onto the geodetic map. The green contour lines are the magnetic field strength at the Earth surface. The red (blue) lines are the magnetic latitude (longitude). The SAA region is marked[187].*

precise description of the cut-off can be obtained by replacing the dipole coordinates with the Corrected Geo Magnetic coordinates (CGM). The method consists in defining an opportune transformation $GM \leftrightarrow CGM$ that maps a more realistic GMF model into the dipole representation. The most commonly used GMF model is the IGRF one. In this picture, a rather complex magnetic field B is treated as the derivative of a scalar potential V , $B = -\nabla V$, with V expressed by a series of spherical harmonics [33]:

$$V = R_\oplus \sum_{n=0}^{\infty} (\frac{R_\oplus}{r})^{n+1} \sum_{m=0}^{n} P_n^m(\cos\theta)(g_n^m \cos m\phi + h_n^m \cos m\phi) \tag{2.51}$$

where $R_\oplus$ is the mean Earth radius $R_\oplus = 6321.2$ km, r is the geocentric radius, θ is the geographic colatitude and ϕ is the East longitude from Greenwich. $P_n^m(\cos\theta)$ are the Legendre polynomial functions, g_n^m and h_n^m are the Gaussian coefficients that

specify the GMF and are determined experimentally. The IGRF model is widely used in geophysics and contains coefficients up to order 12. The dominant terms in the last equation are related to n=1 that leads to the simple dipole field. The corresponding CGM coordinates are illustrated in Fig. 2.14. This procedure allows to use the last two equations in a IGRF framework to estimate the effective exposure time of a detector to galactic cosmic rays.

Chapter 3

Dark Matter Physics

Galaxies are gravitationally bound system made of stars, gas and dark matter, an important but poorly understood component. Here gravity is the main force so that galaxies can be studied as N-interacting body systems. According to Hubble morphological classification, galaxies can be splitted in three main groups: elliptical shape, spiral or irregular. Spiral shape galaxies are composed of two main parts: a central spherical or elliptical swelling (bulge) and the disk namely a flat asymmetric distribution of rotating material. Using the "Doppler shift" associated to absorbtion and emission lines of known electromagnetic wavelengths, one can estimate the motion along the line of sight for stars and gas in the disk with a relative velocity v. In the case of not relativistic radial velocity (v_{rad}) one can observe the wavelength λ_{obs} [57]:

$$\frac{\lambda_{obs} - \lambda_{em}}{\lambda_{em}} \simeq \frac{v_{rad}}{c} \tag{3.1}$$

Here λ_{em} is the hyperfine line emitted by the neutral hydrogen at 21 cm, associated to the transition from a spin 1 state (alignment of proton and electron spins) to a spin 0 state (opposite alignment of proton and electron spins). The main effect of rotation is the wavelength shift. If we now assume a circular orbit, the resulting rotation velocity turns out to be:

$$v_c = \frac{v_{rad} - v_s}{\sin i} \tag{3.2}$$

where v_s is Galaxy center of mass velocity and i is the angle between the line of sight and the perpendicular to the disk [57]. The variation of v_c relative to the galactic radius can be used to measure the mass profile of the Galaxy and can be expressed through a rotation curve (see Fig. 3.1). Using the centripetal acceleration definition, in the spherical case we obtain the following relation:

$$v_c^2 = \frac{GM(r)}{r} \tag{3.3}$$

where *M(r)* is the mass contained in a sphere with a radius r and G is the gravitational constant. In particular the star mass can be studied using the ratio $\frac{M}{L}$, through luminosity (L) measurements, while the gas mass can be determined through the measure of neutral hydrogen (NI). Usually in spiral galaxies the star contribution to the total mass is greater than the one from the gas, so that beyond the optic radius the above relation reduces to $v_c \propto r^{-1/2}$. However observations show that when r increases $v_c \simeq const$: this can be explained invoking the presence of a dark matter halo in the region far from the center, with a density $\rho \simeq r^{-2}$ and mass $M \propto r$, or using an alternative gravitational theory. In the first case, still considering a spiral shape Galaxy, the dark matter composition should be five to ten times the baryonic composition, in the other case we should consider a modified gravitation theory for an acceleration less then $1.2 \cdot 10^{-10}$ m/s^2.

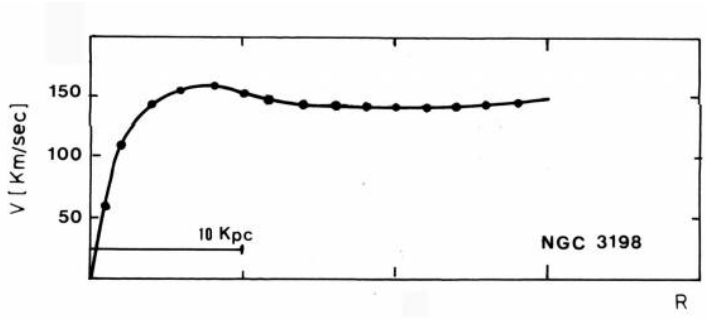

Figure 3.1: *Rotational curve for the NGC3198 galalxy. Here v_c for gas and stars is expressed in function of the distance from the center R[58].*

3.1 ΛCDM Model

Cosmology is the branch of Physics devoted to the study of Universe evolution from the Big Bang until nowadays. Cosmology is found on two main principles:

- **The Cosmological Principle**:
  according to this the Universe can be considered homogeneous and isotropic on a large scale. The Universe homogeneity can be applied only considering extended parts of it, locally this assumption is uncorrect, but it works if we consider spatial regions larger then 10^8 ly. According to actual cosmological models, Universe can be considered as an ideal fluid and each Galaxy can be located using a set of coordinates $x^\mu = (t, r, \theta, \phi)$, the quadri-velocity associated to the Galaxy is $u^\mu = (1, 0, 0, 0)$ and $u^\mu u^\nu = g_{\mu\nu} = g_{00} = 1$, here $g_{\mu\nu}$ is the metric tensor. In this model galaxies move along geodetic curves[44].

- **The Equivalence Principle**:
  according to this second principle, if we fix a point in the space-time framework and an arbitrary gravitational field, we can always find a locally inertial reference system, so that near this point physical laws are those of special relativity [44].

Choosing the first principle we can use a coordinate system (t, r, θ, ϕ), in this system the metric can be expressed as:

$$ds^2 = dt^2 - R^2(t)[\frac{dr^2}{1-kr^2} + r^2 d\theta^2 + r^2 \sin\theta^2 d\phi^2] \tag{3.4}$$

that is the Robertson-Walker metric. Here we consider $c = 1$, k is a constant with three posible values (-1,0,1), $R(t)$ is a scale factor when k=-1,0, it is the Universe radius when k=1. When k=0,-1 the Universe is considered as infinitely extended, when k=1 it is characterized by a circumference $L = 2\pi R(t)$ and a volume $V = 2\pi^2 R^3$ [39].

3.1.1 Friedmann Equations

We can obtain the Friedmann equations using the Robertson-Walker metric written above (Eq.3.4) along with the Einstein equation that can be written as follow[40]:

$$R_{\mu\nu} - \frac{1}{2} g_{\mu\nu} R = -8\pi G T_{\mu\nu} \tag{3.5}$$

where $T_{\mu\nu}$ is the energy-momentum tensor and $R_{\mu\nu}$ is the Ricci tensor i.e. the contraction between the Riemann tensor with the metric tensor. Introducing in the precedent equation the term

$$S_{\mu\nu} = (T_{\mu\nu} - \frac{1}{2} g_{\mu\nu} T^{\lambda}_{\lambda}) \tag{3.6}$$

we obtain

$$R_{\mu\nu} = -8G S_{\mu\nu} \tag{3.7}$$

In our case the energy-momentum tensor is the one for ideal fluid:

$$T_{\mu\nu} = -p(t) g_{\mu\nu} + (p(t) + \rho(t)) u_\mu u_\nu \tag{3.8}$$

here p is the fluid pressure and ρ the fluid density, both time dependent. Using this energy-momentum tensor we can rewrite $S_{\mu\nu}$ as:

$$S_{\mu\nu} = \frac{1}{2}(p - \rho) g_{\mu\nu} + (p + \rho) u_\mu u_\nu \tag{3.9}$$

Substituting the Robertson-Walker metric we obtain:

$$S_{00} = \frac{1}{2}(\rho + 3p) S_{0i} = 0 S_{ij} = \frac{1}{2}(p - \rho) R^2(t) g_{ij} \tag{3.10}$$

where $g_{ij} = 0$ when $i \neq j$, $g_{11} = (1 - kr^2)^{-1}$, $g_{22} = r^2$, $g_{33} = r^2 \sin\theta^2$. The terms in the Ricci tensor that differ from zero are

$$R_{00} = \frac{3\ddot{R}}{R} R_{0i} = 0 R_{ij} = -(R\ddot{R} + 2\ddot{R}^2 + 2k) g_{ij} \tag{3.11}$$

Combining these three relations with S_{ij} we obtain:

$$3\ddot{R} = -4\pi G(3p + \rho) R R\ddot{R} + 2\dot{R}^2 + 2k = 4\pi G(\rho - p) R^2 \tag{3.12}$$

Substituting the first in the second we finally obtain Friedmann equations:

$$\dot{R}^2 + k = \frac{8\pi G \rho R^2}{3} \frac{\ddot{R}}{R} = -\frac{4\pi G(3p + \rho)}{3} \tag{3.13}$$

Considering the conservation of the energy-momentum tensor we obtain a third equation that is:

$$\frac{d(\rho R^3)}{dR} = -3pR^2 \tag{3.14}$$

We can also introduce a useful parameter that is the Hubble constant

$$H(t) = \frac{\dot{R}}{R} \tag{3.15}$$

using it we can express the linear relation between the redshift associated to the Galaxy light emitted (z) and its distance (d):

$$cz = H_0 d \tag{3.16}$$

here H_0 is the Hubble constant and its value is $67,3 \pm 1,2$ km/s/Mpc[181].

3.1.2 Universe Classification

Let's go back to the first Friedmann equation:

$$\dot{R}^2 + k = \frac{8\pi G \rho R^2}{3} \tag{3.17}$$

if we now consider k=0, as suggested by experimental results, we obtain a value for critical density, that is:

$$\rho_c = \frac{3H^2}{8\pi G} \simeq 1,88 \cdot 10^{-29} g/cm^3 h \tag{3.18}$$

Using this critical density we can define the ratio

$$\Omega = \frac{\rho_i}{\rho_c} \tag{3.19}$$

where ρ_i is the source energy density we consider. From this relation one can obtain, by summing up the different contributions, the total amount of energy density Ω. Using Ω we can learn about the Universe curvature and distinguish between three cases[40]:

$$\Omega > \ 1 \rightarrow \rho > \ \rho_c \rightarrow k = 1 \tag{3.20}$$

$$\Omega = 1 \rightarrow \rho = \rho_c \rightarrow k = 0 \tag{3.21}$$

$$\Omega < \ 1 \rightarrow \rho < \ \rho_c \rightarrow k = -1 \tag{3.22}$$

Considering now the second Friedmann equation

$$\frac{\ddot{R}}{R} = -\frac{4\pi G(3p+\rho)}{3} \tag{3.23}$$

given that the term $(3p + \rho)$ is positive, it follows that $\ddot{R} < \ 0$ so that we can conclude the Universe to be in decelerate expansion. Nevertheless in 1999, two different and indipendent studies [40,41] highlighted that the Universe expansion is accelerated [40,41]. The theoretical way to insert in our cosmological model this expansion is to consider an additional term (Λ) in Einstein equation:

$$R_{\mu\nu} - \frac{1}{2}g_{\mu\nu}R - \Lambda g_{\mu\nu} = -8\pi G T_{\mu\nu} \tag{3.24}$$

here the new term Λ is the cosmological constant. Considering this additional contribution to the energy density we obtain

$$\Omega = \Omega_m + \Omega_\Lambda + \Omega_R + \Omega_k \tag{3.25}$$

where Ω_m is the matter density, Ω_k is the density associated to curvature and Ω_R is the radiation density. Using the cosmic microwave background radiation (CMB), some values for these densities have been determined:

$$\Omega_R \simeq 0 \tag{3.26}$$

$$\Omega_k \simeq 0 \tag{3.27}$$

$$\Omega_m \simeq 0,315 \tag{3.28}$$

$$\Omega_\Lambda \simeq 0,686 \tag{3.29}$$

so that

$$\Omega = 1,001 \tag{3.30}$$

To explain such a result, we have to introduce an extra contribution to the total energy density, that is

$$\Omega_{DM} \simeq 0,265 \tag{3.31}$$

this parameter is the dark matter energy density i.e matter different from the barionic kind that doesn't emit electromagnetic radiation, along with this term we can consider also the term connected with an exotic sort of energy, called vacuum energy density, characterized by a self gravitational equation[181].

3.1.3 Dark Matter Production in the ΛCDM Model

Starting from the Cosmological Standard Model, we can underline that all the evidences associated to dark matter come from its gravitational effects. Nevertheless what is still not completely understood is dark matter particle nature. Dark matter features have repercussions on both astrophysics (here dark matter determine galaxies and cluster structures) and particle physics[44].
In the context of ΛCDM model hyphotetical particle candidates are Weak Interactive Massive Particles (WIMP). These particles were produced in the primordial Universe and could have the adequate abundance to solve the dark matter issue. Along with this, WIMP could be useful to explain another physical issue that is the gauge hierarchy problem, connected to the Higgs mass. All fermion masses are logarithmic sensible to the Λ energy scale, beyond this energy the Standard Model doesn't work any more, on the other hand scalar masses expand as $m^2 \propto \Lambda^2$ [42]. For Higgs' particle we obtain

$$M_H^2 = M_{H_0}^2 + \Delta M_H^2 \tag{3.32}$$

here M_{H_0} stands for the tree level mass while $\Delta M_H^2 = \frac{\lambda^2 \Lambda^2}{16\pi^2}$ and λ is a dimensionless constant. In the Standard Model Λ is like $\simeq 10^{19}$ GeV and the gauge hierarchy problem seems to be difficult to solve. Nevetheless if we would consider a new sector beyond the Standard Model i.e. the SuperElectroWeak Sector, in the range 100 GeV$\div$1 TeV with $\Lambda \simeq 1$ TeV the gauge hierarchy problem would be solved, this is a strong justification for WIMP.
We want to explain in the following the thermal production mechanism for dark matter candidates in the ΛCDM model.
In its initial phase the Universe was hot and dense and all of the particles were in thermal equilibrium. In this framework WIMPs were produced in collisions between plasma particles during the radiative stage. A typical reaction involving WIMP annihilation and production is[45]:

$$\chi\bar{\chi} \leftrightarrow e^+e^-, \mu^+\mu^-, q\bar{q}, W^+W^-, ZZ, HH... \tag{3.33}$$

As long as the temperature is higher than WIMP mass, that is $kT \gg m_\chi$, particles and antiparticles have energy enough to produce $\chi\bar{\chi}$ and this reaction is in balance

with the inverse one. The production-annihilation rate is:

$$\Gamma =< sigma_{ann} v > \ n_{eq} \tag{3.34}$$

here σ_{ann} is the annihilation cross section for WIMPs, v is the relative velocity and n_{eq} is the WIMP density at chemical equilibrium.
While the Universe expansion proceeds, the temperature drops below WIMP mass and their number decreases as $e^{-\frac{m_\chi}{T}}$, only high energy particles can interact to produce WIMPs. This way WIMP number would drop rapidly below zero. On the other hand the Univere expansion proceeds and the WIMP density drops too, so that the free mean path for WIMP annihilation raise above the Hubble radius

$$d_H(t) = (\frac{\dot{R}}{R})^{-1} \tag{3.35}$$

and their annihilation stops.
The temperature corresponding to this phase is called freeze out temperature, in this conditions the number of WIMP keeps constant inside a comovent volume, this means that the WIMP density drops as the volume increases like $n \propto 1/R^3$ [44]. Considering WIMP to be coincident with its antiparticle, WIMP density should be equal to antiWIMP density so that Boltzmann equation turns out to be:

$$\frac{dn}{dt} = -3Hn - < \ \sigma_{ann} v > \ (n^2 - n_{eq}^2) \tag{3.36}$$

where n is the WIMP density and n_{eq} is the dark matter density in a thermal equilibrium condition.
The first term on right describes the density decrease as the Universe expansion proceeds, the n^2 term describes the reaction $\chi\chi \longrightarrow SMSM$ while the n_{eq}^2 term takes into account the inverse reaction $SMSM \longrightarrow \chi\chi$, where SM is a Standard Model particle. The above equation can be numerically solved and an approximated solution can be written in the following form:

$$n_f \simeq (m_\chi T_f)^{3/2} e^{-m_\chi T_f} \simeq \frac{T_f^2}{M_{pl} < \ \sigma_{ann} v >} \tag{3.37}$$

where we chose the freeze out time according to the condition $n <$
$sigma_{ann} v > = H$ and f is associated to freeze out quantities [42,45]. Let's now define the quantity $x_f = \frac{m_\chi}{T_f}$ that can be considered indipendent from dark matter properties and keep constant $x_f \simeq 20$, from it we can obtain the density Ω_χ:

$$\Omega_\chi = \frac{m_\chi n_0}{\rho_c} \simeq \frac{m_\chi T_0^3 n_f}{\rho_c T_f^3} \simeq \frac{x_f T_0^3}{\rho_c M_{pl}} (< \ \sigma_{ann} v >)^{-1} \tag{3.38}$$

where 0 stands for the value at present time. We notice that m_χ here define the scale corresponding to the annihilation cross section:

$$\sigma_{ann} v = k \frac{g^4_{weak}}{16\pi^2 m^2_\chi} v^2 \tag{3.39}$$

the final term v^2 isn't present in the S-wave reaction, $g_{weak} \simeq 0,65$ and k take into account possible deviations from this relation.

Using the above relation and fixing the k value we can observe that Ω_χ depends only on the mass m_χ. If we consider both the cases l=0 and l=1 for the angular momentum and a range $k = 1/2 \div 2$ we need a candidate mass in the range 100 GeV$\div$ 1TeV (see Figure 3.2.), this is called the *WIMP Miracle*. As will be discussed in the following in particle physics WIMPs (weakly interacting massive particles) are among the leading hypothetical particle candidates for dark matter. These particles were produced by falling out of thermal equilibrium with the hot dense plasma of the early universe. To obtain the correct abundance of dark matter a self-annihilation cross section of $< \sigma v > \simeq 3 \cdot 10^{-26} cm^3 s^{-1}$ is required, which corresponds to what is expected for a new weakly interacting particle in the 100 GeV mass range. This apparent coincidence is known as the *WIMP miracle*.

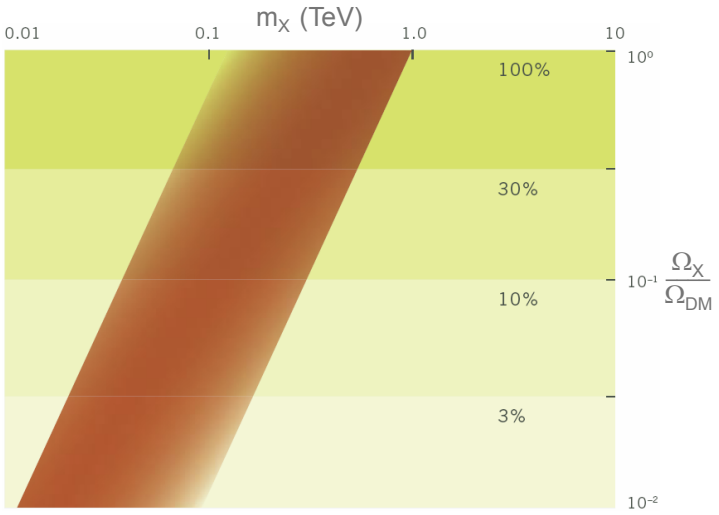

Figure 3.2: *A band of natural values in the (m_χ,Ω_χ/Ω_{DM}) plane for a thermal relic χ, where Ω_{DM} is the required total dark matter density[95].*

3.2 Dark Matter Candidates after the Higgs Boson Discovery

There is no shortage of ideas as to what the dark matter could be. In fact, the problem is the opposite. Serious candidates have been proposed with masses ranging from 10^{-5} eV (Axions) up to $10^4 M_{\odot}$ (Black holes). That's a range of masses of over 75 orders of magnitude. It should be clear that no search technique could be used for all dark matter candidates.
In this section we want to list the main characteristics of the most important dark matter candidates. We won't present in the following the Technicolor theory because of its exclusion by the discovery of the Higgs particle. For each candidate we will discuss the possibility to see it using tha Alpha Magnetic Spectrometer AMS-02. Finding a consistent categorization scheme is quite diffucult, so we will try to present each candidate without this pretense[38].

- **SUSY particles**
  It would be impossible to review in only a few pages the theory of Supersymmetry (SUSY). Instead, we prefer here to review the motivations that led to its introduction and to briefly present the concepts and the notations that we will use in the following. Furthermore, we present a few of the supersymmetric models discussed in the literature and deal with the consequences of various assumptions, involved in the process of model building, on SUSY phenomenology[38,52].
  In the Standard Model of particle physics there is a fundamental distinction between bosons and fermions: while bosons are the mediators of interactions, fermions are the constituents of matter. It is therefore natural to ask whether a symmetry exists which relates them, thus providing a sort of "unified" picture of matter and interactions. Another way to state the problem is to ask whether a Lie group exists mixing internal (Isospin, etc.) and space−time (Lorentz) symmetries[49]. Although apparently uncorrelated to the differing behaviour of bosons and fermions, this problem led to the study of the same algebraic structures. Early attempts to find a broad Lie group including the Poincaré and internal symmetry groups had to face the limitations imposed by the so called no-go theorem of Coleman and Mandula. Such limitations were finally circumvented with the introduction of graded Lie algebras, i.e. algebras involving fermionic generators satisfying anticommutation relations. For those who are not convinced by these symmetry arguments, there are other major reasons for interest in super-

symmetry. One reason is its role in understanding the hierarchy problem. The hierarchy problem is linked to the enormous difference between the electroweak and Planck energy scales. This problem arises in the radiative corrections to the mass of the Higgs boson. All particles get radiative corrections to their mass, but while fermion masses increase only logarithmically, scalar masses increase quadratically with energy, giving corrections at $1-$loop of

$$\delta m_s^2 \sim (\frac{\alpha}{2\pi})\Lambda^2 \tag{3.40}$$

where Λ is a high energy cut$-$off where new physics is expected to play an important role. The radiative corrections to the Higgs mass (which is expected to be of the order of the electroweak scale $M_W \sim 100$ GeV) will destroy the stability of the electroweak scale if Λ is higher than $\sim$TeV, e.g. if Λ is near the Planck mass. An appealing, though not the only, solution to this problem is to postulate the existence of new particles with similar masses but with spin different by one half. Then, since the contribution of fermion loops to δm_s^2 have opposite sign to the corresponding bosonic loops, at the $1-$loop level, the above relation becomes:

$$\delta m_s^2 \sim (\frac{\alpha}{2\pi})(\Lambda^2 + m_B^2) - (\frac{\alpha}{2\pi})(\Lambda^2 + m_F^2) = (\frac{\alpha}{2\pi})(m_B^2 - m_F^2) \tag{3.41}$$

Furthermore, the supersymmetric algebra insures that (provided $\mid m_B^2 - m_F^2 \mid \leq 1$ TeV) the quadratic divergence to the Higgs mass is cancelled at all orders of perturbation theory. The algebra of supersymmetry naturally guarantees the existence of new particles, with the required properties, associating to all of the particles of the Standard Model superpartners with the same mass and opposite spin type (boson or fermion)[38,56].

Another reason for interest in supersymmetric theories comes from the unification of gauge couplings at a scale $M_U \sim 2 \cdot 10^{16}$ GeV (see Fig. 3.3). Although extrapolation of the coupling constants using only Standard Model particles fails to unify them to a common value (left frame of Fig. 3.3), by introducing supersymmetry at the TeV scale, it was shown[50] that these forces naturally unify at a scale $M_U \sim 2 \cdot 10^{16}$ GeV (right frame of Fig. 3.3). This has been taken as a strong hint in favor of a Grand Unified Theory (GUT) which predicts gauge coupling unification below the Planck scale.

The new generators introduced with supersymmetry change fermions into bosons and vice versa, i.e.

$$Q \mid fermion >= \mid boson > \tag{3.42}$$

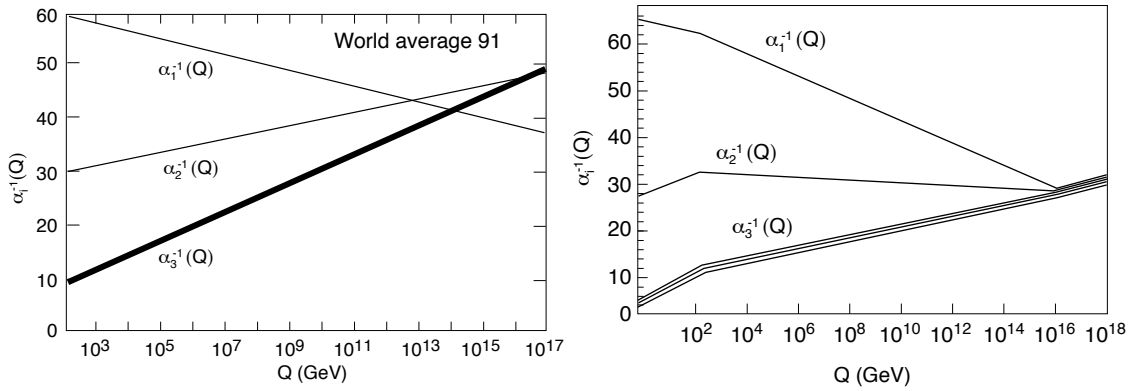

Figure 3.3: *The measurements of the gauge coupling strengths at LEP do not (left) evolve to a unified value if there is no supersymmetry but do (right) if supersymmetry is included[58].*

$$Q \mid boson >= \mid fermion > \tag{3.43}$$

Because of their fermionic nature, the operators Q must carry spin $1/2$, which implies that supersymmetry must be a spacetime symmetry. The question then arises is how to extend the Poincaré group of spatial translations and Lorentz transformations to include this new boson/fermion symmetry. The structure of such a group is highly restricted by the Haag−Lopuszanski−Sohnius extension of the Coleman and Mandula theorem cited above. For realistic theories, the operators Q, which we choose by convention to be Majorana spinors, must satisfy

$$\left\{Q_a, \bar{Q}_b\right\} = 2\gamma^\mu_{ab} P_\mu \tag{3.44}$$

$$\{Q_a, P_\mu\} = 0 \tag{3.45}$$

$$\{Q_a, M^{\mu\nu}\} = \sigma^{\mu\nu}_{ab} Q^b \tag{3.46}$$

where

$$\bar{Q}_a \equiv (Q^\dagger \gamma_0)_a \tag{3.47}$$

$$\sigma^{\mu\nu} = \frac{i}{4}[\gamma^\mu, \gamma^\nu] \tag{3.48}$$

are the structure constants of the theory[38,56]. Just as Lorentz invariance is manifest in Minkowski spacetime, supersymmetry is manifest in the so called superspace formalism, where a superspace is defined as a set of coordinates $x, \theta, \bar{\theta}$, where $x = x^\mu$ are the usual coordinate of Minkowski spacetime, and θ, $\bar{\theta}$ are anticommuting Weyl spinors. A superfield is then a function, $\Phi(x, \theta, \bar{\theta})$, defined on a superspace. It is common to introduce chiral fields representing matter and vector fields representing gauge fields.

Let's now consider the Minimal Supersymmetric extension of the Standard Model (MSSM). The MSSM is minimal in the sense that it contains the smallest possible field content necessary to give rise to all the fields of the Standard Model. This can be done as follows:

- we associate fermionic superpartners to all gauge fields. Gluons, $W^{\pm}$ and B bosons then get fermionic partners called gluinos ($\tilde{g}$), winos ($\tilde{W}^i$) and binos ($\tilde{B}$), respectively. The common name for all partners of gauge fields is the gaugino;
- we associate scalar partners to the fermions, i.e. quarks and leptons get scalar partners called squarks and sleptons;
- we introduce one additional Higgs field (for a total of two Higgs doublets, corresponding to five physical Higgs states) and associate one spin 1/2 Higgsino to each Higgs boson. This is done to give masses to both up and down-type quarks upon electroweak symmetry breaking and also preserve supersymmetry (therefore, we cannot use the conjugate of the Higgs as is done in Standard Model). Introducing another Higgs doublet also makes the theory anomaly free[38].

The resulting particle content of the theory is shown in Fig. 3.4: The MSSM is

Standard Model particles and fields		Supersymmetric partners			
		Interaction eigenstates		Mass eigenstates	
Symbol	Name	Symbol	Name	Symbol	Name
$q = d, c, b, u, s, t$	quark	$\tilde{q}_L$, $\tilde{q}_R$	squark	$\tilde{q}_1$, $\tilde{q}_2$	squark
$l = e, \mu, \tau$	lepton	$\tilde{l}_L$, $\tilde{l}_R$	slepton	$\tilde{l}_1$, $\tilde{l}_2$	slepton
$\nu = \nu_e, \nu_\mu, \nu_\tau$	neutrino	$\tilde{\nu}$	sneutrino	$\tilde{\nu}$	sneutrino
g	gluon	$\tilde{g}$	gluino	$\tilde{g}$	gluino
$W^{\pm}$	W-boson	$\tilde{W}^{\pm}$	wino	$\tilde{\chi}^{\pm}_{1,2}$	chargino
H^-	Higgs boson	$\tilde{H}^-_1$	higgsino		
H^+	Higgs boson	$\tilde{H}^+_2$	higgsino		
B	B-field	$\tilde{B}$	bino	$\tilde{\chi}^0_{1,2,3,4}$	neutralino
W^3	W^3-field	$\tilde{W}^3$	wino		
H^0_1	Higgs boson	$\tilde{H}^0_1$	higgsino		
H^0_2	Higgs boson	$\tilde{H}^0_2$	higgsino		
H^0_3	Higgs boson				

Figure 3.4: *Standard Model particles and their superpartners in the MSSM[58].*

then specified through the superpotential, defined as:

$$W = \epsilon_{ij}[y_e H_1^j L^i E^c + y_d H_1^j Q^i D^c + y_u H_2^i Q^j U^c] + \epsilon_{ij}\mu H_1^i H_2^j \tag{3.49}$$

where i and j are SU(2) indices, and y are Yukawa couplings. Color and generation indices have been suppressed in the above expression. The superpotential represents a supersymmetrization of the Standard Yukawa couplings plus a bilinear Higgs term. The superpotential enters the Lagrangian of the theory through the terms:

$$L_{SUSY} = -\frac{1}{2}(W^{ij}\psi_i\psi_j + W^*_{ij}\psi^{i\dagger}\psi^{j\dagger}) - W^i W^*_i \tag{3.50}$$

where we have used $W^i \equiv \partial W/\partial\phi_i$, $W^+_i \equiv \partial W/\partial\phi^{i*}$, and $W^{ij} \equiv \partial^2 W/\partial\phi_i\partial\phi_j$. ϕ_i and ψ_i are scalar and fermion fields, respectively. One additional ingredient of the MSSM is the conservation of R-parity. R-parity is a multiplicative quantum number defined as

$$R \equiv (-1)^{3B+L+2s} \tag{3.51}$$

All of the Standard Model particles have $R = 1$ and all sparticles (i.e. superpartners) have $R = -1$. Thus, as a consequence of R$-$parity conservation, sparticles can only decay into an odd number of sparticles (plus Standard Model particles). The lightest sparticle (dubbed the LSP, for Lightest Supersymmetric Particle) is, therefore, stable and can only be destroyed via pair annihilation, making it an excellent dark matter candidate[38,56]. The nature of the LSP in the MSSM is constrained by many observations. It cannot have a non zero electric charge or color, or it would have condensed with baryonic matter to produce heavy isotopes, in conflict with observations. Among the neutral candidates, a possibile LSP could be the sneutrino. Sneutrino LSP have, however, been excluded by direct dark matter detection experiments. Although axinos and gravitinos cannot be a prori excluded, they arise only in a subset of supersymmetric scenarios and have some unattractive properties. In particular, gravitinos and axinos have very weak interactions and would be practically impossible to detect, making them less interesting from a phenomenological perspective. The lightest neutralino remains an excellent dark matter candidate, and is further discussed in the following. To determine the identity of the LSP (or other characteristics) in a given supersymmetric scenario, we have to specify how supersymmetry is broken. If supersymmetry were not broken, then each superpartner would have a mass identical to its Standard Model counterpart, which is clearly not the case. Thus, new terms which break supersymmetry must be added to the Lagrangian. These terms, however, should be added carefully, in order not to destroy the hierarchy between Planck and electroweak scales. The possible forms for such terms are

$$L_{break} = -\frac{1}{2}M^a_\lambda\lambda^a\lambda^a - \frac{1}{2}(m^2)^i_j\phi_i\phi^{j*} - \frac{1}{2}(BM)^{ij}\phi_i\phi_j - \frac{1}{6}(Ay)^{ijk}\phi_i\phi_j\phi_k + h.c. \tag{3.52}$$

where M_λ^a are gaugino masses, m^2 are break scalar masses, B is a bilinear mass term, and A is a trilinear mass term.
As already said for dark matter, it is natural to consider all the new particles that are electrically neutral[38]:

- Gravitino $\tilde{G}$ that is a 3/2 spin fermion
- Neutralinos χ_1 ,χ_2, χ_3, χ_4 which are spin 1/2 fermions
- Sneutrinos $\tilde{\nu}_e$, $\tilde{\nu}_\mu$, $\tilde{\nu}_\tau$ which are spin 0 scalars

Among these, as already said, the most favourite is the neutralino, so let's now consider in detail this supersymmetric candidate.

The properties of each neutralino depend on their mixing, they have masses in a large range 100÷10000 GeV and couple to other particles with strengths characteristic of the weak interaction, so that they are similar to neutrinos. They are Majorana fermions not directly observable in particle detectors at accelerators. We can express neutralino through a linear combination of the four gauge sfields: Bino, Wino and Higgsinos, previously mentioned:

$$\chi = \alpha\tilde{B} + \beta\tilde{W}^3 + \gamma\tilde{H}_1 + \delta\tilde{H}_2$$

We can also introduce a mixing matrix, corresponding to the one of the Higgs sector, which mix the mass and the electroweak/supersymmetric states:

$$\begin{pmatrix} M_1 & 0 & -M_Z\cos\beta\sin\theta_W & M_Z\sin\beta\sin\theta_W \\ 0 & M_2 & M_Z\cos\beta\cos\theta_W & -M_Z\sin\beta\cos\theta_W \\ -M_Z\cos\beta\sin\theta_W & M_Z\cos\beta\cos\theta_W & 0 & -\mu \\ M_Z\sin\beta\sin\theta_W & -M_Z\sin\beta\cos\theta_W & -\mu & 0 \end{pmatrix}$$

where θ_W is the Weinberg angle, M_1 and M_2 are the bino and wino mass parameters, $\tan\beta$ is the ratio of the vacuum expectation values of the Higgs bosons while μ is the higgsino mass parameter[55]. As disclose at the beginning, here we want to discuss also the opportunity for AMS-02 to detect each of these candidate. In the neutralino case we can discuss this task introducing a parameter I_ϕ, that contains many dependeces: the discrimanation threshold between background and DM signal for AMS-02, the acceptance and the exposure time. In figure 3.5 we show three different neutralino candidates, corresponding to three different SUSY models. From this figure we can see that the most suitable detectable candidate for AMS-02 is AMSB Wino, in both positron and antiproton channel[38].

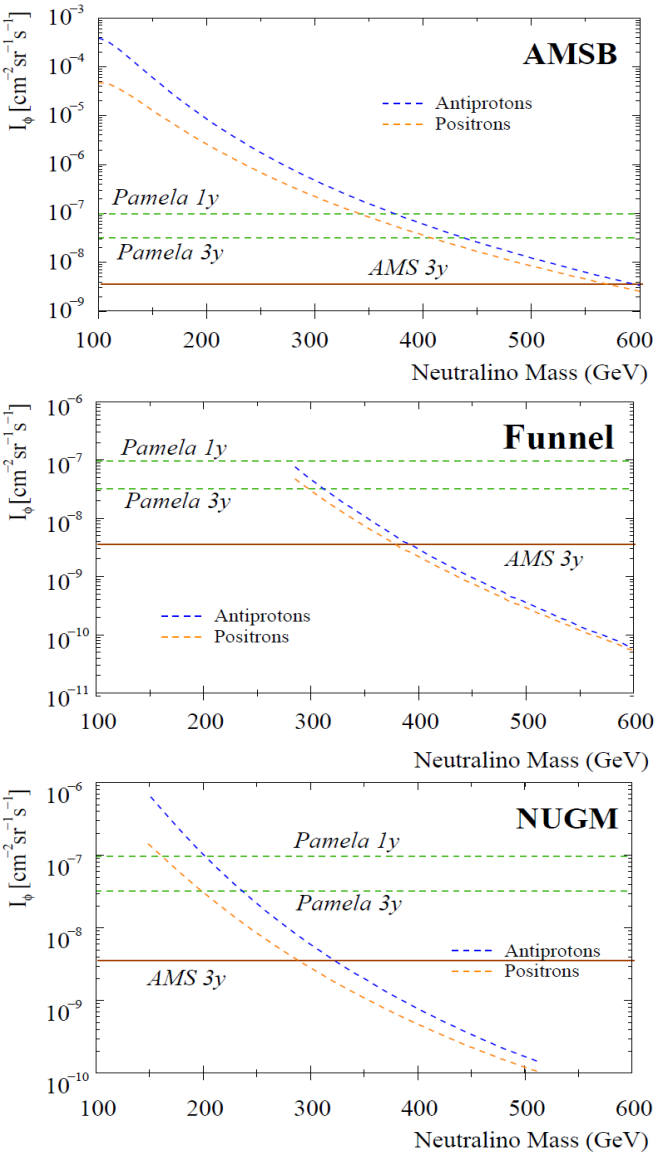

Figure 3.5: *In these plots, the I_ϕ parameter is reported as a function of the neutralino mass for three possible SUSY scenarios in both the anti-proton (dashed curve) and positron (dotdashed curve) channels. The of horizontal dashed lines represent $I_\phi^{95\%}$ for PAMELA after an operating time of one and three years. The estimate for $I_\phi^{95\%}$ of AMS in three years of data taking is the solid horizontal line[38].*

- **Kaluza-Klein particle**

  Although our world appears to consist of 3+1 (three space and one time) dimensions, it is possible that other dimensions exist and appear at higher energy scales.

  From the physics point of view, the concept of extra dimensions received great attention after the idea of Kaluza, in 1921, to unify electromagnetism with gravity by identifying the extra components of the metric tensor with the usual gauge

fields. More recently, it has been realized that the hierarchy problem could be addressed, and possibly solved, by exploiting the geometry of spacetime[38,59]. In many extra-dimensional models, the 3+1 dimensional spacetime we experience is a structure called a brane, which is embedded in a $(3 + \delta + 1)$ spacetime called the bulk. The hierarchy problem can then be solved by postulating that all of the extra dimensions are compactified on circles (or other topology) of some size, R, thus lowering the fundamental Planck scale to an energy near the electroweak scale. Alternatively, this could be accomplished by introducing extra dimensions with large curvature (warped extra dimensions). The extra dimensional scenario which we will focus on introduces flat extra dimensions which are much smaller than those in the above mentioned framework.

In addition to the hierarchy problem, motivation for the study of theories with extra dimensions comes from string theory and M−theory, which today appear to be the best candidates for a consistent theory of quantum gravity and a unified description of all interactions. It appears that such theories may require the presence of six or seven extra-dimensions.

A general feature of extra−dimensional theories is that upon compactification of the extra dimensions, all of the fields propagating in the bulk have their momentum quantized in units of $p^2 \sim 1/R^2$. The result is that for each bulk field, a set of Fourier expanded modes, called Kaluza−Klein (KK) states, appears. From our point of view in the four dimensional world, these KK states appear as a series (called a tower) of states with masses $m_n = n/R$, where n labels the mode number. Each of these new states contains the same quantum numbers, such as charge, color, etc.

In many scenarios, the Standard Model fields are assumed to be confined on the brane, with only gravity allowed to propagate in the bulk. Nevertheless, if the extra−dimensions are small, it would be possible for all fields to freely propagate in the extra dimensions. Such is the case in models with universal extra dimensions.

Scenarios in which all fields are allowed to propagate in the bulk are called Universal Extra Dimensions (UED). We note that there is significant phenomenological motivation to have all Standard Model fields propagate in the bulk, including[38]:

- motivation for three families from anomaly cancellation;
- attractive dynamical electroweak symmetry breaking;

– prevention of rapid proton decay;

– provides a viable dark matter candidate.

In the case of one extra dimension, the constraint on the compactification scale in UED models from precision electroweak measurements is as low as $R^{-1} > 300$ GeV. This is to be contrasted with another class of models where Standard Model bosons propagate in extra dimensions while fermions are localized in 4 dimensions. In such cases, the constraint on the compactification scale is much stronger, requiring $R^{-1} >$ several TeV.

The prospect of UED models providing a viable dark matter candidate is indeed what motivates us in our discussion here. The existence of a viable dark matter candidate can be seen as a consequence of the conservation of momentum in higher dimensional space. Momentum conservation in the compactified dimensions leads to the conservation of KK number. This does not stabilise the lightest KK state, however. To generate chiral fermions at the zero mode, the extra dimensions must be moded out by an orbifold, such as S/Z_2 for one extra dimension or T^2/Z_2 for two. This orbifolding results in the violating of KK number, but can leave a remnant of this symmetry called KK−parity (assuming that the boundary terms match). All odd−level KK particles are charged under this symmetry, thus ensuring that the lightest (first level) KK state is stable. In this way, the Lightest Kaluza−Klein Particle (LKP) is stabalized in a way quite analogous to the LSP in R−parity conserving supersymmetry[57].

The LKP here reconsidered in the framework of universal extra dimensions, is likely to be associated with the first KK excitation of the photon, or more precisely the first KK excitation of the hypercharge gauge boson. We will refer to this state as $B^{(1)}$[61].

A calculation of the $B^{(1)}$ relic density was performed and it was found that if the LKP is to account for the observed quantity of dark matter, its mass (which is inversely proportional to the compactification radius R) should lie in the range of $400 \div 1200$ GeV, well above any current experimental constraint.

We show in Fig. 3.6 the relic density of the $B^{(1)}$ particle versus its mass, including coannihilations with the next to lightest KK particle, which in the case shown is $e_R^{(1)}$, the first KK excitation of the right−handed electron. Note that the results of the LKP relic density calculation can vary depending on the spectrum of other first level KK states. Unlike in the case of supersymmetry, the density of KK dark matter is increased through coannihilations with other KK particles.

This is due to the fact that in the case of neutralinos, the cross section for the

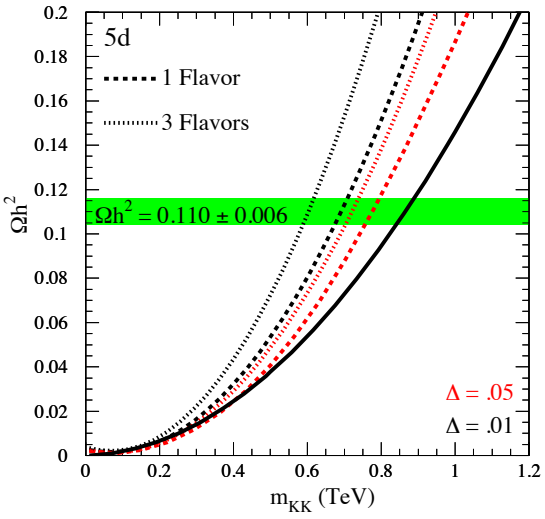

Figure 3.6: *Relic density versus mass of the $B^{(1)}$. The solid line is the case for $B^{(1)}$ alone, dashed and dotted lines are for one (three) flavors of nearly degenerate $e_R^{(1)}$. For each case, black curves (upper of each pair) are for $\Delta = 0,01$ and red curves (lower of each pair) for $\Delta = 0,05$[58].*

interaction between neutralinos and the NLSP is much larger than the neutralino self annihilation cross section, which implies that DM particles are kept longer in thermodynamic equlibrium, thus decoupling with a lower relic density. In constrast, the interactions between the $B^{(1)}$ and $e_R^{(1)}$ are comparable with the $B^{(1)}$ self-interaction. Decoupling in presence of coannihilations thus happens essentially at the same time as in the case with no coannihilations, and the $B^{(1)}$ relic density becomes larger since the $e_R^{(1)}$, after decoupling at the same time, decays in the $B^{(1)}$.

The $B^{(1)}$ annihilation cross section is given by

$$\sigma v = \frac{95 g_1^4}{324\pi m_{B^{(1)}}^2} \simeq \frac{0,6pb}{m_{B^{(1)}}^2[TeV]} \tag{3.53}$$

The branching ratios for $B^{(1)}$ annihilation are almost independent of the particle mass. Unlike in the case of supersymmetry, the bosonic nature of the LKP means that there will be no chirality suppression in its annihilations, and thus can annihilate efficiently to fermion-fermion pairs. In particular, since the annihilation cross section is proportional to hypercharge of the final state, a large fraction of LKP annihilations produce charged lepton pairs[38].

Both LKP and LZP can be detected by AMS-02 in all particle channel: positrons, antiprotons and antideuterons. Especially in the antiproton, there's the opportunity to see a sharp bump in the spectrum in the high energy range, which could

provide an important hint to DM existence.

- **Little Higgs Particle**

  In Little Higgs Models the Standard Model Higgs is considered as a pseudo-Goldstone boson, associated to a spontaneous symmetry breaking in the electroweak sector at TeV scale[38,69]. An explicit global symmetry breaking, arising from Yukawa and gauge interactions, generates the Higgs mass. In these theories, the gauge group has the form of a direct product of several copies of the same factor, for example SU(3) $\times$ SU(3). Each SU(3) factor may be visualized as the SU(2) group living at a particular point with an additional space dimension. This way many features of extra-dimensional theories may be reproduced even though the little Higgs theory is 3+1 dimensional. Two Little Higgs models contain possible dark matter candidates[69,70]. The first, called "theory space" Little Higgs models, provide a stable, scalar particle which can provide the measured density of dark matter: the detection prospects for such a candidate were found to be similar to WIMPs predicted in models of supersymmetry or universal extra dimensions. Some authors have developed other Little Higgs models, motivated by the problem of the hierarchy between the electroweak scale and the masses of new particles constrained by electroweak precision measurements. This problem is solved by introducing a new symmetry at the TeV scale which results in the existence of a stable WIMP candidate with a TeV mass. In this context, new particles have to be introduced, to solve quadratic divergences inside the Standard Model along with a new parity called T-parity[71,72]. This new quantity guarantees stability to the lightest particle for odd T-value. The most modern candidate are vector bosons which emerge from latest theories spectra and are called A_H. They're a sort of massive photons. Due to kinematic reasons and properties of the theory, the hadronic annihilation for a LTP (Lightest T-symmetry Particle) is strongly suppressed. But the positron channel (in Fig. 3.7) is very promising. Also a photon-photon annihilation is a favored process. AMS-02 can explore the parameters space of this theory, increasing our knowledge[38].

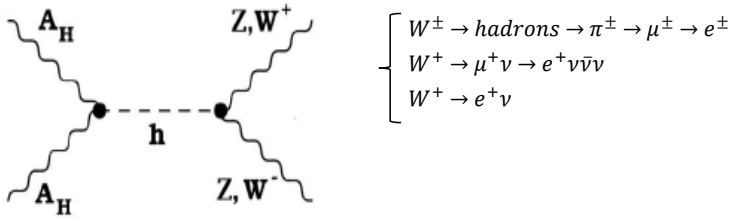

Figure 3.7: *Positron enhancement due to a Little Higgs particle decay[38].*

- **Axions**

  Introduced in an attempt to solve the problem of CP violation in particle physics, the strong CP problem, axions have also often been discussed as a dark matter candidate[57]. Experimental data seems not to indicate a CP violation in the QCD sector (strong CP problem). This is in conflict with the QCD Lagrangian that contains terms associated to weak interaction along with terms that break this symmetry:

$$L_{QCD} = -\frac{1}{4}G^a_{\mu\nu}G^{a\mu\nu} + \sum_{j=1}^{n}[\bar{q}_j\gamma^\mu iD_\mu q_j - (m_j q^\dagger_{Lj} q_{Rj} + h.c.)] + \frac{\theta g^2}{32\pi^2}G^a_{\mu\nu}\tilde{G}^{a\mu\nu} \quad (3.54)$$

  where $G^a_{\mu\nu}$ and $\tilde{G}^a_{\mu\nu}$ are the gluon field strength and its dual respectively, θ is a dimensionless parameter, whose value sets the magnitude of the effective term of the Lagrangian, q_j are color fields for quark, γ^μ are Dirac matrices, g is the coupling constant and D_μ is the covariant derivative. The CP violating term in the QCD Lagrangian is:

$$L_{CP} = \Theta\frac{g^2}{32\pi^2}G^a_{\mu\nu}\tilde{G}^{a\mu\nu} \quad (3.55)$$

  this term was introduced by Peccei and Quinn to solve the strong CP problem, and it is associated to the symmetry $U_{PQ}(1)$ that is explicitly broken by perturbing effects that make the Lagrangian θ dependent. The particle produced as a consequence of this break is the Nambu-Goldstone pseudo-boson called axion[38,95]. Laboratory searches, stellar cooling, the dynamics of supernova 1987A and cosmological observations constrain axions to be extremely light ($\sim 10^{(5\div 3)}$ eV). Furthermore, they are expected to be extremely weakly interacting with ordinary particles, which implies that they were not in thermal equilibrium in the Early Universe. The calculation of the axion relic density is uncertain, and depends on the assumptions made regarding the production mechanism. Nevertheless, it is possible to find an acceptable range where axions satisfy all present day constraints and represent a good dark matter candidate: in particular, if m_a ~ 10 μeV they could be the dominant component of DM. They're not detectable with AMS-02 but they could be good candidate. We must notice that the recent detection of B-modes by BICEP2 [179,180] has important implications for axion dark matter, though further experimental verification, coming from Planck, is required. According with these results the tensor-to-scalar ratio measurement at the end of the inflation is $r = 0.20^{+0.07}_{-0.05}$. The main consequence is that more than half of the CDM axion parameter space is no more accessible, so that many theories including axions as possible DM candiadate are ruled out[179,180].

- **Scalar Singlet**

  A simple way to explain the dark matter is the addition of a real scalar singlet and an unbroken Z_2 symmetry in the Standard Model. Such a model is called the singlet scalar model of dark matter[38,95]. This model contains only one additional field, the singlet scalar, and two new parameters: the singlet mass and the coupling between the singlet and the Higgs boson, that is the only Standard Model field that couples to it. The singlet relic density, as well as its direct and indirect detections rates, depends on the Higgs mass. After imposing the dark matter constraint, the viable parameter space gets reduced simply to the singlet mass and the now known Higgs mass. The singlet scalar model Lagrangian can be written as:

$$L = L_{SM} + \frac{1}{2}\partial_\mu S \partial^\mu S - \frac{m_0^2}{2}S^2 - \frac{\lambda_S}{4}S^4 - \lambda S^2 H^\dagger H \tag{3.56}$$

  where L_{SM} denotes the Standard Model Lagrangian, H is the Higgs doublet, and S is the singlet scalar field. AMS-02, as it's show in Fig. 3.8, could put some constraints on these theories in the antiproton channel.

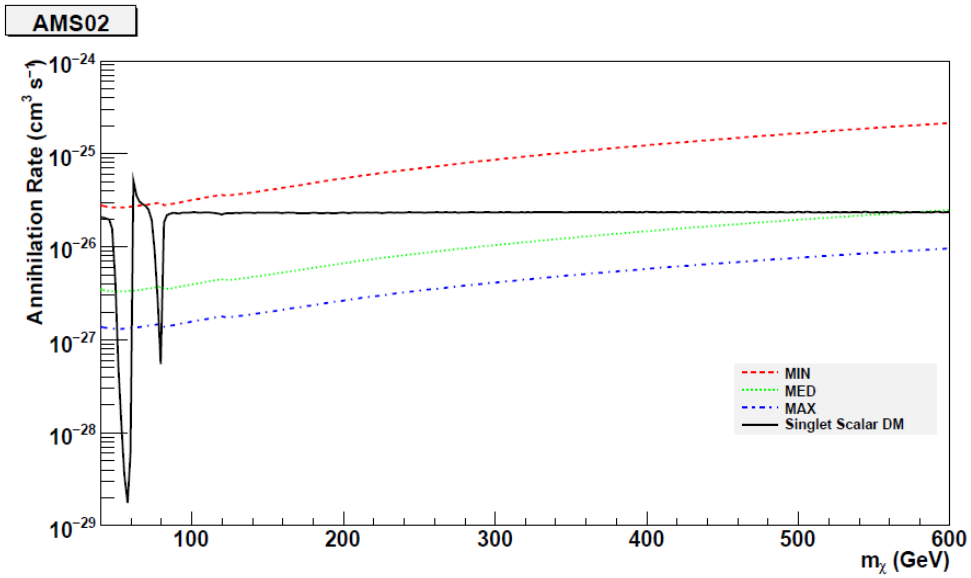

Figure 3.8: *Parameter space region accessible to AMS-02 experiment in the antiproton channel. The solid (black) line shows the prediction of the singlet model. The area above the MIN, MED, and MAX lines is detectable by AMS-02[38].*

- **Sterile neutrinos**

  These particles are similar to Standard Model neutrinos, they undergo mixing, but without Standard Model weak interactions. They were proposed as dark matter candidates in 1993 by Dodelson and Widrow[38,74]. Stringent cosmological

and astrophysical constraints on sterile neutrinos come from the analysis of their cosmological abundance and the study of their decay products. Light neutrinos, with masses below a few keV, would be ruled out as dark matter candidates. In fact, if the WMAP result for the reionization optical depth is correct, then dark matter structures were in place to form massive stars prior to redshift z $>$ 20, which is simply not possible if the dark matter particle mass is smaller than ~ 10 keV. An alternative explanation for the WMAP optical depth is reionization by decaying particles, such as sterile neutrinos[57,58]. Sterile neutrinos could also be cold dark matter, if there is a very small lepton asymmetry, in which case they are produced resonantly with a non thermal spectrum[74,75]. These particles are not detectable with AMS-02.

- **Singlino**

  In particle physics the Next to Minimal Supersymmetric Standard Model (NMSSM) is a supersymmetric extension to the Standard Model that adds an additional singlet chiral superfield[38,78]. The idea behind the Next to Minimal Supersymmetric Model is to promote the μ term, associated to the superpotential $\mu H_u H_d$, to a gauge singlet chiral superfield S. The scalar superpartner of the singlino S is denoted by $\hat{S}$ and the opposite spin singlino superpartner by $\tilde{S}$. The superpotential for the NMSSM is given by

  $$W_{NMSSM} = W_{Yuk} + \lambda S H_u H_d + \frac{\kappa}{3} S^3$$

  where W_{Yuk} gives the Yukawa couplings for the Standard Model fermions and the couplings λ and κ are dimensionless, this way the μ problem of the MSSM is solved in the NMSSM. The role of the λ term is to generate an effective μ term, $\mu_{eff} = \lambda < \hat{S} >$, where $< \hat{S} >$ is expectation value of the singlet scalar component. The role of the κ term is to break the $U(1)$ superpotential symmetry. However there remains a discrete Z_3 symmetry, which is moreover broken spontaneously. Introducing additional but suppressed terms, the Z_3 symmetry can be broken without changing phenomenology at the electroweak scale. In practice, the spin $-1/2$ singlino $\tilde{S}$ gives a fifth neutralino, compared to the four neutralinos of the MSSM. The singlino does not couple to gauge bosons, gauginos (the superpartners of the gauge bosons), leptons, sleptons (the superpartners of the leptons), quarks or squarks (the superpartners of the quarks). Supposed that a supersymmetric partner particle is produced at a collider, for instance at the LHC, the singlino is omitted in cascade decays and therefore escapes detection. However, in case the singlino is the lightest supersymmetric particle (LSP) all

supersymmetric partner particles eventually decay into the singlino. Due to R-parity conservation this LSP is stable. In this way the singlino could be detected via missing transversal energy in the detector. The "singlino−dominated" neutralino $\tilde{\chi}_S$ (in terms of mixing, for example 90% singlino and 10% Higgsino) is a light particle: in function of the parameter of the theory and of the now known Higgs mass, its mass is between 10÷160 GeV. Recent studies performed to constrain the Singlino scenario with PAMELA and WMAP data favor a very light singlino−dominated neutralino, which could produce the cosmic antiproton spectrum measured by PAMELA (but not the positron one) and has the correct cosmological properties[86]. This particle would be compatible with the circumstantial signals by CoGeNT and DAMA−LIBRA and would have a mass of 12 GeV. This is in complete disagreement with all the reasoning performed and all the empirical evidences from the entire scientific community.

- **Primordial Black Holes**

  Micro black holes are predicted as tiny black holes, also called quantum mechanical black holes or mini black holes, for which quantum mechanical effects play an important role[38]. It is possible that such quantum primordial black holes were created in the high density environment of the Early Universe, or possibly through subsequent phase transitions. They might be observed by astrophysicists in the near future, through the particles they are expected to emit by Hawking radiation (Fig. 3.9). Some theories involving additional space dimensions predict that micro black holes could be formed at an energy as low as the TeV range, which are available in particle accelerators such as the LHC. Such quantum black holes would instantly evaporate, either totally or leaving only a very weakly interacting residue. In principle, a black hole can have any mass equal to or above the Planck mass (about 22 μg). To produce a black hole, one must concentrate mass or energy sufficiently that the escape velocity from the region in which it is concentrated exceeds the speed of light. This condition gives the Schwarzschild radius, $R = \frac{2GM}{c^2}$, where G is gravitational constant and c is the speed of light, of a black hole of mass M. On the other hand, the Compton wavelength, $\lambda = \frac{h}{Mc}$, where h is Planck's constant, represents a limit on the minimum size of the region in which a mass M at rest can be localized. For sufficiently small M, the reduced Compton wavelength ($\lambda = \frac{\bar{h}}{Mc}$)exceeds half the Schwarzschild radius, and no black hole description exists. This smallest mass for a black hole is thus approximately the Planck mass. But in higher dimensional space-time, the strength of gravity increases more rapidly with decreasing distance than in

three dimensions. With certain special configurations of the extra dimensions, this effect can lower the Planck scale to the TeV scale, through the relation $M_P^2 = 8\pi M_*^2 R^2$, where M_* is the effective Planck scale and R the additional dimension lenght. In such scenarios, black hole production could possibly be an important and observable effect at the LHC. It would also be a common natural phenomenon induced by the cosmic rays[79,81]. All this assumes that the theory of General Relativity remains valid at these small distances. If it does not, then other, presently unknown effects, will limit the minimum size of a black hole. About their detectability, there are many problems. They especially produce low

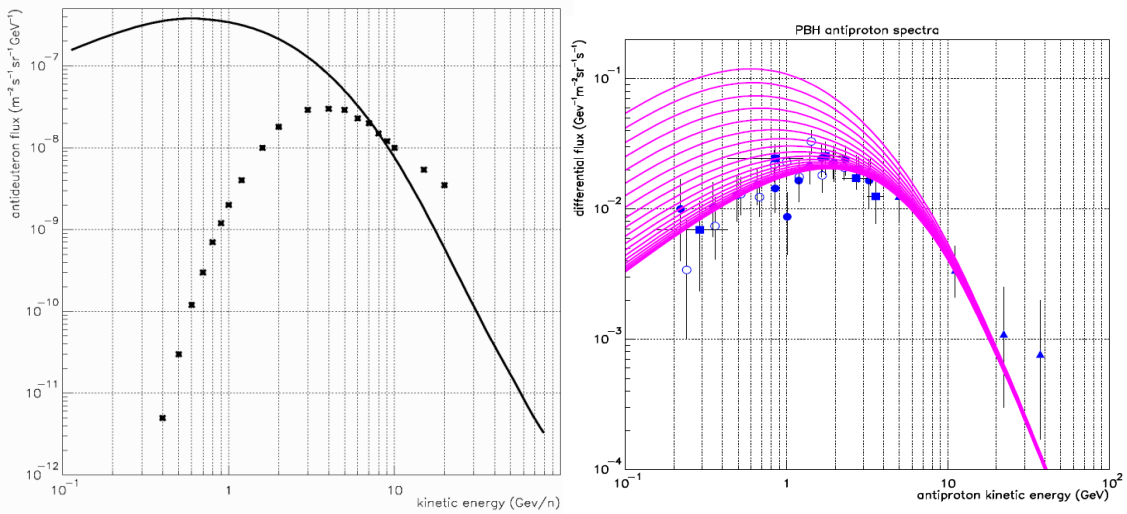

Figure 3.9: *Antideuterons (left) astrophysical spectrum (straight black line) from primordial quantum black holes. On the right, the antiprotons spectra (several parameterizations) [38].*

energy hadrons. Antiprotons production is incompatible with PAMELA's data and the antideuterons one is at the border of AMS-02 sensitivity. Furthermore CMS researches for PBH are still inconclusive. They put some high energy constraints: from CMS results at March 2012, PBH should have masses above 3.8 $\div$ 5.3 TeV, but they have seen no signal at all. Finally, sometimes also Holeums are taken into account in dark matter theoretical searches[79,82,83], which are stable, quantized gravitational bound states of primordial or micro black holes.

3.3 Dark Matter Search the Space with AMS-02

3.3.1 Experimental Results from PAMELA and Fermi

Recent results have highlighted new hints on the origin and propagation of leptonic CR component. The most important result is the one obtained by PAMELA collaboration about the positron fraction $f(E)$ [45]:

$$f(E) = \frac{1}{1 + \Phi_{e^-}/\Phi_{e^+}}$$

where Φ are positron and electron fluxes at the top of the atmosphere.
PAMELA measurement (see Fig. 3.10) shows that the positron fraction increases in the range 10 GeV $\div$ 100 GeV. A similar result has been observed by FERMI ex-

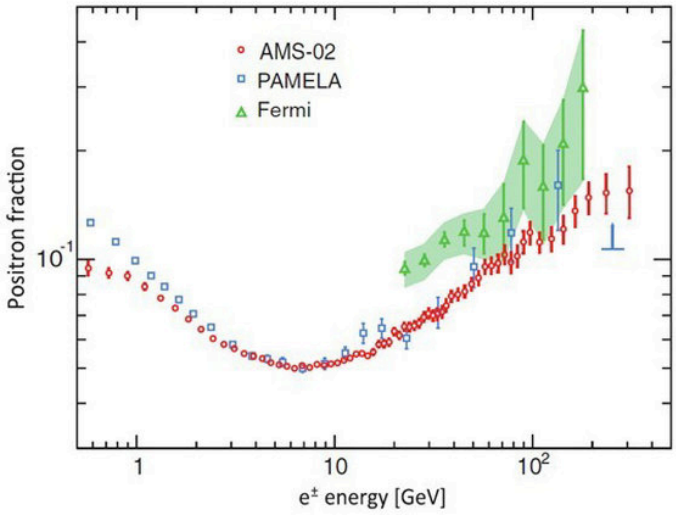

Figure 3.10: *Positron fraction excess, measured by the PAMELA experiment[98].*

periment (see Fig. 3.10). What we can infer from these results is the necessity of a primay positron source, indeed electron and positron measured fluxes differ from what theoretically expected without additional source terms. Fitting PAMELA data in the range $10 \div 100$ GeV we obtain a power law $\Phi_{e^-} \propto E^{-3,23\pm0,02}$ for electrons and $\Phi_{e^+} = E^{-2,85\pm0,06}$ for positrons. For protons we expect a theoretical flux $\Phi_p \propto E^{-2,82}$, while for positrons we expect $\Phi_{e^+} = E^{-(3,4\div E^{-3,5})}$. If these results were correct an easy way to explain them is to postulate the production by a primary source. Dark matter annihilation models can reproduce the observed excess in positron fraction. On the other hand there are other effects, associated to this primary production, which should be specified:

- we should observe a distinctive shape, that is an initial increasing signal followed by a drop corresponding to the dark matter candidate mass.

- the corresponding cross section has a high value if compared to the theorical one for wave-S annihilation process: $\sigma v \gg (\sigma v)_S \simeq 1pb$
- we should see other excesses like antiprotons, γs and neutrinos.

None of these have been observed yet.
The first problem can be solved if we consider the limited energy range accessible to PAMELA.
The second one can be treated using for the cross section the following relation:

$$< \sigma v > \simeq a + bv^2 + c\frac{1}{v} \tag{3.57}$$

where v is the relative velocity. We can justify the last term invoking the effect called Sommerfeld enhancement, which effect is presently active in our Galaxy but wasn't very influential in the primordial Universe, to not modify the WIMP production. In this way, the main annihilation is the one corresponding to S-wave but it's increased increased using Sommerfeld corrections, in the not relativistic limit[95].
The third effect, fixes some limit on dark matter mass: it seems to be within 150 GeV (see Fig. 3.11). Experimental data coming from antiprotons seem to suggest a heavier dark matter with a mass heavier than 1 TeV or a dark matter that decays only through the leptonic channel. AMS-02 could be able to solve this tension between the hadronic and leptonic channel.
We can invoke astrophysical justifications to explain PAMELA results in the leptonic channel, taking into account pulsars. Pulsars are rotating neutron stars, that induce a rather strong electric field, which is able to extract electrons from the star surface. This effect is so strong that the rotating pulsar is surrounded by a plasma called magnetosphere that extends up to a distance called 'ray of light' that can be defined as $r_l = \omega_c$ where ω is the pulsar angular velocity. This way pulsars could produce a positron$-$electron excess that could explain the experimental results without dark matter need. If this was the correct explanation we wouldn't expect any hadronic signal[95].

3.3.2 Indirect Dark Matter Search

As already said, the indirect dark matter search is based on the CR anomalous components, associated to dark matter annihilation processes in the galactic halo:

$$\chi + \chi \longrightarrow q\bar{q} + W^+W^- \longrightarrow \bar{p}, e^+, \gamma, \nu$$

Let's consider at first antiprotons as indirect dark matter signal. In this case we can introduce a source term in the transport equation, derived from four main mechanisms:

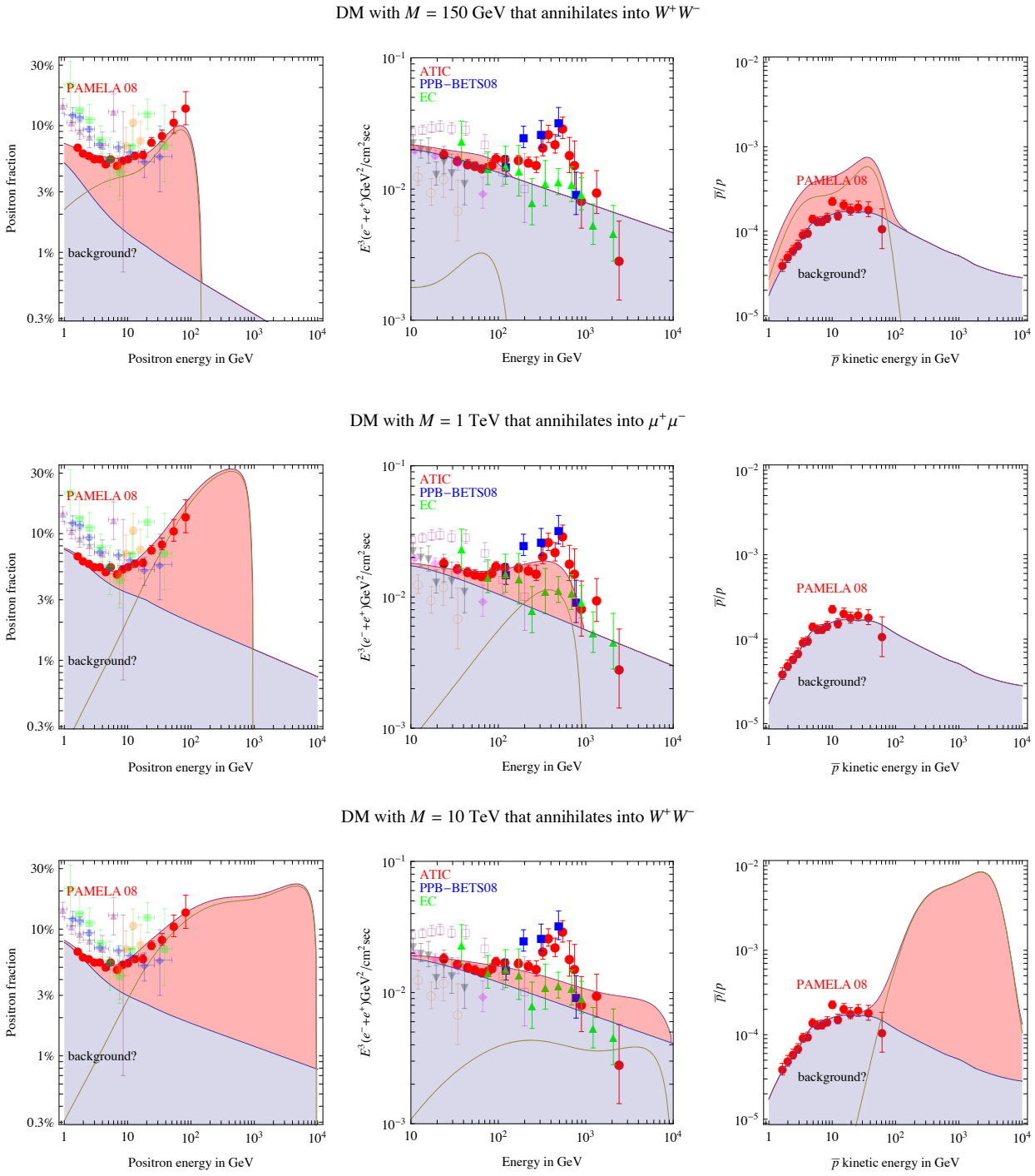

Figure 3.11: *Three examples of fits of e^+ (left), $e^+ + e^-$ (center), barp (right) data, for M =150GeV (upper row, excluded by p^-), M=1TeV (middle row, favored by data), M=10TeV (lower row, disfavored by the current e^++e^- excess). Galactic DM profiles and propagation models are varied to provide the best fit[38].*

- when high energy nuclei interact with the interstellar medium they undergo spallation process, that results in the production of secondary antiprotons;

- the dark matter candidates annihilation is a primary source for antiprotons;
- when an interaction involving a nucleon at rest occurs, the transferred energy could produce a Δ, thus modifing the spectrum [40];
- annihilation involving H or He in the interstellar medium.

The last mechanism lead to a negative term for the source i.e. $-\Gamma_{\bar{p}}^{ann}\psi$, where

$$\Gamma_{\bar{p}}^{ann} = \sigma_{\bar{p},H}^{ann}\beta_{\bar{p}}n_H + \sigma_{\bar{p},He}^{ann}\beta_{\bar{p}}n_H e \tag{3.58}$$

Here $n_{H,He}$ are Hydrogen and Helium density ($n_H \simeq 0,9\ cm^{-3}$ and $n_{He} \simeq 0,1\ cm^{-3}$ in the galactic disk), $\sigma_{\bar{p},H}^{ann}$ is the hydrogen annihilation cross section, $\sigma_{\bar{p},He}^{ann}$ is the helium annihilation cross section that can be deduced from the hydrogen one introducing a factor 2,5 [47].
The spallation contribution to the source term can be obtained assuming negligible energy loss and a reacceleration mechanism, so we can express the antiproton production rate as [40]:

$$q_{\bar{p}}^{sec} = \int_{E_{p,\alpha}^0}^{+\infty} n_{H,\alpha}\cdot\beta_{p,\alpha}\psi_{p,\alpha}(r,E_{p,\alpha})\cdot dE_{p,\alpha}\cdot\frac{d\sigma}{dE_{\bar{p}}}(E_{p,\alpha}\longrightarrow E_{\bar{p}}) \tag{3.59}$$

where, as usual, n is the density, σ the cross section and E is the energy. Here we consider the interaction between cosmic protons and α nuclei and Hydrogen and Helium interstellar nuclei, integrating from a minimal energy up to infinity and considering only antiproton sources in the intergalactic disk. Starting from the obtained interstellar fluxes, taking into account the Sun position, we can correct for the solar wind effect. Using the force field approximation we can express fluxes at the top of the atmosphere as:

$$\frac{\phi^{TOA}E^{TOA}}{\phi^{IS}E^{IS}} = (\frac{p^{TOA}}{p^{IS}})^2 \tag{3.60}$$

here p and E are respectively antiproton momentum and energy while $\phi^{IS,TOA}$ are the interstellar flux and the one at the top of atmosphere. The following relation is still valid

$$E^{TOA} = E^{IS} - C \tag{3.61}$$

where C is a parameter that can be experimentally determined.
If we compare PAMELA $\bar{p}/p$ ratio with some theoretical curves (see Fig. 3.12), we can say that the secondary antiprotons production is sufficient to explain the experimental results, in the range accessible to the experiment. To obtain these theoretical curves, a deep propagation and diffusion parameters knowledge is necessary.

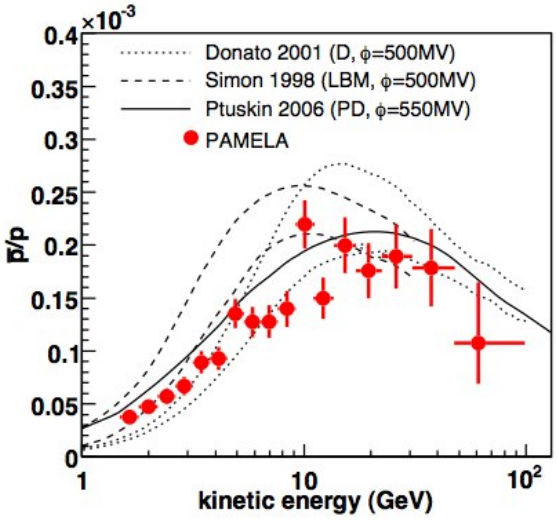

Figure 3.12: *$\bar{p}/p$ ratio measured by the PAMELA experiment. The different lines shown one refer to three different theoretical models[95].*

Let's now consider the last possible mechanism responsible for the antiproton production, that is the dark matter annihilation. Unlike previous cases, here we need a primary source; its production rate can be expressed as:

$$q_{\bar{p}}^{DM}(r, z, T_{\bar{p}}) =< \sigma_{ann} v > g(T_{\bar{p}})(\frac{\rho_\chi(r, z)}{m_\chi})^2 \tag{3.62}$$

here $\sigma_{ann}v$ is the thermal cross section with $\sigma_{ann}v \simeq 10^{-26}\ cm^3 s^{-1}$, $\rho_\chi(r, z)$ is the dark matter density inside the galactic halo, m_χ is the dark matter candidate mass and $g(T_{\bar{p}})$ is the dark matter annihilation differential spectrum that we can rewrite as:

$$\frac{dN_{\bar{p}}}{dE_{\bar{p}}} = \sum_{F,h} B_{\chi,h}^F \frac{dN_{\bar{p}}^h}{dE_{\bar{p}}} \tag{3.63}$$

Here we consider the WIMP annihilation into quarks and gluons (h stands for hadronic), F is the final state and B is the branching ratio. During this reaction quarks and gluons can produce jets and their fragmentation can lead to an energy spectrum reproducible through Monte Carlo simulations.
If we consider a spherical halo, we can express the Dark Matter density as:

$$\rho(r) = \rho_s(\frac{r_s}{r})^\gamma[1 + (\frac{r}{r_s})^\alpha]^{(\gamma-\alpha)/\alpha} \tag{3.64}$$

where r is the galactocentric distance, r_s and ρ_s are scale parameters and α, γ, β are parameters connected to the halo model chosen.
Let's now consider positrons, above few GeV, the main process for energy loss are syncrotron radiation in the galactic magnetic field and inverse Compton scattering.

We can write the energy loss rate for these particles in the following way[95]:

$$b^{loss}(E) =< \dot{E} > = -\frac{E^2}{E_0 \tau_E} \tag{3.65}$$

where E_0 is a reference energy, here $E_0 = 1$ GeV, and τ_E is the characteristic loss time $\tau_E = 10^6$ s.
Using this relation we can rewrite the transport equation as

$$-K\nabla^2\psi + \partial_E(b^{loss}(E)\psi) = q(x, E) \tag{3.66}$$

For energies higher than 1 MeV, positrons can be considered as relativistic particles, so that their rigidity is proportional to the energy. So we can express K as

$$K(\epsilon) = K_0\epsilon^\delta \tag{3.67}$$

Here $\epsilon = \frac{E}{E_0}$ and we can redefine the time as

$$\tilde{t}(E) = \tau_E(\frac{\epsilon^{\delta-1}}{1-\delta}) \tag{3.68}$$

Using these relations the transport equation can be written as [40]:

$$\frac{\partial\tilde{\psi}}{\partial\tilde{t}} - K_0\nabla^2\tilde{\psi} = \tilde{q}(x, \tilde{t}) \tag{3.69}$$

where $\tilde{\psi} = \epsilon^2\psi$ and ψ is the spatial-energy density, while the source term is redefined as $\tilde{q} = \epsilon^{2-\delta}q$.
Using this formalism we can express the positron density as:

$$\psi_{e^+}(x, E) = \int_{E_S=E}^{E_S=+\infty} (dE_S \int (d^3x_S G_{e^+}(x, E \leftarrow x_S, E_S) q_{e^+}(x_S, E_S) \tag{3.70}$$

The second integral is calculated on the galactic halo and the term G_{e^+} is the positron propagator that is proportional to the Green function through the following relation:

$$G_{e^+}(x, E \leftarrow x_S, E_S) = \frac{\tau_E}{E_0\epsilon^2}\tilde{G}_{e^+}(x, \tilde{t} \leftarrow x_S, \tilde{t}_S) \tag{3.71}$$

Green function form depends on the halo model we choose, then if we consider an infinitely extended diffusive halo, we obtain

$$\tilde{G}_{e^+}(x_{sun}, \tilde{t} \leftarrow x_S, \tilde{t}_S) = (\frac{1}{4\pi K_0\tilde{t}})^{3/2} e^{-\frac{r^2}{4K_0\tilde{t}}} \tag{3.72}$$

where $\tilde{\tau} = \tilde{t} - \tilde{t}_S$ is the time the energy takes to drop from E_S to E, r is the source-Earth distance and x_{sun} is the Sun position.
The Gaussian distribution is approximately constant in a sphere with a radius $\lambda_D =$

$\sqrt{4K_0\tilde{\tau}}$, so we can define a positron sphere that is the region centered on Earth position that delimits the halo where positrons can origin. The above defined radius represents the mean path for a particle with a starting energy E_S that arrives on Earth with an energy E. Using the radius definition we can rewrite the positronic propagator as:

$$G_{e^+}(x, E \leftarrow x_S, E_S) = \frac{\tau_E}{E_0 \epsilon^2} \tilde{G}(x \leftarrow x_S, \lambda_D) \tag{3.73}$$

As already discuss for antiprotons, also in the case of positron we have to modify the source term in the transport equation. Here we can distinguish between two possible contributions: one comes from the spallation secondary production while the second comes from Dark Matter primary production.

Let's start with the secondary production, the main mechanism in this case is the collision between protons and Hydrogen atoms at rest: this reaction can produce $\pi^{\pm}$ that decay in $\mu^{\pm}$ that decay finally in $e^{\pm}$. Also kaons $K^{\pm}$ can produce positron, but this channel is quite rare. The positron production rate can be written as:

$$d\Gamma^{sec}_{e^+}(E_e) = \frac{d\sigma}{dE_e}(E_p \rightarrow E_e) \cdot \beta_p \cdot (\psi_p(E_p) \cdot dE_p) \tag{3.74}$$

here σ is the positron cross section, $E_{p,e}$ are respectively proton and positron energies and β_p is the proton relative velocity. Then we can write the source term as:

$$q^{sec}_{e^+} = 4\pi n_H(x) \int \phi_p(x, E_p) \cdot dE_p \cdot \frac{d\sigma}{dE_e}(E_p \longrightarrow E_e) \tag{3.75}$$

Where ϕ_p is the proton flux and n_H is the hydrogen density.

Finally let's consider the Dark Matter contribution to the source term[95]. Combining the two previous relations (,) i.e. the positron density with the positron propagator, we can write the primary positron flux produced by WIMP annihilation as:

$$\phi^{DM}_{e^+}(\epsilon = \frac{E_e}{E_0}) = F \cdot \frac{\tau_E}{\epsilon^2} \cdot \int_{\epsilon}^{m_\chi/E_0} (d\epsilon_S g(\epsilon_S) \tilde{I}_{DM}(\lambda_D)) \tag{3.76}$$

Here $\phi^{DM}_{e^+}$ is the DM positron flux, F is a function related to annihilation cross section (σ_{ann}), DM mass (m_χ), Dark Matter density near the sun (ρ_{sun}) and to relative velocity, that can be written as:

$$F = \frac{\beta}{4\pi} < \sigma_{ann} v > (\frac{\rho_{sun}}{m_\chi}) \tag{3.77}$$

The function $g(\epsilon_S)$ in the previous integral describes the positron spectrum at source and depends on WIMP annihilation mechanism. Finally the term $\tilde{I}_{DM}$ is related to the Green function $\tilde{G}$ and to Dark Matter density (ρ_χ) and can be expressed with the following relation:

$$\tilde{I}_{DM} = \int d^3 x_S \tilde{G}(x_{sun} \leftarrow x_S, \lambda_D)(\frac{\rho_\chi(x_S)}{\rho_{sun}})^2 \tag{3.78}$$

Where the integral is calculated on the diffusive halo.
In conclusion we want here to notice that, although the Higgs boson discovery make it possibile to reduce the number of DM candidates, many other theories must be studied in detail, to validate or discard the remaining ones. The combined efforts of AMS-02, which provide the opportunity to study both the leptonic channel and the hadronic channel, and the possibility of direct search coming from Xenon 100 and LHC production, will help us to finally find the extensive model able to explain DM particle nature.

Chapter 4

AMS-02

The Alpha Magnetic Spectrometer (AMS) is a high energy physics experiment designed to operate as an external module on the International Space Station (ISS) (figure 4.1). It uses the unique environment of space to study the Universe and its origin by searching for primordial antimatter and dark matter while performing precision measurements on cosmic rays composition and flux. Orbiting the Earth on the ISS at an altitude of about 400 km, AMS-02 studies with an unprecedented accuracy of one part in 10 billions the composition of primary cosmic rays, that after being accelerated by strong magnetic fields, traveled for hundreds of millions of light years before reaching the experiment[98].

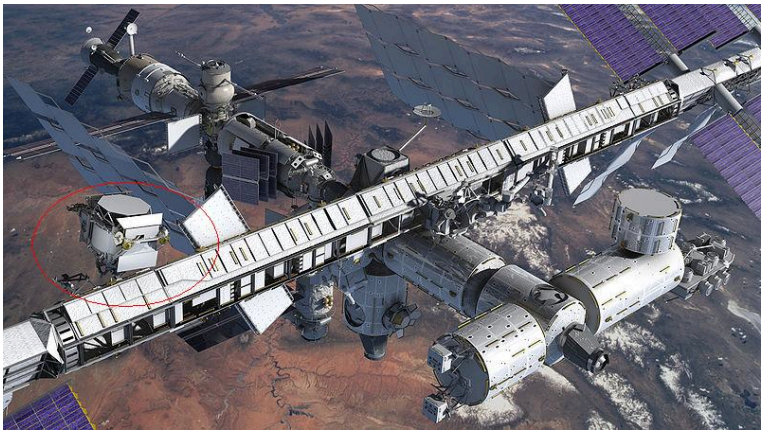

Figure 4.1: *AMS-02 on the upper Payload Attach Point on S3 Truss of the International Space Station[98].*

4.1 The Experiment: Goals and Measurements

The main goal of the AMS-02 experiment is to search for antimatter of primordial origin looking for the presence of anti-nuclei (Z≥2) in the cosmic rays. Experimental evidences indicate so far that our Galaxy is made of matter. However, there are more than hundred million galaxies in the Universe and the Big Bang theory on the origin of the Universe requires equal amounts of matter and antimatter. Theories that ex-

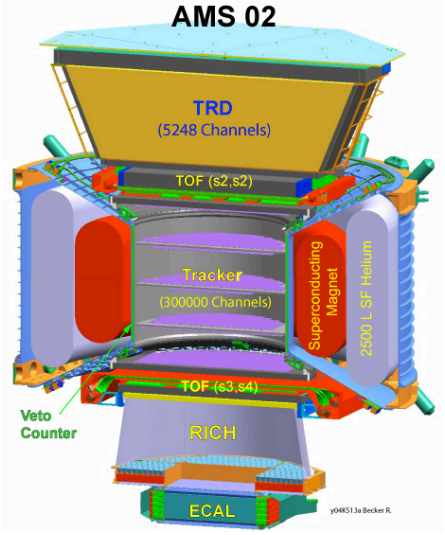

Figure 4.2: *Schematical view of the AMS-02 experiment with its subdetectors[98].*

plain this apparent asymmetry violate other measurements. Whether or not there is significant antimatter is one of the fundamental questions on the origin and nature of the Universe. The detection of even a single antinucleus in the cosmic radiation, as a nucleus of He, would provide evidence for the existence of antimatter domains, since the probability of a spallation production of He is extremely low. Another interesting discover potential for AMS concerns the indirect dark matter detection. The visible matter in the Universe, such as stars, adds up to less than 5% of the total mass that is known to exist from many other observations. The other 95% of matter is dark, which is estimated at 26% of the energy balance of the Universe; the remaining part is made up by dark energy. The exact nature of both is still unknown. Any excesses in the background positron, antiproton, or gamma ray flux could signal the presence of a dark matter candidate. Thanks to the large acceptance, the long exposure time and the excellent particle identification capabilities, AMS can measure the spectra of the CR rare components (p, e+, D, γ) with a great accuracy over a never explored energy range. The high statistics measurements of AMS-02 of all the charged species of cosmic rays, including chemical species up to Iron and isotopes up to Carbon, will largely improve our knowledge of the cosmic rays and will help to solve several astrophysics

fundamental questions[91,93,94]. The measurement of the nuclear and isotopic composition of cosmic rays can be used to validate or discard models for particle propagation in the interstellar medium; in particular, the accurate determination of the Boron to Carbon ratio over a wider range of energies will be crucial to determine propagation parameters like the thickness of the galactic halo or the galactic wind velocity. AMS-02 is composed of several subdetectors, each able to misure the energy and to identify every particle passing through it. The main detectors are presented in the following sections and shown in Figure 4.2.

4.2 Transition Radiation Detector (TRD)

On the top of the instrument, just below the first layer of the Silicon Tracker, a Transition Radiation Detector is used to identify electrons and positrons within the leading background of protons and nuclei. This subdetector is capable of discriminating different particles using the emission of a special kind of radiation called transition radiation. Transition radiation is produced when a particle passes through a medium composed of materials with different dielettric constants. This radiation is emitted within an angle proportional to $\frac{1}{\gamma}$ ($\gamma = \frac{E}{m}$) while its intensity depends on γ; this way different particles may be discriminated using the measure of the transition radiation. The AMS

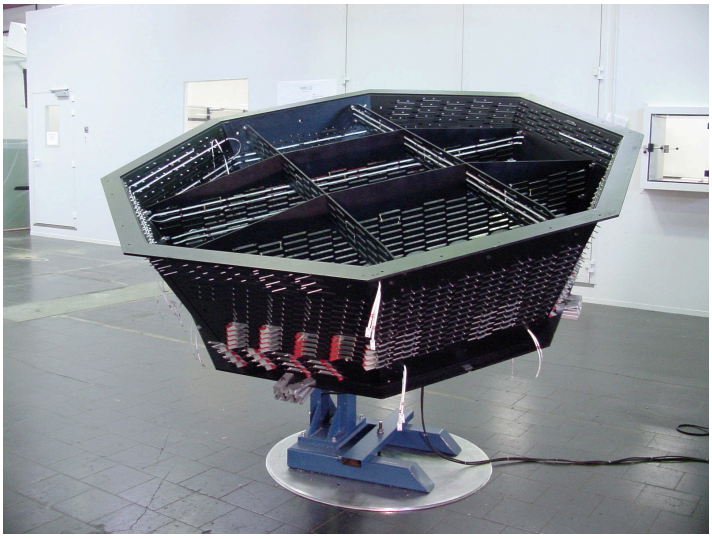

Figure 4.3: *View of the TRD integrated before its installation on the whole detector[188].*

TRD has a truncated octagonal pyramidal shape (figure 4.3), is composed of 328 modules divided in 20 layers along the up coordinate. Each layer is made up by 20 mm irregular polypropylene/polyethylene fiber fleece as radiator (density $\simeq 0.06 g/cm^3$) and wire straw tubes with an inner diameter of 10 mm and filled with Xe and CO_2.

The X-rays emitted in the transition radiation are detected using straw tubes, particles underthreshold loose energy through ionization producing a lower signal, this way electron can be discriminated from proton up to 600 GeV. To keep the detector filled with clean gas, AMS has a gas recirculation system; an extra amount of Xe and CO_2, stored in lightweight bottles, accompany the TRD. A network of valves and pressure sensors can whip up fresh Xe and CO_2 at a rate of 7 liters per day, into the 300 liter detector volume. Within the TRD, the gas is flushed in a closed circuit and there are pumps, valves, and CO_2 analyzers to monitor its properties[104].

4.3 Time of Flight (TOF)

The AMS Time of Flight (TOF) detector consists of four planes of plastic scintillators, displaced alternatively along the x and y axis: two of them are placed above the magnet and constitute the so called Upper Tof (UT), the other two are placed under the magnet and called Lower Tof (LT), see Figure 4.4[87,90]. Each plane that composes the UT

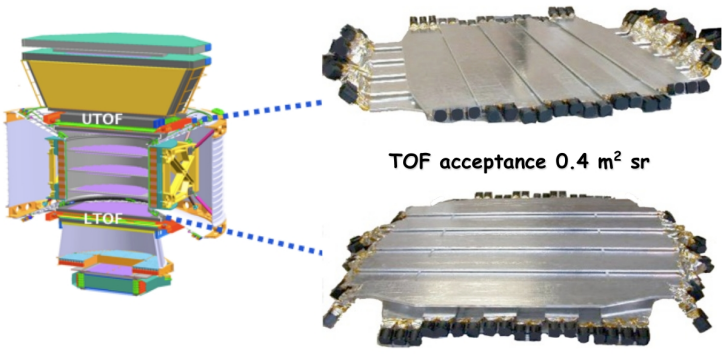

Figure 4.4: *Exploded view of the AMS TOF detector[95].*

is made of 8 scintillator (layer 1 and 2), the third plane (in the LT) is made of 10 scintillators while the last one (layer 4) is made of 8 scintillator counters[92,96]. The central 26 scintillator counters of the TOF planes are rectangular in shape (width=12 cm, height=1 cm) while the external ones are trapezoidal. The light produced in the rectangular scintillator counters is collected using 4 Photo Multiplier Tubes (PMTs), two for each side, while for the trapezoidal ones 6 PMTs are used, three for each side; this way the temporal resolution is almost independent from the passage point of the particle. The PMT used for the AMS TOF are R5946 W/FL Hamamatsu, choosen for their good temporal resolution while working in presence of high magnetic fields. Each PMT contains 16 dinodes, with a total gain of 106 at 2000 V, a corresponding rising

Figure 4.5: *View of the TOF layers[98].*

time of 1.9 ns, a transit time of 7.7 ns and a wavelenght sensitivity from 300 nm to 600 nm (maximum at 420 nm). The anod signals collected from the PMTs of the same side are summed and used as trigger for low charged particles while the dinode ones are read separately and used for high charged particles. The connection between the scintillator counter and each PMT is achieved using plastic light guides (see figure 4.6), characterised by a variable orientation, with the aim of minimizing the angle between the magnetic field and the PMT axis[96]. Because of power and weight limitation, each high voltage alimentation channel is simultaneously connected to two PMTs, belonging to different sides of the scintillation counter: this configuration guarantees redundancy, necessary beacuse the detector operations are in space, and then not accessible to the human intervention. The AMS TOF furnishes several measurements and information:

- AMS fast trigger
- time of flight measurement (with a mean time resolution $\sigma_t = 180$ ps for fundamental particles)
- discrimination between upgoing to downgoing particles
- discrimination between protons and nuclei with $Z \geq 1$

4.3.1 How it works

Scintillating materials exhibit a special property called *luminescence*, that is the capability of absorbing energy and riemitting it as light. This process can be splitted in two subprocesses: the fluorescence take place when the duration of the riemission time

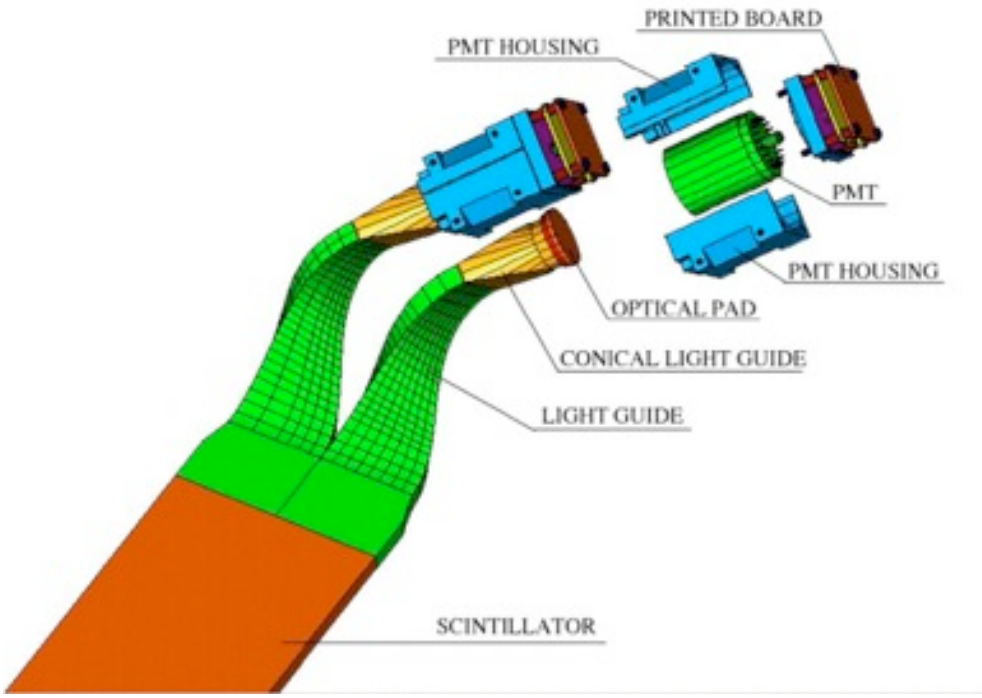

Figure 4.6: *Connection between the scintillator counter and the PMT in the TOF detector[95].*

is about 10^8 s, otherwise the process is called *phosphorescence*, and the riemission time is longer[102,103]. The time evolution of the light emission can be written using an exponential function as in the following equation:

$$N = A \cdot e^{\frac{-t}{\tau_f}} + b \cdot e^{\frac{-t}{\tau_s}} \tag{4.1}$$

where N stands for the number of photons emitted at the time t, τ_f and τ_s are the fast and slow decaying constants while A and B are constants associated with the fast and slow components (usually the fast component is the leading one) of the material the scintillator is made of. It exists a relation, linear in fist approximation, connecting the energy lost by the particle (E) and the fluorescence light produced (L):

$$L \propto E \tag{4.2}$$

Nevertheless photons produced from the passing particle could be absorbed by the molecules of the material, giving rise to the "quenching" effect, that reduces the amount of light that can be collected. For this reason the relation between the lost energy per unit length and the light produced for unit length must be corrected; this correction is included in the Birk formula:

$$\frac{dL}{dx} = \frac{A\frac{dE}{dx}}{1 + kB\frac{dE}{dx}} \tag{4.3}$$

where A is a constant connected to the scintillator efficiency and kB a parameter that describes the ionization center density. To convert the primary signal into a usable form, and to amplify it, PMTs are used. When an incident photon impinges upon the photocathode, an electron is emitted via the photoelettric effect, the efficiency for photoelectric conversion varies strongly with the frequency of the incident light and the structure of the material and can be expressed by the quantum efficiency, $\eta(\lambda)$:

$$n(\lambda) = \frac{photoelectrons emitted}{incident photons} \tag{4.4}$$

$\eta(\lambda)$ is usually less than 30% with a maximum corresponding to a wavelength close to 400 nm, but it depends on the material the photocathode is made of[102]. At a

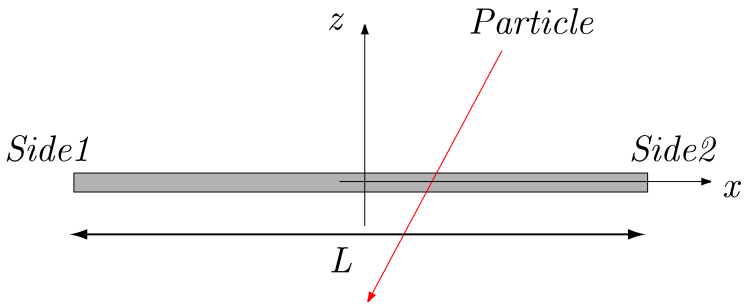

Figure 4.7: *TOF principle of working[95].*

later stage, because of the applied voltage, the electron is directed and accelerated toward the first dynode, where it transfers some of its energy to the electrons in the dynode. This causes secondary electrons to be emitted, which in turn, are accelerated towards the next dynode where more elecrons are released and further accelerated. An electron cascade down the dynode string is thus created. At the anode, this cascade is collected to give a current which can be amplified and analyzed, using the front-end electronics. All time signals are measured relative to a common value, that is the Fast Trigger, defined as the coincidence between signals coming from at least a counter for each TOF layer. Each time a traversing particle gives rise to a Fast Trigger signal, the time $t_{m1}(t_{m2})$ is memorized relative to it (see figure 4.7); this signal is connected to the crossing of the set up threshold coresponding to the side 1 (2) of the counter. Then these signals have to be corrected, because of the "slewing" effect, that is the time elapsed between the beginnig of the signal and the effective threshold crossing. Finally two other effects must be taken into account: the time spent by the light to propagate from the impact point to the counter side (see figure 4.8) and the delay induced by the electronic cables. For these reasons, the effective time corresponding to a passing

particle is[95]:

$$t_{cr2} = t_{m2} + \frac{s_2}{\sqrt{A_2}} + \frac{L/2 - x}{V} + t_{del2} \tag{4.5}$$

where t_{cr2} is the effective time relative to the Fast Trigger, t_{m2} is the time measured relative to the Fast Trigger, $\frac{s_2}{\sqrt{A_2}}$ is the slewing correction (s is the slewing parameter while A is the signal amplitude), $\frac{L/2-x}{V}$ is the delay associated to the light propagation relative to the counter middle (x) and to the light speed in the counter (V) and t_{del} is the cables induced delay. Similarly, for the other side of the counter we have:

$$t_{cr1} = t_{m1} + \frac{s_1}{\sqrt{A_1}} + \frac{L/2 + x}{V} + t_{del1} \tag{4.6}$$

The only difference here is the delay induced by the light propagation. Using the

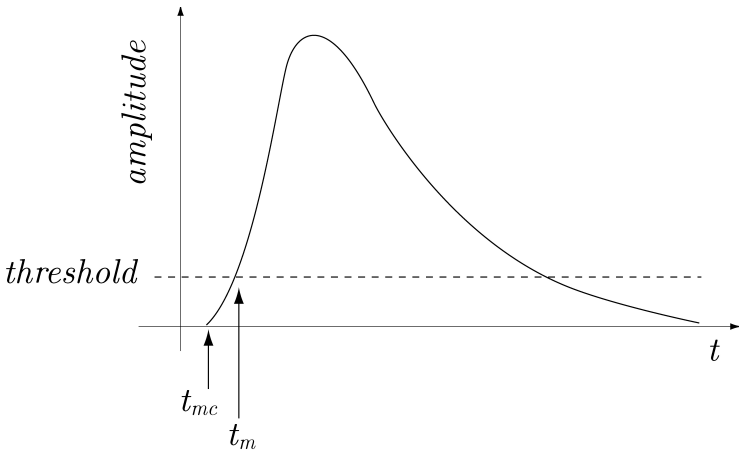

Figure 4.8: *Schematical view of the slewing correction on the effective time formation signal[95].*

previous equations (subtracting one from the other), the impact coordinate can be obtained:

$$x = V(\frac{t_{m2} + \frac{s_2}{\sqrt{A_2}} - t_{m1} - \frac{s_1}{\sqrt{A_1}} + t_{del2} - t_{del1}}{2}) \tag{4.7}$$

whereas summing up the equations the transit time can be calculated, independently from the impact coordinate:

$$t_{cr1} = \frac{t_{m1} + \frac{s_1}{\sqrt{A_1}} + t_{m2} + \frac{s_2}{\sqrt{A_2}} + \frac{L}{V} + t_{del1} + t_{del2}}{2} \tag{4.8}$$

t_{cri} represents the transit time associated with the i-counter. This way both the transit time and the impact coordinate can be obtained using the signals produced in the counter.

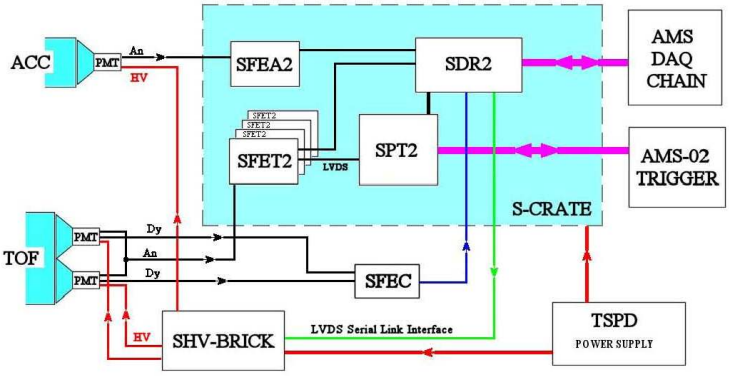

Figure 4.9: *Schematical view of the TOF electronics and ACC (Anti Coincidence Counter)[95].*

4.3.2 Electronics

The TOF electronics is composed of different components as can be seen in the Figure 4.9[95,97]:

- TSPD: this is the electronical component designate to supply the low voltage for the SHV-bricks and the S-crate;
- SHV-brick: this element supplies high voltage to the PMTs, AMS TOF contains four SHV-bricks;
- SFEC: this is the front-end electronical component that acquire the charge integrated signal, the TOF contains four of them;
- S-crate: this is an electronical element (AMS TOF contains four S-crate) made of others electronical board:
  - SFEA: is an electronic board contained in the S-crate, its task is to handle signals coming from ACC PMTs;
  - SFET: as shown in figure 4.10 SFETs are electronical boards that handle the anodic signals coming from TOF PMTs to obtain time measurements[97]. These boards have 4-5 input signals: as soon as these signals reach the SFET they are separated: 5% of each signal is directed to the charge measurement unit while the 95% is directed to the time measurement unit. In the time measurement unit the signal is then compared to three different threshold (see figure 4.11): the first is the Low threshold (LT), that corresponds to 20% of a MIP signal for ground-measured muons, the second one is the High Threshold (HT) that corresponds to 50% of the MIP peak and it's used

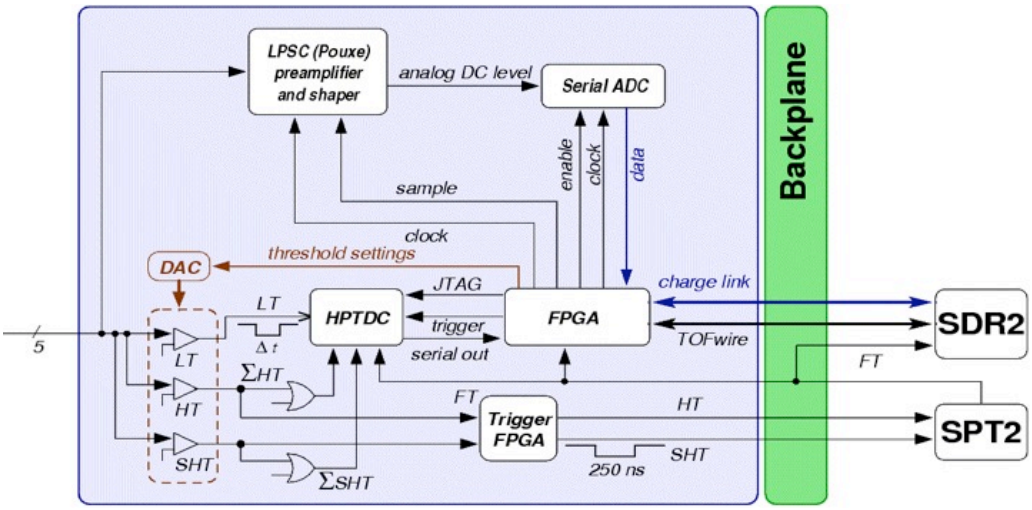

Figure 4.10: *SFET scheme.*

as fast trigger for charged particles, the last is the Super High Threshold (SHT) that is four times the MIP peak, used as fast trigger for ions. Time measurements are achieved using a HTDC, that works with a 40 GHz clock: it is equipped with 8 channels, characterized by a time resolution of $\sigma_t = 25$ ps and able to measure the formation time of the signal from 0 to 1 and vice versa;

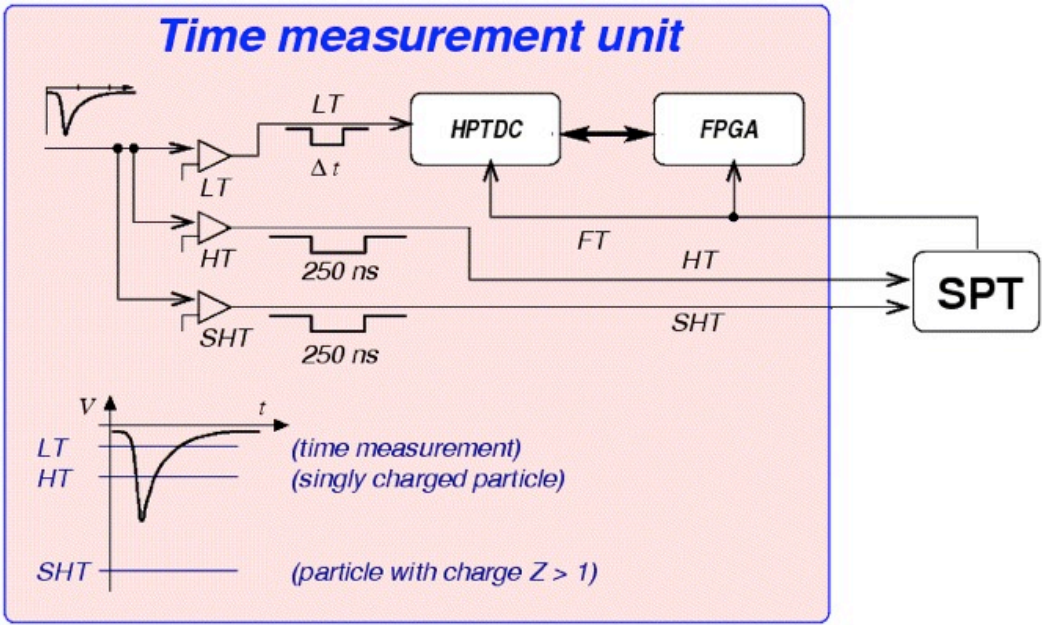

Figure 4.11: *Time measurement unit: the signal time development determines the kind of threshold, LT,HT or SHT[95].*

– SPT: it processes the signals coming from the TOF to produce the trig-

ger[116]. The input signals for this board are the HT and SHT coming from each side of the TOF layers: if the signal coming from at least a counter of one of the TOF layers passes the HT or the SHT, then a CP-CT or a BZ signal, associated to that layer, is produced. This signal is then compared with a trigger mask signal and the result of this comparing is sent to the JVL1 that will generate the trigger. The trigger generation varies depending on the logical condition that are fulfilled:

  * FTC (Fast Trigger for Charged Particles): when we have a HT signal from at least three TOF layers with $\Delta t_{GATE} = 340$ ns;
  * BZ (Fast Trigger for Ions): when we have a SHT signal from at least three TOF layers with $\Delta t_{GATE} = 340$ ns;
  * FTZ (Fast Trigger for Exotic Particle): when there is a coincidence between BZ signals (640 ns) produced in the Upper TOF and Lower TOF;

- SDR: it processes physical events and manage the communications. It acquires data from the front-end electronics and send them to upper acquisition levels; during level-1 trigger data are divided, digitalized and then stored in a memory. From here they are read, processed then stored in the output event buffer memory and finally transmitted using the AMSwire protocol.

4.4 Magnet

A superconducting magnet (SM) was ideal for a three year stay on ISS, from 2005 to 2008, as originally planned for AMS, but after the 2003 Shuttle accident the AMS program was slowing down while the ISS operation was scheduled to end in 2010. Actually the ISS scientific program has been strengthened and its lifetime has been extended to 2020 (2028). The Shuttle flights, however ended in 2011, thus eliminating any possibility of returning and refilling a superconducting magnet. So, in 2010, AMS collaboration decides to use a permanent magnet for the experiment.

The AMS permanent magnet is composed of 6400 Nd-Fe-B blocks, each of 5x5x2.5 cm^3, divided in 100 circular shaped sections, each composed of 64 layers (Figure 4.12)[98]. The magnet has a cylindrical shape with a diameter =1.15 m and an height =0.8 m[86]. The blocks are arranged in order to produce a 0.15 T field intensity in the magnet center, that is uniform along the x axis (figure 4.13). The external residual field

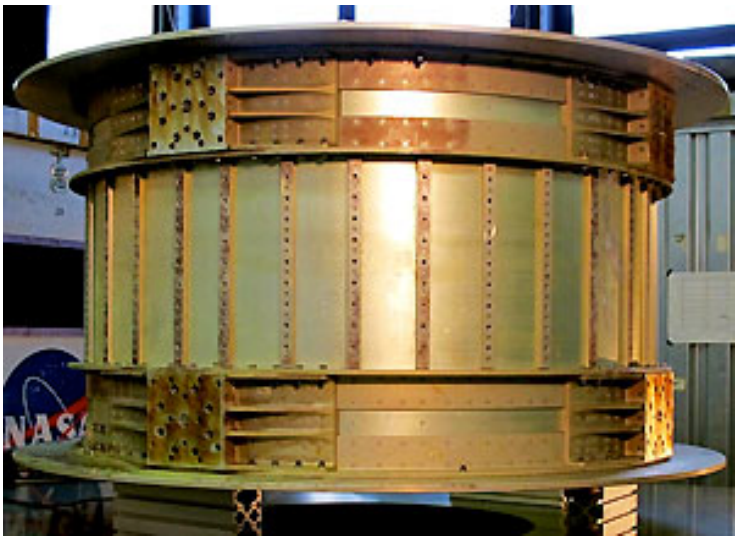

Figure 4.12: *AMS-02 permanent magnet, already used for the 1998 flight on the ISS[98].*

was designed to be smaller than $2 \cdot 10^{-2}$ to avoid torques and to minimize unwanted interferences with the electronic devices.

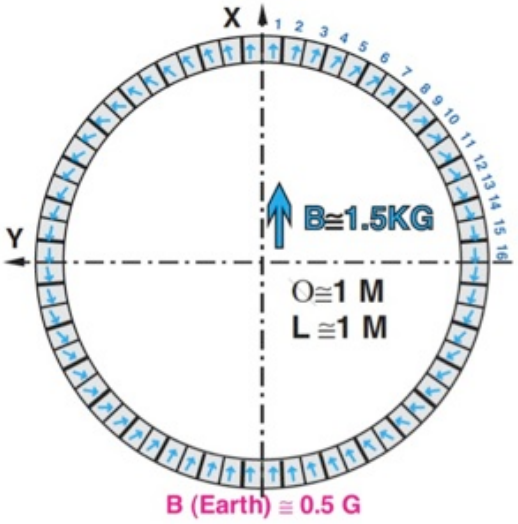

Figure 4.13: *Magnetic field orientation and intensity of the permanent magnet of AMS-02[98].*

4.5 Silicon Tracker

The AMS-02 Silicon Tracker is one of the most important subdetectors: precisely measuring the curvature of the particles traversing the magnet, it's able to define their rigidity ($R = \frac{p}{Z}$). The tracker is the only detector able to distinguish among matter and antimatter by means of charge sign determination; in fact, the curvature

of positive and negative particles are opposite[111,112]. The silicon tracker is made of 9 layers (see figure 4.14), 7 layers contained in the center of the magnet, one above the TRD and the last one above the ECAL. The basic element that constitute each layer

Figure 4.14: *One of the nine layers that constitute the AMS Tracker system[98].*

is the double-sided micro-strip sensor, which consists on a substrate of high purity doped silicon 300 μm thick; on the two sides of the substrate tiny aluminum strips run in orthogonal directions. When a charged particle crosses the silicon substrate, about 24000 electron/hole pairs are created and these charges drift in opposite directions within 10 ns due to the electric field applied between the two sides (80 V) (see Figure 4.15). Only strips near to the migrating charges will give signal. The charge center of gravity of these strips provides a position resolution of 10 μm, while the sum of the electric signals on the hit strips is proportional to the square of the absolute charge of the particle. From a structural point of view the silicon tracker is composed by 2264 double-sided silicon sensors (72x41x0.3 mm^3) assembled in 192 read-out units, called ladders (figure 4.16). These ladders are connected from one side to the Tracker Data Reduction, designed for the early zero suppresion of not interesting events, and from the other side to the Tracker Thermal Control System able to remove the excess of heat produced from the Tracker channels.

4.6 Ring Imaging Cherenkov (RICH)

The main aim of the AMS-02 Ring Imaging Cherenkov is to estimate the particles velocity with a high accuracy ($\simeq$ 0.1%). Velocity derives from pattern recognition of photons distributed over geometrical shapes as circles produced by the Cherenkov

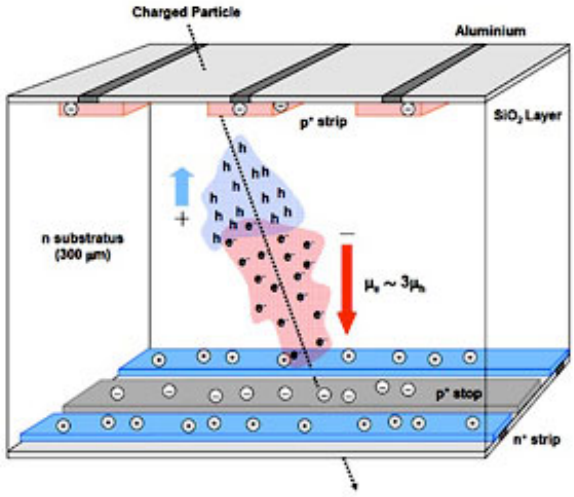

Figure 4.15: *Measurement principle of the Double-Sided Microstrip Silicon Sensor[98].*

Figure 4.16: *Assembly of the AMS02 Silicon Tracker inside the Magnet at CERN[98].*

effect. Using the measured velocity and combinig it with the rigidity and the charge measured by the tracker, the particle mass can then be determined[104].
As already disclosed, the measurements performed by this detector are based on the Cherenkov effect, that is when very fast particles traverse the medium with a velocity that is slower than the speed of light in vacuum but faster than the speed of light in that medium, then these particles will emit a light cone (see figure 4.17).

$$c\beta \geq \frac{c}{n} \tag{4.9}$$

The Cherenkov radiation consists of photons emitted along a characteristic cone whose angular aperture is directly related to the particle velocity and with the refraction index

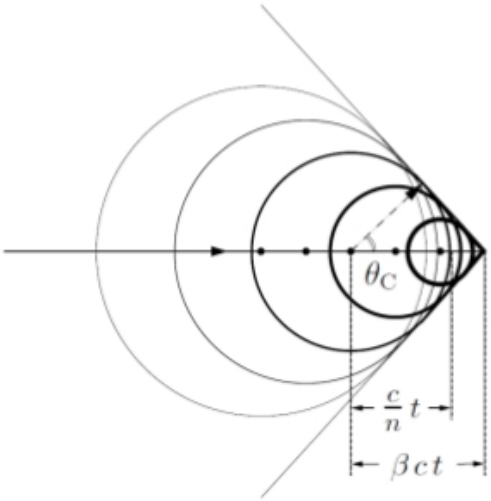

Figure 4.17: *Cherenkov effect[102].*

of the material:

$$\cos\theta_C = \frac{1}{n\beta} \tag{4.10}$$

After passing through the RICH thin radiator the cone produced by the particle expands in vacuum and it is finally detected over a sensible surface. On this surface, the cone projection appears to be an ellipse or a circle depending on the particle incidence angle (see figure 4.18). A pattern recognition algorithm reconstructs the particle velocity from the detected geometrical shape, while the charge measurement (Z) derives from the total amount of collected photons:

$$\frac{d^2N_\gamma}{dxd\lambda} = \frac{2\pi\alpha}{\lambda^2}(1 - \frac{1}{\beta^2 n^2}) \qquad with \qquad \alpha \simeq 1/137 \tag{4.11}$$

The AMS-02 RICH is composed of a radiator plane, responsible for the Cherenkov radiation production, which consists of a dodecahedral polygon with a 118.5 cm internal tangent diameter. An array of 2.7 cm thick aerogel tiles with a refractive index between 1.03 and 1.05 surrounds a central 35x35 cm^2 region equipped with 5 mm thick Sodium Fluoride (NaF) radiator ($n_{NaF} = 1.335$)[99]. A 47 cm height conical reflector multi-layer structure, on a Carbon fiber reinforced composite substrate, encloses the radiator and the detection plane. The mirror increases the RICH acceptance reflecting high-inclination photons and provides the necessary photon drift ring expansion. The final part of the RICH is the detection plane, composed of an array of 680 PMTs connected with light guides, characterized by a hole in the center, corresponding to the active area of the underlying ECAL.

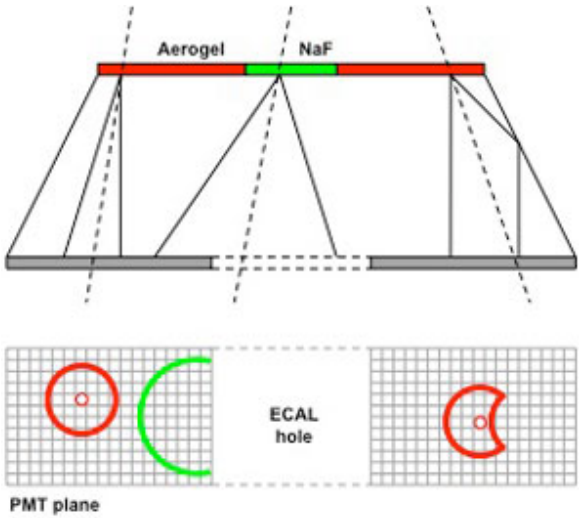

Figure 4.18: *RICH measurement principle[98].*

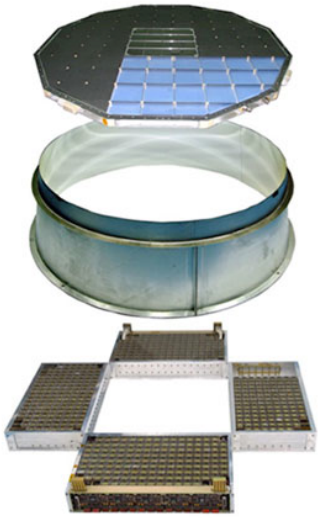

Figure 4.19: *AMS-02 RICH exploded view: radiator, conical mirror and detector plane[98].*

4.7 ECAL

The Electromagnetic Calorimeter (ECAL) is a heavy-lead brick equipped with instrumentation, able to distinguish among electrons/antiprotons and positrons/protons with an identification power of one positron over 100,000 protons. The positron has the same proton charge and sign, but a 1/2000 mass and a similar argument is valid for the negative sign particles, as electrons and antiprotons: since they cannot be separated by a magnetic field, for this aim the ECAL is used[113,98]. The measurements performed by this detector are based on the production of the so called electromagnetic shower, that is when a high-energy e^+, e^- or γ passes through a material with a high Z, many other e^+, e^- and γ of lower energy are produced. This process is caused by the inter-

play of two phenomena: the bremsstrhalung (or production of photons by high energy positrons and electrons), and the pair production that consists in the conversion of a photon in a e^+/e^- pair. The shower ends either when secondary particles are absorbed in material or when they are able to escape from the material. An incident proton interacts in a very different way, producing an hadronic shower, which has a totally different shape. The proton shower is characterized by the production of many types of

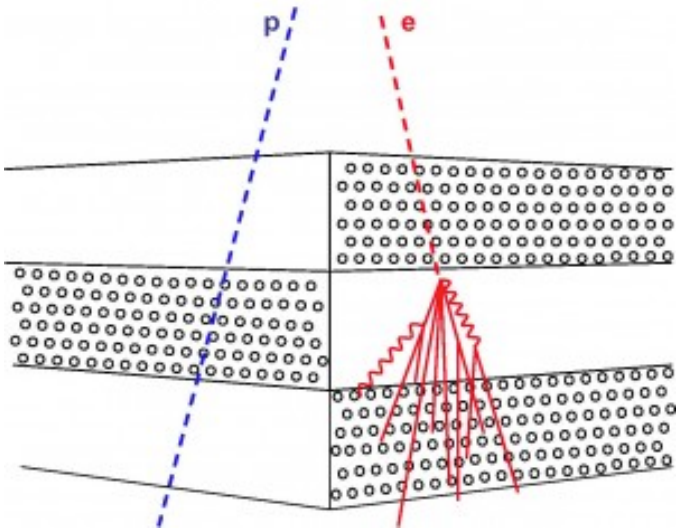

Figure 4.20: *Electron production of an electromagnetic shower passing through the ECAL[98].*

particles (pions, kaons and others) resulting in a wider shower: this way it is possible to distinguish between e^+/p and $\bar{p}/e^-$ (see Fig. 4.20). The AMS ECAL is composed of 9 super-layers with an active area of 648x648 mm^2 and a thickness of 166.5 mm. Each super-layer is 18.5 mm thick and made of 11 grooved, 1 mm thick, lead foils interleaved with layers of 1 mm diameter scintillating fibers, glued together with epoxy resin and arranged alternatively parallel to the x-axis (4 layers) and y-axis (5 layers); see Fig. 4.21.

Figure 4.21: *The ECAL brick before the final integration[95].*

4.8 ACC, TAS and Star Tracker

The Anti-Coincidence Counter (ACC) is the AMS Cerberus (see Fig. 4.22), indeed thousand cosmic rays, from all directions, pass through AMS per second: the ACC can discard 8/10 of these particles and save the ones useful for the physics analysis. Particles with a high incident angle cannot be well measured, so the ACC reject them[98].

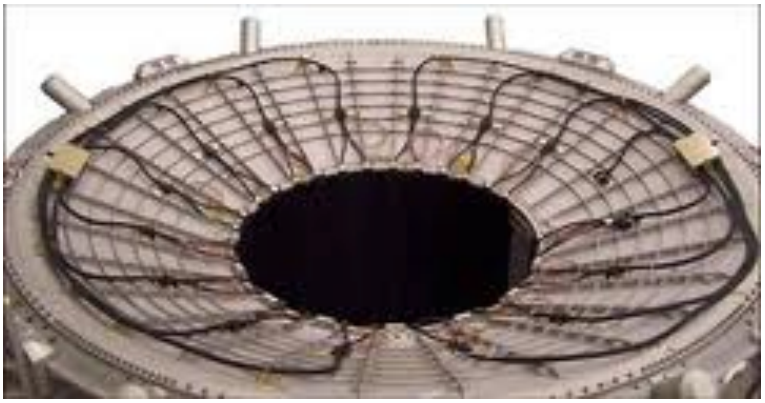

Figure 4.22: *The ACC integration in the vacuum case[98].*

ACC is also important for the rejection of high-energy particles incident on AMS materials (magnet, aluminium honeycomb, etcetera) that interact inelastically; the result of such interactions is the production of a lot of particles, that could be a significant background for the search of faint antimatter signals.
From a structural point of view this subdetector is composed of 16 paddles arranged on a cylinder surrounding the Tracker. Wavelength shifter fibers with 1 mm diameter, embedded in grooves milled into the scintillating material, collect the light coming from the scintillating paddles. At both ends of each paddle, fibers are routed on 2 bunches of 37 fibers each to connectors located on the conical flanges of the magnet vacuum case. From these connectors, the light is routed through clear fibers to 8 PMTs mounted on the rim of the vacuum case.

The Tracker Alignment System (TAS) represented in Fig. 4.23, checks the stability of the Tracker alignment using a procedure called misplacements alignment[98]. Knowing the exact position of each module of the tracker is of fundamental importance for the trajectory determination , the detector is able to trace a Tracker geometry change with accuracy better than 5 μm. Ten pairs of alignment control laser beams equip the AMS-02 Tracker. Laser diodes mounted outside of the inner Tracker volume generate the photons beam. The wavelength of these beams, 1082 nm (infrared bandwidth or IR),

has been chosen such as to penetrate all the seven inner Tracker Silicon detector layers at once. The Tracker sensors placed along the alignment beams have an anti-reflective coating (SiO_2 and Si_3N_4) optimized for the chosen wavelength (residual reflectivity $\simeq 1\%$). This coating reduces the strong attenuation caused by the high refractive index of Silicon.

The Star Tracker (Fig. 4.24) determines the orientation of AMS in the sky, more

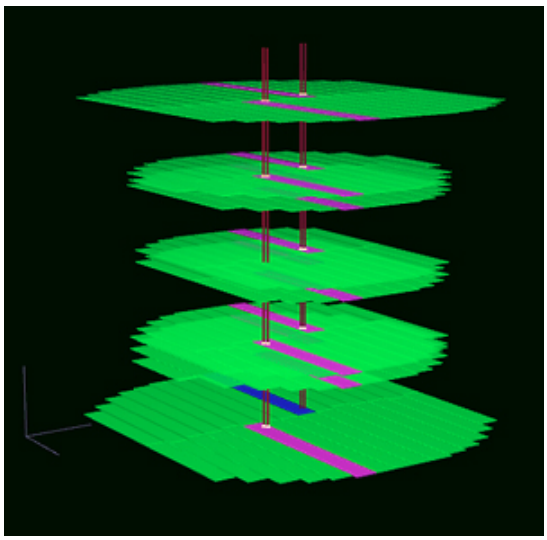

Figure 4.23: *Four of the ten laser lines of the TAS as seen by the Tracker Monitor Display[98].*

precise than the ISS one[98]. Two CCD digital photographic cameras placed on both sides of AMS compose the Star Tracker. We need two because, from time to time, one of the two could point toward the Sun and cannot be used. Star Tracker takes pictures of the sky in a 6 degrees field-of-view. A comparison between the taken picture and stellar maps could reveal the orientation of AMS in the sidereal reference frame. Star Tracker acquires a picture of the sky every 10 seconds, to describe finely the AMS orientation along the 90 minutes ISS orbit.

Figure 4.24: *The Star Tracker integrated on the top of AMS[98].*

Chapter 5

The GALPROP Software

5.1 GALPROP Model

Galactic cosmic rays are important part of the interstellar medium. The energy density of relativistic particles is about 1 eV cm^{-3} and is comparable to the energy density of interstellar radiation field, magnetic field, and turbulent motions of the interstellar gas. This makes cosmic rays one of the essential probe in determining the dynamics and processes that happen in the interstellar medium.

The variety of isotopes in cosmic rays allows us to study different aspects of their acceleration and propagation in the interstellar medium as well as the source composition. Stable secondary nuclei tell us about the diffusion coefficient, about the galactic wind (convection) and about reacceleration in the interstellar medium (2nd order Fermi acceleration mechanism). Longlived radioactive secondaries allow us to constrain global galactic properties such as galactic halo size. Abundances of K-capture isotopes, which being stopped in the interstellar gas would decay via electron K-capture, allow to probe the gas density and acceleration time scale. All these together allow us in principle to build a model of particle acceleration and propagation in the Galaxy[134]. Such a model is however incomplete. The whole of our knowledge is based on measurements done only at one point on the outskirts of the Galaxy, the Solar System, and on the assumption that particle spectra and composition are almost the same at every point of the Galaxy, the latter may not necessarily be correct. However γ-rays are able to deliver the information directly from distant regions thus complementing that obtained from cosmic ray measurements.

To extract information which is contained in cosmic ray abundances and γ-ray fluxes one needs to develop a model of particle production and propagation in the Galaxy. Analytical and semi-analytical models are able to interpret one or only a few features

and often fail when they try to deal with the whole variety of data. Therefore more realistic and consistent models are required which would be able to incorporate many processes and astrophysical data of many different kinds simultaneously.
Clearly, a detailed model of cosmic ray propagation in the Galaxy should supplement the high quality data obtained by recent experimental missions, providing support for the necessary interpretation and analysis.
Concerning the software used to produce cosmic rays fluxes, our choice fell on the GALPROP model. Among the reasons for this choice we have: the code that comes with the GALPROP model (hereafter GALPROP) is public and flexible i.e. it can be updated introducing new data or processes, it has a completely physical approach, since a real propagation environment (a 3D simulation is available) and all the known propagation effects (such as diffusion, convection, reacceleration, fragmentation, decay, loosing energy interaction and so on) are included, finally it is able to reproduce simultaneously almost all the data from space missions.
This software can be used to test CR acceleration and propagation mechanisms in the Galaxy but also to find out signatures related to new physics, through the comparison with the known physics and the observation of possible incongruities.

5.2 Galaxy Structure

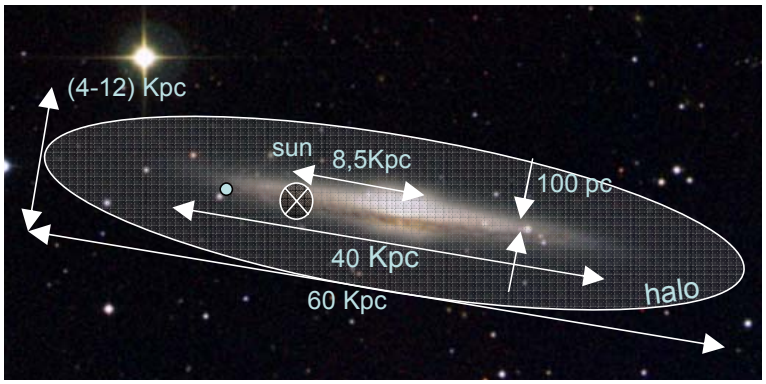

Figure 5.1: *Schematical view of the Galaxy structure in the GALPROP model[189].*

The fundamentals of any cosmic ray model reside in the assumptions that we make on the properties of the Galaxy. To have a complete description we use information taken from different fields of astronomy and astrophysics. In this section we will try to give an exhaustive description of the galactic frame as used in GALPROP model, focusing on the parameters tuned in our work to obtain good agreement with the experimental data. Each parameter can be specified using a galdef file, so the first

thing to do to get a GALPROP simulation is to built up a grid on which GALPROP works, paying attention to the fact that the more the grid is accurate the more will last the computation process: a compromise is thus necessary between this two factors. GALPROP is designed to treat both two and three spatial dimensional models, the corrisponding galdef parameter is $n\_spatial\_dimensions$.

In our work we tested both the options, obtaining comparable results despite very

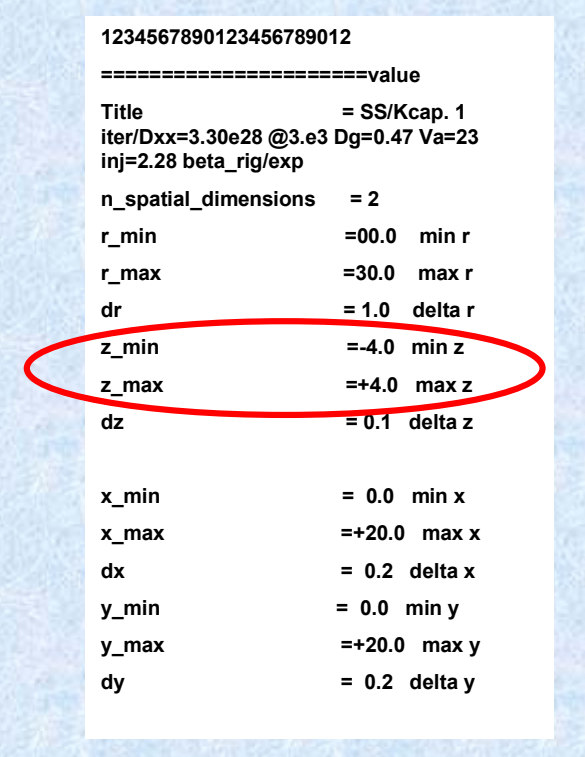

Figure 5.2: *Section of a geldef grid containing Galaxy structure parameters. Here dr and dz represent respectively the cell size in galactocentric radius and in z direction, avaible in both the 2D and 3D case, and expressed in kpc[189].*

different computational times ($\Delta t_{2D} \simeq 3min$ whereas $\Delta t_{3D} \simeq 8h$); for the two dimensional case we assumed a cylindrical symmetry (R,z) with isotropy in momentum space, whereas for the 3D a (x,y,z) system that may be fully asymmetric or not (as specified by the parameter $use\_symmetry$). In this framework the Galaxy is considered as a dense central disk of thickness 2h, where h is assumed to be 100 pc, surrounded by a cylindrical halo (centered on the disk) where cosmic rays are trapped by the galactic magnetic field (see Fig. 5.1). In the disk the CR sources are located and this is the only place where interactions with matter take place. The half height of the halo (z_min and z_max in galdef file) is one of the most important parameter defined by the user, usually running in an interval from 1 kpc to 15 kpc as suggested by previous studies on radioactive nuclei [127] and distribution of synchrotron radiation [122]. The radial

extension of the halo usually runs from 10 kpc to 30 kpc and corresponds to the galdef parameter *r_max*. Beyond the halo cylindrical box, cosmic rays are free to escape, while inside it diffusion and reacceleration are supposed to work. The Solar System is located at about $8.3 \div 8.5$ kpc from the center of the Galaxy [125,126].
All the galdef parameters described above are shown in Fig. 5.2

5.2.1 Galactic Source Distribution

In the previous section we argued that supernovae may be a reasonable source of cosmic rays. Therefore in GALPROP particular attention is dedicated to the supernovae distribution inside the disk. The source parameterization used in the model turns out to be

$$q_i(r, z, R) = f_i(r, z) \cdot \beta^{-1} R^{-\gamma_i} \delta(r - r_{max}) \tag{5.1}$$

where R is the rigidity, γ_i are the spectral index $\gamma_i \equiv \gamma_e(R), \gamma_p(R), \gamma_{nuclei}(R)$, r_{max} is the galdef parameter *source_prameter_3* and $f_i(r, z)$ is the spatial sources distribution and can be parameterized as

$$f_i \propto r^{\alpha} e^{-\beta r} e^{\frac{|z|}{z_{scale}}} \tag{5.2}$$

where α corresponds to the galdef parameter *source_parameter_1* and its value runs from 0.4 to 2, β corresponds to *source_parameter_2* and its value runs from 1 to 5. Finally z_{scale} is a modulation factor that takes into account the confinement of sources into the disk and corresponds to *source_parameter_0*: all these parameters are expressed in kpc.
In GALPROP there is the possibility to introduce point-like supernovae but we did not consider this option for our purpose.

5.2.2 Interstellar Gas Distribution

The most important component of the interstellar medium gas is Hydrogen, followed by Helium. The Hydrogen is present in the medium in three possible forms: atomic Hydrogen (HI), molecular Hydrogen (H_2) and ionized Hydrogen (HII). A good fit to the atomic Hydrogen distribution is parameterized as an exponentially decreasing function of the halo height and can be written as

$$n_{HI}(r, z) = n_{HI}(r) e^{-(ln2)(\frac{z}{z_0(r)^2})} atoms cm^{-3} \tag{5.3}$$

where $n_{HI}(r)$ is taken from [48] and represented in Fig. 5.3, while $z_0(r)$ has the form proposed in [129], namely

$$z_0(r) = \begin{cases} 0.25kpc & r \leq 10kpc \\ 0.083 \cdot e^{0.11r} kpc & r\ 10kpc \end{cases}$$

with a breaking at the galactocentric radius, approximately equal to the one of the Solar System. Concerning the molecular Hydrogen we can parameterize its density as

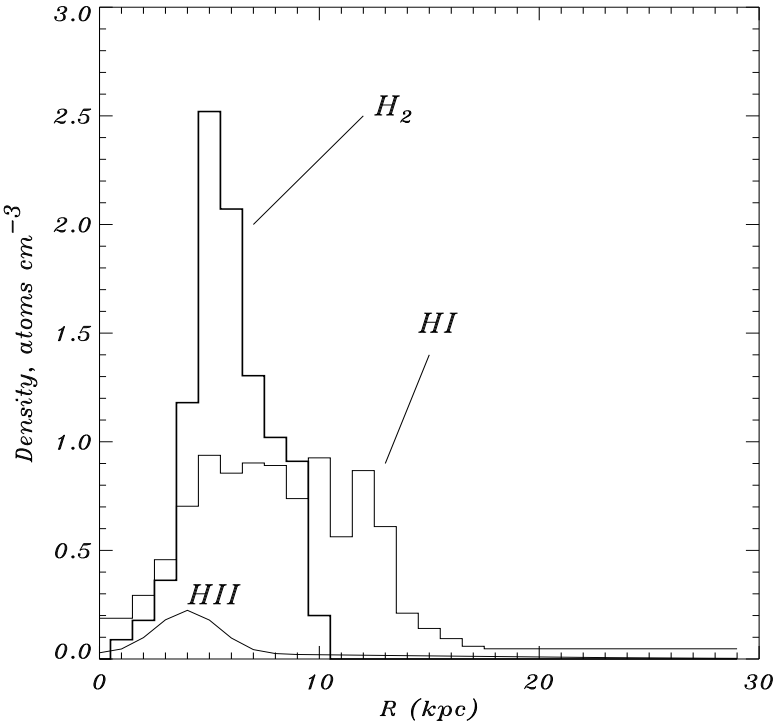

Figure 5.3: *A schematic profile of the radial dependence of the three components of hydrogen from[51].*

$$n_{H_2}(r,z) = n_{H_2} e^{-ln2 \cdot (\frac{z}{70pc})^2} cm^{-2} kpc^{-1} \tag{5.4}$$

Finally for the last component we consider a first term which represents extensive warm ionized gas added to a second component that takes into account the concentration around $r = 4$ kpc. Thus we have the following parameterization, taken from [136]

$$n_{HII}(r,z) = 0.025 e^{-\frac{|z|}{1Kpc} - (\frac{r}{20Kpc})^2} + 0.2 e^{-\frac{|z|}{0.15Kpc} - (\frac{r}{2Kpc} - 2)^2}$$

The Helium distribution in interstellar medium has been determined exploiting the photospheric methods explained in[131]. It turns out that the Helium follows the Hydrogen distribution with a factor $He/H = 0.10 \pm 0.08$, that corresponds to the galdef parameter H_He_ratio and its value runs from 0.08 to 0.11.

5.3 Galactic Magnetic Field

The direction and strength of the uniform magnetic field is a key information for cosmic ray physics, because not only it influences the cosmic ray propagation but also their trapping in the Galaxy and, consequently, the halo height is directly connected to the magnetic profile. Investigations on the uniform component of the galactic magnetic field are complicated because of the random component, whose strength exceeds that of the uniform one (the non random component is estimated to be $\simeq 5$ μG with a scale length for fluctuations $\simeq 100$ pc). Various techniques has been applied to the determination of the magnetic field. For example the work presented in [132] develops a spiral-frame line of research which is based on the large scale data set on starlight polarization [58] with nearly 7000 stars. The advantage of this kind of data is that they are free of systematic errors and the polarization is accompanied by the source location and estimate of extinction. In the GALPROP model the uniform magnetic field is consistent with the conclusions in [132] and is parameterized as

$$B = 6e^{-\frac{|z|}{5Kpc} - \frac{(r-r_\odot)}{20Kpc}} \mu G \tag{5.5}$$

Random fluctuation are not included in the model. The parameters corresponding to the galactic magnetic field in the galdef file are respectively B_field_name that determines the name of the model choosen for the simulation. In our case, the value for this parameter is the original Galprop one and corresponds to the exponential model that uses the three field parameters $B_0[Gauss]$, $r_{scale}[Kpc]$ and $z_{scale}[Kpc]$. These information are encoded in B_field_model, whose value is composed of three numbers namely bbb,rrr and zzz that enter in the magnetic field parameterization as $B = (bbb/10) \cdot e^{-(r-r_0)/(rrr/10)-|z|/(zzz/10)}$ expressed in μG: in our case the magnetic configuration corresponds to 050100020. Modifications of B_0 in the $30 \div 80 \mu G$ don't affect the resulting spectra in a significant way.

5.4 Isotopic Abundances

In the GALPROP model it is possible to consider various kind of cosmic rays, nuclei from ${}^{1}{}_{1}H$ to ${}^{64}{}_{28}Ni$, through the galdef parameters max_Z (it runs from 1 to 28) and $use\_Z\_\#$, with which we can specify which nuclei to include in the run, see Fig. 5.4. We can also propagate elementary particles: $e^-, e^+, p, \bar{p}$ and γ. It is also possible to specify the various isotopes abundances at source, using the galdef parameter $iso\_abundance\_0Z\_0A$, where Z and A vary for different nuclei isotopes (see Fig. 5.5).

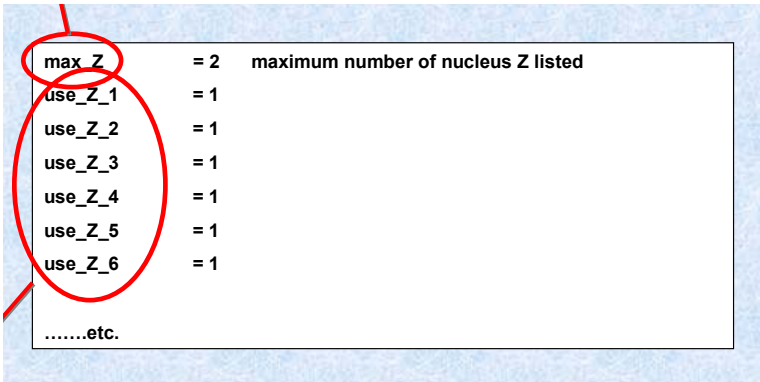

Figure 5.4: *Section of a galdef file containing the parameter that defines the amount of different nuclei in the run[189].*

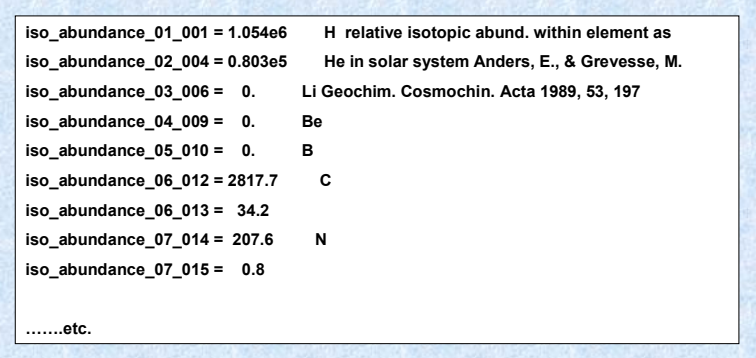

Figure 5.5: *Section of a galdef file containing the parameters associated to the isotopes abundance for various species as fixed in SM2001 (COSPAR 2001)[189].*

5.5 Propagation Equation

The propagation of cosmic rays in GALPROP is completely based on the kinetic theory that we explained in Chapter 2, and it is solved using a fixed source distribution and boundary conditions for all cosmic ray species. This includes galactic wind (convection), diffusive reacceleration in the interstellar medium, energy losses, nuclear fragmentation, and decay. The spatial boundary conditions assume zero CR density at the boundaries or, more physically plausible, free particle escape at the boundaries. Nevertheless to have contact with the code, it is important to notice that a change of variable that concerns the cosmic ray phase space density $N_j(p, \mathbf{r}, t)$ in the propagation equation presented before has to be performed. More precisely we introduce the density per unit of total particle momentum $\psi(p, \mathbf{r}, t)$ defined by

$$\psi(p, \mathbf{r}, t)dp = \int_{-1}^{1} d\cos\theta \int_{0}^{2\pi} d\varphi N(p, \mathbf{r}, t)dp \tag{5.6}$$

Rewriting the terms in the propagation equation using this function and multiplying the whole equation by p^2 we end with

$$\frac{\partial \psi}{\partial t} = \bar{\nabla} \cdot (D_{zz} \bar{\nabla} \psi - \mathbf{V_C} \psi) + \frac{\partial}{\partial p} p^2 D_{pp} \frac{\partial}{\partial p} \frac{1}{p^2} \psi + \frac{1}{3} \frac{\partial}{\partial p} [(\bar{\nabla} \cdot \mathbf{V_C}) p \psi] \tag{5.7}$$

where reacceleration is described as diffusion in momentum space and is determined by the coefficient D_{pp}; it is also assumed that the diffusion coefficient only has the diagonal component which is parallel to the regular magnetic field. The z-component of the convection velocity is assumed to follow a linear increasing with distance from the galactic plane[135]. The wind velocity at z=0 is a model parameter that we fixed $\mathbf{V_C}(z = 0) \equiv 0$ ($v0_{conv}$ in GALPROP). In general we have $\mathbf{V_C} > 0$ for $z > 0$, $\mathbf{V_C} < 0$ for $z < 0$, so that we can write the convection velocity gradient as dV/dz, it is positive for all z, implying a constant adiabatic energy loss. We can express the convection velocity using the previous parameters through the following relation:

$$v_{conv} = v0_{conv} + \frac{dV}{dz} dz \tag{5.8}$$

To take into account decay and fragmentation we add the two terms $\frac{-1}{\tau_d}$ and $\frac{-1}{\tau_f}$ to the right hand side of the eqution. Energy losses enter the propagation through a momentum loss rate $\dot{p}$. Finally we need to add a source term $s(\bar{r}, p)$ that includes both primary and secondary contribution. The complete propagation equation used in GALPROP is then given by

$$\frac{\partial \psi}{\partial t} = s(\bar{r}, p) + \bar{\nabla} \cdot (D_{xx} \bar{\nabla} \psi - \mathbf{V_C} \psi) + \frac{\partial}{\partial p} p^2 D_{pp} \frac{\partial}{\partial p} \frac{1}{p^2} \psi - \frac{\partial}{\partial p} [\dot{p} \psi - \frac{p}{3} (\bar{\nabla} \cdot \mathbf{V_C}) \psi] - \frac{1}{\tau_f} \psi - \frac{1}{\tau_d} \psi \tag{5.9}$$

D_{xx} is the spatial diffusion coefficient and is taken as $D_{xx} = \beta D_0 (R/R_0)^{\delta}$, if necessary with a break $\delta = \delta_{1,2}$ below or above the reference rigidity R_0, where the factor β is a consequence of a random walk process, while $\dot{p} \equiv dp/dt$ is the momentum loss rate. For a given halo size the diffusion coefficient as a function of momentum and the reacceleration or convection parameters is determined by B/C ratio data. For the case of reacceleration the momentum space diffusion coefficient D_{pp} is related to the spatial coefficient D_{xx} [161] (see formula (2.32)), where $\delta = 1/3$ for a Kolmogorov spectrum of interstellar turbulences and $\delta = 0.5/0.6$ for a Kraich and Plain Diffusion spectrum respectively. The distribution of cosmic ray sources [138,140] is chosen to reproduce the cosmic ray distribution determined by analysis of γ-ray data [36]. The injection spectrum is assumed to be a power law in momentum $dq(p)/dp \propto p^{-\gamma}$, as will be discussed in the following. Energy losses [140] for nucleons by ionization and Coulomb interactions are included, and also ionization, Coulomb interactions, bremsstrahlung, inverse Compton, and synchrotron. For electrons the total magnetic field distribution

is adjusted to match the 408 MHz synchrotron longitude and latitude distributions. This is in agreement with interstellar field estimates [140] and other magnetic field models [132,141].

5.6 Iniection Spectra and Diffusion Coefficients

The source function distribution for primary cosmic rays has already been discussed, it was explained that the best choice fall on a power law in momentum

$$\frac{dQ(E)}{dE} \propto p^{-\gamma} \tag{5.10}$$

For our purposes we need to find a connection between the previous relation and the cosmic ray density per unit of total particle momentum $\psi(p, \mathbf{r}, t)$. We notice that $dE/dp = \beta/A$, where A is the mass number and E is the kinetic energy per nucleon, so that we can write the previous relation in terms of the momentum

$$\frac{dQ(p)}{dp} \propto \frac{\beta}{A} p^{-\gamma} \tag{5.11}$$

If now we go on using the relation between the cosmic ray density and the flux $dQ(p) \propto (c/4\pi)\beta s(\mathbf{r}, p)dp$, with $s(\mathbf{r}, p)$ indicating the proper source term, we can say that the injection spectrum enters the propagation equation in the following way

$$\frac{\partial \psi}{\partial t} = s(\mathbf{r}, p) \qquad \frac{\partial s}{\partial p} \propto p^{-\gamma} \tag{5.12}$$

Since the rigidity $R = p/Z$ is the most likely parameter governing the propagation and escape of particles moving in the galactic magnetic field, it is preferable to replace the previous equation with

$$\frac{\partial \psi}{\partial t} = s(\mathbf{r}, R) \qquad \frac{\partial s}{\partial R} \propto R^{-\gamma} \tag{5.13}$$

In GALPROP this quantity is implemented as $\frac{\partial s}{\partial p} \propto (\frac{R}{R_0})^{-\gamma}$ to take into account possible breaking in the injection spectrum at a reference rigidity R_0.

In detail, the parameter R_0 corresponds to the galdef parameters *nuc_rigid_br#* that is the reference rigidity for nuclei injection index (in other words, it is the energy position of the break in the considered spectrum), where # stands for the number of index introduced;*electron_rigid_br#* is the reference rigidity for electron injection index and *positron_rigid_br#* is the reference rigidity for positron one. They are all expressed in MV (see Fig. 5.6). We can also introduce more than one reference rigidity, that is we can simulate more breaks in the particles or nuclei spectra and we can specify for each species the reference rigidity through the galdef parameter

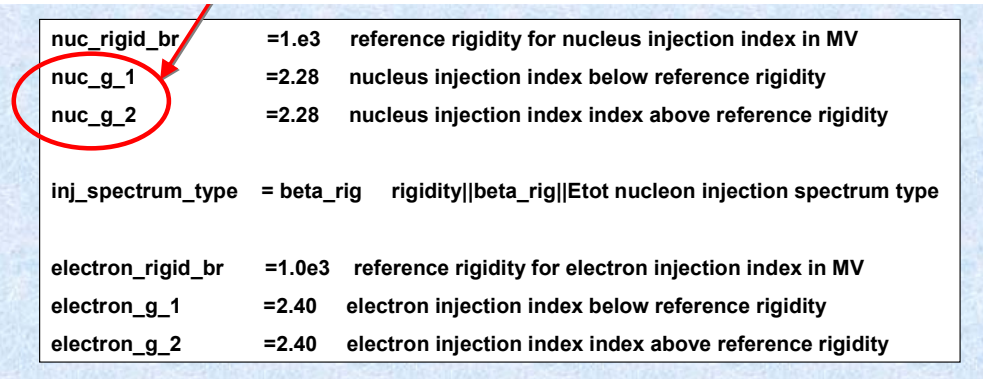

Figure 5.6: *Section of a galdef file containing the parameters associated to injection spectra[189].*

nuc_rigid_br#_0Z_0A, where Z and A define the nucleus identity. GALPROP gives also the possibility of introducing the nucleus or particle injection index $\gamma(R)$, one for each energetic range defined through the break values: the corrisponding parameters in this case are *nuc_g_#*, *electron_g_#* and *positron_g_#* is the positron injection index , in this case we can't specify for each nuclear species its injection index through the parameter, we must use the same index for all of them, we will discuss in the following section the way we use to overtake this limit of the software.
The secondaries are generated by a source term that enters the propagation equation as

$$s_{sec}(\mathbf{r}, p) = \beta c \psi_{prim}(\mathbf{r}, p)[\sigma^{(H)}(p) n_H(\mathbf{r}) + \sigma^{(He)}(p) n_{He}(\mathbf{r})] \tag{5.14}$$

where the production cross sections that are relevant for spallation are introduced. Here we consider only the production on Hydrogen and Helium targets, with the ψ_{prim} being the progenitors density and n_H, n_{He} the distribution of Hydrogen and Helium in the interstellar medium, as discussed previously.
The diffusion mechanism has already been treated in detail in Chapter 2, where it was introduced in the complete transport equation through the term

$$\nabla \cdot (\mathbf{D} \nabla N_j) \tag{5.15}$$

and in the GALPROP propagation equation via the term

$$\bar{\nabla} \cdot D_{xx} \bar{\nabla} \psi \tag{5.16}$$

Here $\mathbf{D}$ and D_{xx} represent the diffusion coefficient: this coefficient and the momentum diffusion coefficient have been deduced for cosmic ray particles that are scattered by random hydromagnetic waves propagating along the regular magnetic field H_0. Restricting our attention to a power law energy spectrum in wavenumber k we can

write the wave energy density as

$$W(k) = \frac{wH_0^2 L}{4\pi(1-a)}(kL)^{(a-2)} \tag{5.17}$$

where a is a constant, L is the principal scale of the turbolence with $kL \geq 1$ and $w = \frac{4\pi}{H_0^2}\int_{1/L} W(k)dk$ characterizes the turbolence level, being equal to the ratio of magnetohydrodynamic wave energy density to magnetic field energy density. We assume that the energy density is the same for both the waves propagating in opposite directions along the regular magnetic field. This imply that the effective velocity of the convective particle transport by the wave vanishes, so that the only contribution to convection comes from the large movements of the medium. It is worth to notice that the diffusion coefficient is related to two important quantities: the mean time taken by a particle to get a certain height H in the Galaxy

$$t_H \propto \frac{H^2}{\mathbf{D}} \tag{5.18}$$

and the mean distance from the galactic plane

$$< x >= 2\sqrt{\frac{\mathbf{D}t}{\pi}} \propto \sqrt{\mathbf{D}t} \tag{5.19}$$

This way the diffusion mechanism can be studied through the diffusion coefficient

$$\mathbf{D} = k_0 \beta R^{2-\kappa} \tag{5.20}$$

that we can rewrite, considering what we said above, as

$$D_{xx} = \beta D_0 (\frac{R}{R_0})^{\delta} \tag{5.21}$$

where R is the rigidity and R_0 is a reference rigidity introduced for an eventual break. It corresponds to the galdef parameter D_rigid_br and is expressed in MV. The parameter D_0 is a normalization factor that corresponds to the galdef parameter $D0\_xx$ when isotropy is assumed, otherwise we have to turn on the anisotropy $Diffusion\_aniso$ and introduce a second factor that is $D0\_zz$.

Then we have δ that is a free parameter of the model and corresponds to $D\_g\_\#$, i.e. the diffusion coefficient index below and above the reference rigidity, the symbol # indicates the break we consider (see Fig. 5.7).

In conclusion, we reduced the problem of diffusion to two fundamental parameter, i.e. D_0 and δ (plus R_0 in case of breaks).

The convection mechanism, as the previous one, has been treated in detail in Chapter 2; the term corresponding to this process was introduced in the transport equation as

$$-\nabla \cdot (\mathbf{V_C} N_j)$$

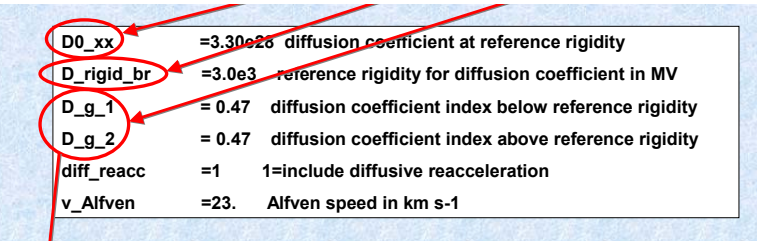

Figure 5.7: *Section of a galdef file containing the parameters associated to the diffusion process[189].*

and in GALPROP model as

$$-\bar{\nabla} \cdot \mathbf{V_C} \psi$$

where $\mathbf{V_C}$ is the galactic wind velocity, that is characterized by a linear increasing on the z direction and produce a particle energy diluition, i.e. a kind of energy loss called adiabatic deceleration.

The convection process can be turned on in GALPROP using the parameter *convection*; the velocity variation along z, $\frac{dV}{dz} > 0$, is included in the galdef file via the parameter $dvdz\_conv$ that is expressed in km/skpc and runs from 0 to 10, while the convection velocity is encoded in galdef parameter $v0\_conv$ through the relation $v\_conv = v0\_conv + dvdz\_conv * dz$ (see Fig. 5.8).

The reacceleration process, as said in Chapter 2, comes from the additional term in

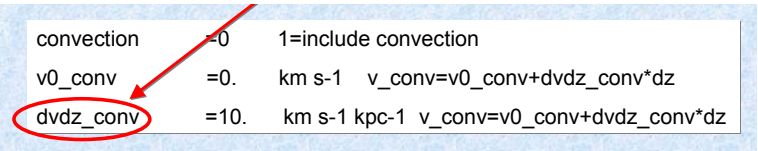

Figure 5.8: *Section of a galdef file containing the parameters associated to the convection mechanism[189].*

the transport equation

$$\frac{1}{p^2}\frac{\partial}{\partial p}[p^2 D_{pp}\frac{\partial N_j}{\partial p}] \tag{5.22}$$

and in GALPROP via the corresponding term

$$\frac{\partial}{\partial p}p^2 D_{pp}\frac{\partial}{\partial p}\frac{1}{p^2}\psi \tag{5.23}$$

where D_{pp} is the diffusion coefficient in the momentum space.

We can write a relation between the diffusion coefficients in the parameters space using the following equation

$$D_{pp}D_{xx} = \frac{4p^2 V_A^2}{3\delta(4-\delta^2)(4-\delta)w} \tag{5.24}$$

where w, already defined, characterizes the level of turbulence while V_A is the model parameter called Alfvén speed. The reacceleration affects mainly the light elements and fundamental particles and can be used in the run through the parameter v_Alfvn in the range 7 to 117 and is expressed in km/s (see Fig. 5.9).

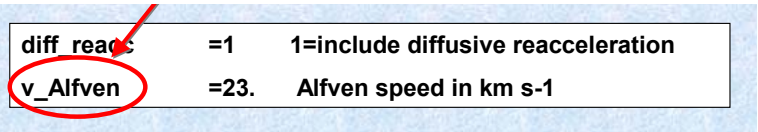

Figure 5.9: *Section of a galdef file containing the parameters associated to the reacceleration process[189].*

5.7 Modulation in the Heliosphere

The Heliospheric or Solar Modulation is a process that alters cosmic rays up to $\simeq 20$ GeV/n then beacuse of it their abundance is less then the IS one.
The propagation equation can be modified to take in account this phenomenon in this way: the acceleration due to the diffusion mechanism is omitted, the convection velocity is substituted with the solar wind velocity that is then kept constant, finally a spherical symmetry is assumed with a weak radial variation and power law energy spectra[134].
We then obtain the following relation

$$D_{xx}\frac{\partial^2\psi}{\partial r^2}+\frac{2D_{xx}}{r}\frac{\partial\psi}{\partial r}-\mathbf{V_C}\frac{\partial\psi}{\partial r}+\frac{2\mathbf{V_C}p}{3r}\frac{\partial\psi}{\partial p}=0 \tag{5.25}$$

If we now neglect the first and third terms, i.e. we make the strong field assumption, we obtain

$$\frac{\partial\psi}{\partial r}+\frac{\mathbf{V_C}p}{3D_{xx}}\frac{\partial\psi}{\partial p}=0 \tag{5.26}$$

Moreover if we consider the quasi linear approximation we can rewrite the diffusion coefficient as

$$D_{xx}=k_0\beta p \tag{5.27}$$

and then

$$dE=\frac{\mathbf{V_C}}{3k_0}dr \tag{5.28}$$

This way the final solution depends only on one parameter

$$E(r)=E_R+|eZ|\,\phi\cdot(r-R) \tag{5.29}$$

GALPROP parameter	physical meaning
$DM\_double1$	local DM density
$DM\_double2$	DM mass
$D\_double9$	annihilation cross section
DM_int0	DM halo profile
$DM\_double3/4$	e^+ kinetic range/BR for annihilation
$DM\_double5/6$	e^- kinetic range/BR for annihilation
$DM\_double7/8$	$\bar{p}$ kinetic range/BR for annihilation

Table 5.1: GALPROP file parameters associated to DM: density, mass, annihilation cross section, halo profile and branching ratios of the annihilation channel.

that is the solar modulation parameter

$$\phi = \frac{\mathbf{V_C}}{3k_0} \tag{5.30}$$

It runs from 325 to 1500 MV.
The output file provided by GALPROP is a .gz one. To obtain a more easy to analyze format, we used a python routine namely $plot_galprop.py$. The procedure implemented in this code read the FITS files produced by GALPROP and output data as text tables, compatible with the analysis software we use i.e. Mathematica. What we have to specify, for each job submitted to this routine, is the name of the GALPROP output and the value of the solar modulation we want to adopt.

5.8 Dark Matter in Galprop

As discussed in Chapter 3, the indirect Dark Matter research is based on CR anomalous components detection, due to DM annihilation in the galactic halo. The reaction associated to this process is

$$\chi + \chi \longrightarrow q\bar{q} + W^+W^- + ... \longrightarrow \bar{p} + e^+ + \gamma + \nu$$

In GALPROP we can use a set of routines ($gen\_DM\_source.cc$) to assign different values to the parameters associated to Dark Matter properties. We can distinguish between the astrophysical and the one related to particle production via DM decay (10 in all), they are sketched in the following table:

Finally the source functions for $e^+, e^-, \bar{p}$ can be turned on/off using the GALPROP parameter $DM\_positrons(electrons, antiprotons) = 0/1$[134]. We will return on DM

parameter discussion at the end of this work, to show some DM signal in $\bar{p}/p$ channel, and to observe which of them mainly affect our propagations.

Chapter 6

Analysis of Nuclear Ratios: a Comparison between Data and Theory

This chapter is entirely devoted to original results. The main task that we achieved in the following paragraphs is to find the set of propagation parameters that better describe the cosmic rays preliminary observations coming from AMS-02. As already pointed out in the introduction, it will be described in detail the method used, underlying all the adopted approximation in order to present a reproducible analysis scheme. The energy range, chosen from 1 MeV to 10 TeV, is the most interesting from a propagation point of view. These energies contain the interval covered by previous experiments, making this work particularly relevant for a comparison between the results gained before and by the AMS-02 experiment. Moreover, we want to debate here about the associated predictive power for the indirect DM search, making a comparison between what obtained from GALPROP and from PPPC4DMID.

6.1 Analysis Strategy

In this section we want to explain in a complete way the analysis strategy adopted for the identification of a propagation set with GALPROP. A schematical view of this procedure is shown in Figure 6.1.

As we can see from the scheme, the starting point for the anlysis is a set of experimental data, coming from AMS-02, that includes nuclei fluxes and ratios: $\bar{p}$/p, He, H/He, B, C, B/C, Li, O, C/O. A complete description of these preliminary data is given in Table 6.1, here the energy range and the number of measurements avaible

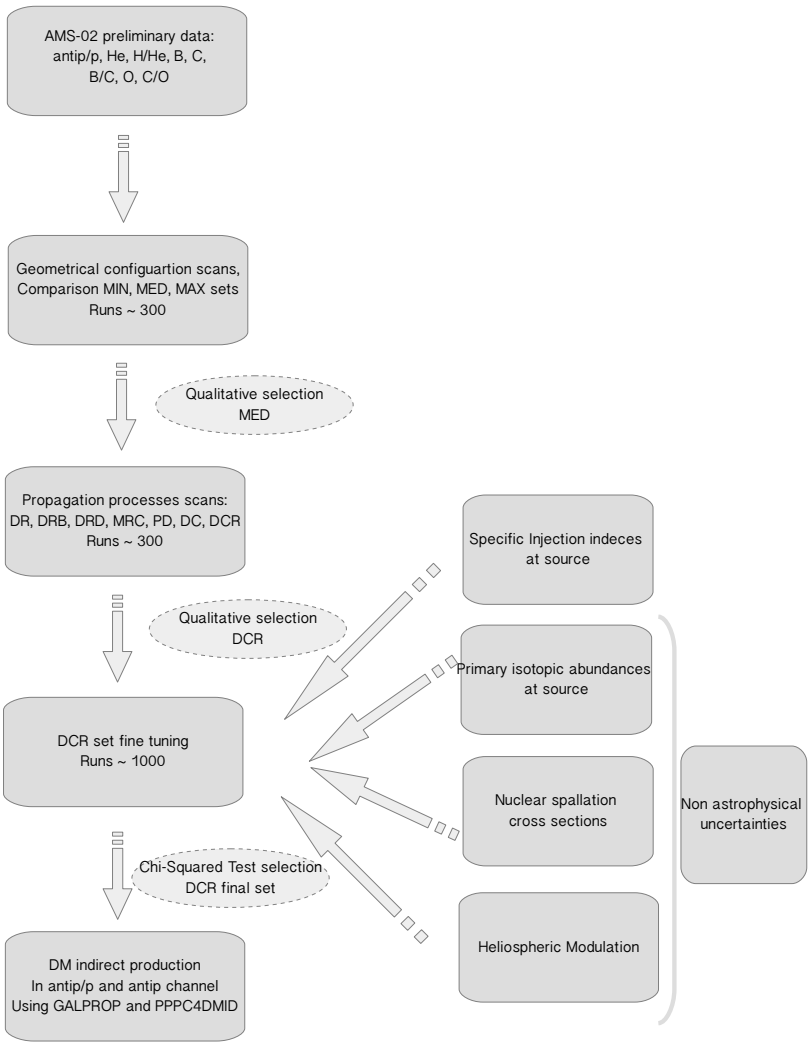

Figure 6.1: Schematical view of the analysis strategy of this work. Starting from AMS-02 preliminary data, we made a first scan to study the geometrical parameters (a MED set was selected), a second scan to study the propagation processes (a Diffusion-Reacceleration-Convection set was selected) and a third scan to fine tune the DCR set obtained. Along with these scans we made two important studies: one related to specific injection indeces at source for nuclei propagation (this option isn't implemented in GALPROP); the other centred on the not astrophysical uncertainties that affect CR fluxes and ratio: isotopical abundances at source, nuclear spallation cross section and heliospheric modulation. The results obtained were used as input for the study of DM indirect signal, done with two different software: GALPROP and PPPC4DMID.

spectra	energy range [GeV]	number of points
$\bar{p}$/p	1÷250	58
He	1÷2500	87
H/He	1÷1600	69
B	0,5÷700	18
Li	0,5÷1000	49
C	0,5÷1100	53
B/C	0,5÷1100	35
O	0,5÷1100	52
C/O	0,5÷1100	35

Table 6.1: AMS-02 measurement for nuclei fluxes and ratios. Here we report the number of measurement avaible and the energy range for E<200 GeV. As one can see we didn't use the protons, indeed for this measure we have only preliminary results and the analysis is under further investigation by the AMS-02 collaboration.

are provided. The associated error of these preliminary measures is very little, for this reason in the first part of our analysis we used this feature to discard or accept the propagation configuartions, just looking at the comparison with preliminary data, without using a statistical approach.

The nuclei fluxes considered are obtained as sum of different isotopes. We can express the relative abundance of nuclei isotopes through the isotopical ratio as shown in Figure 6.2. We want here underline that these fluxes are produced using a GALPROP simulation and that the results obtained are strongly dependent on the propagation configuration chosen, as will be described in the following.

Finally we want here to discuss about the set (MIN, MED, MAX) used for the first comparison of the geometrical scan (described in detail in the next section). We built these sets using for GALPROP parameters values found in literature. In particular the set name refers to the fluxes and ratios intensity obtained and not to the values fixed for propagation parameters, as we can see from Table 6.2 where the parameters values for these three sets are reported. These sets were used at the beginning of our work as reference in GALPROP parameter space.

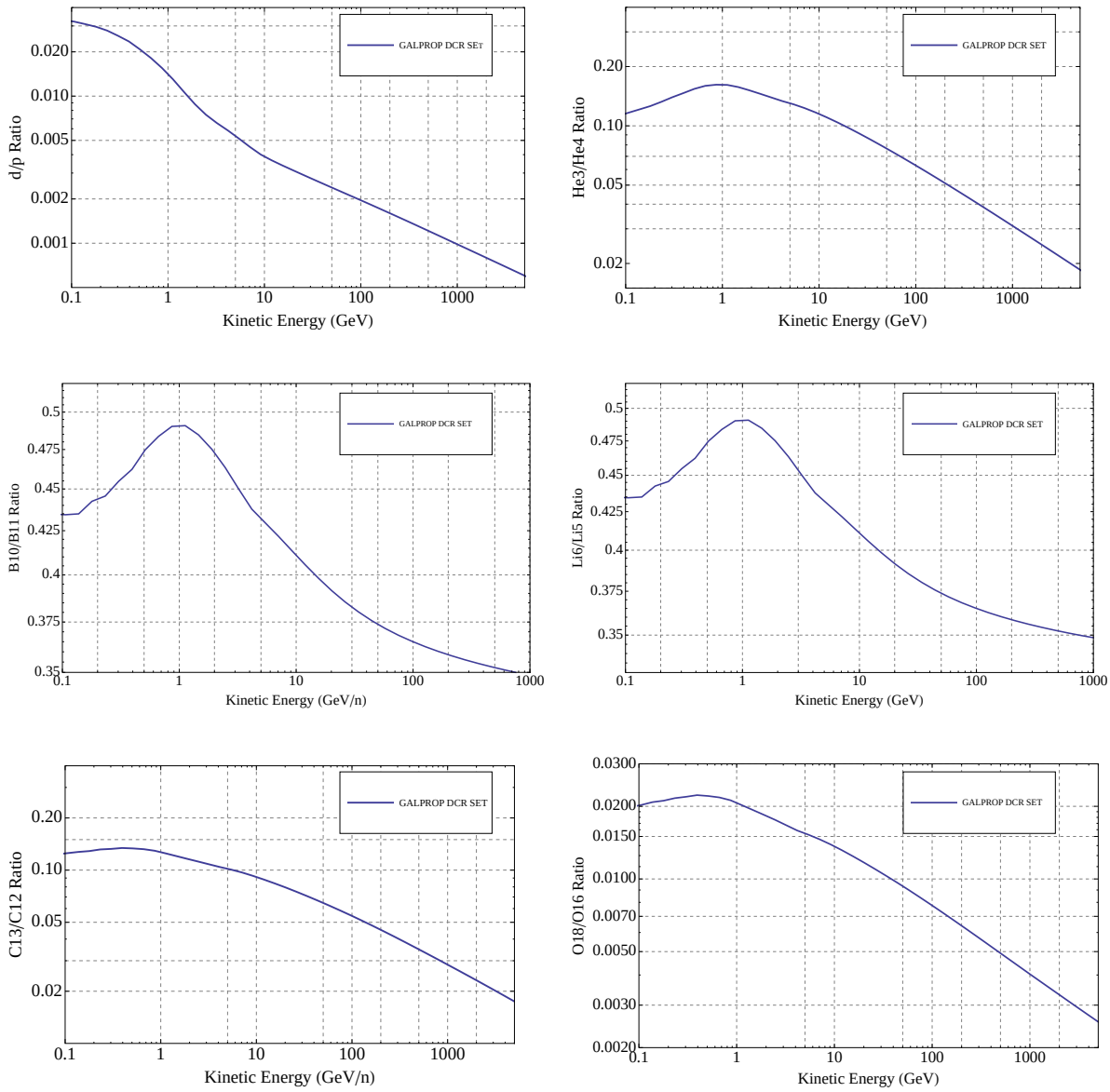

Figure 6.2: Isotopical ratio obtained with GALPROP for the nuclei considered in the following analysis: d/H(upper left plot),He^3/He^4(upper right plot),B^{10}/B^{11}(middle left plot),Li^6/Li^7(middle right plot),C^{13}/C^{12}(lower left plot) and O^{18}/O^{16}(lower right plot).

set	D_0	$\delta_{1,2}$	γ_1	γ_2	V_A	v0_conv	dV_C/dz
MIN	0,8	0,55	1,92	2,39	12	13,5	10
MED	2,7	0,7	1,92	2,39	40	12	5
MAX	6,7	0,34	1,92	2,39	110	0	0

Table 6.2: Classification of the three starting configuartion that we built using values taken from literature. These three set were used for a comparison in the geometrical scan and as reference for next comparison with more structured propagation configurations.

6.2 Choice of the Propagation Set with Galprop

The most simple approach for the selection of the best propagatio set is a combinatory scan of the parameters grid. The starting point for this study is to make some tests, using a reasonable set of parameters. All the parameters are included in a datacard, that is the file GALPROP uses to realise the propagation of CR from the source up to the top of the atmosphere. Using this parameters grid we wanted to obtain a best fit to the AMS-02 data for what concerns nuclear spectra and ratios. Concerning the parameter range, we were mainly guided by theoretical values found in literature, where precise limits for a reduced chi-squared were obtained. In the following we will explain in detail the procedure used for tuning the set, trying to narrow the parameters ranges and improve CR simulations.

6.2.1 Galaxy Geometry and Propagation Mechanisms

The first thing we did to find a good propagation set, as already said, was to make a scan of a parameters grid. In GALPROP we can divide the avaible parameters in different groups, acording to their role in the propagation. At first we focused our scan on the geometrical parameters, in a 2D configuration, maintaining all the other ones unchanged. The main avaible geometrical parameters in GALPROP are the maximum galactocentric radius (r_{max}) for 2D case and the galactic halo height (z), both expressed in kpc. As sketched in Table 6.3 we chose different combination of these two first analysis sample parameters, using the B/C ratio fit and the single B and C fluxes.

Fitting the measured B/C ratio is a standard procedure to derive the propagation parameters. Its importance resides in the entirely secondary origin of boron and in the measurement accuracy that is better than for other ratios. Moreover, the production cross sections from the main progenitors CNO, are better known for boron than for the

z [kpc]	**r** [kpc]
4	10,20,30
1,4,7,15	20

Table 6.3: Geometrical parameters values used as the first analysis sample for the maximum galactocentric radius and the galactic halo height respectively.

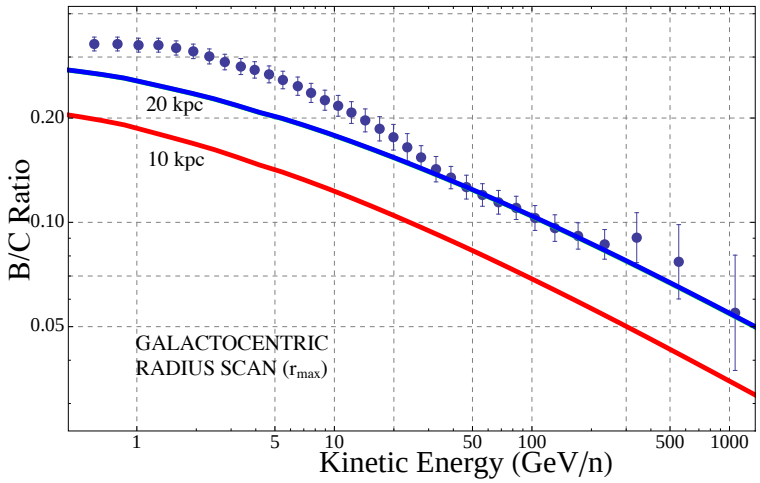

Figure 6.3: Boron over Carbon ratio for different galactocentric radii. The red curve corresponds to a 10 kpc radius while the blue one is obtained for a 20 kpc radius. As one can see the too low choice is clearly wrong, since it produces a too lacking spectrum.

Be and Li (the other almost completely secondaries that share the same parent nuclei). In Figures 6.3 and 6.4 some examples of geometrical parameter variation are shown. In Fig. 6.3 the variation of the B/C ratio is reported, as a function of increasing values of the r_{max} parameter: in particular the red curve corresponds to a 10 kpc radius while the blue one corresponds to a 20 kpc radius.
The other plot (Fig. 6.4) shows the variation of the B flux according to the variation of the halo height: the red line corresponds to a 1 kpc height, the green curve corresponds to a 4 kpc, the blue one to a 7 kpc height and finally the light blue one is 15 kpc.
Then we extended this geometrical parameters comparison to all avaible nuclei and ratios, not only to B and B/C. Finally, from the z-r analysis our choice for z and r_{max} fell respectively on

$$z = 4 \quad Kpc$$

and

$$r_{max} = 20 \quad Kpc$$

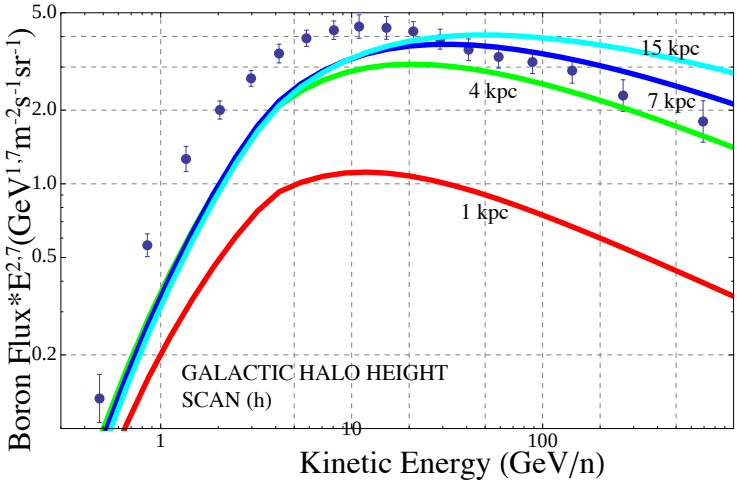

Figure 6.4: Boron flux for different values of the galactic halo height: the red line corresponds to a 1 kpc height, the green one corresponds to 4 kpc, the blue one corresponds to 7 kpc and finally the light blue one corresponds to 15 kpc. We can observe that a 1 kpc height is too little and produce a too low flux.

After we compared this geometrical set (red line) in Fig.6.5 with the three defined set (i.e. MIN in yellow,MED in black and MAX in purple) (see Table 6.2), we observed that what we chose was similar to a MED set.

After fixing the geometrical parameters, we started investigating the ones related to the propagation mechanisms. In Table 6.4 we outline all the mechanism taken into account for the scan of the parameter grid i.e. diffusion (D), reacceleration (R), convection (C), possible breaks (B),minimal scenario (M) and plain case(P).

Specific values for the spatial diffusion coefficient, the diffusion index, the injection index, for Alfvén velocity, convection velocity and for the convection velocity gradient were chosen, according to the mechanism we were probing, as sketched in the Table 6.4.

For all the mechanisms listed above the main propagation scheme was used, maintaining the parameters related to DM production unchanged, the spatial ones (fixed before), the energy range for the fluxes simulation and the reference rigidity for the spectral breaks.

An example of result obtained for the DR I set (see Table 6.4), using the B over C ratio, is shown in Fig. 6.6: here the red curve represents the GALPROP propagation while the blue dots are the AMS-02 preliminary data. The first plot was obtained using a modulation of 450 MV while in the second one we used a 1500 MV modulation. We can observe that the two plots don't differ too much at high energies, because solar modulation plays a pronounced role only below 10 GeV. A second example is given in

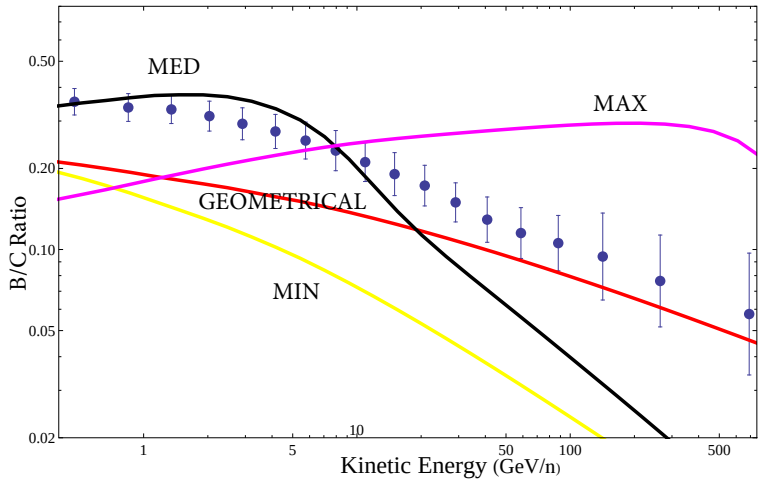

Figure 6.5: Comparison, for the B/C ratio, between MIN (yellow line), MED (black line), MAX (purple line) sets (as defined in Table 6.2) and the geometrical set characterized by a galactic radius of 20 kpc and a halo height of 4 kpc (red line). As we can see from the plot the geometrical set obtained in the first configuartions scan is similar to a MED set.

Mechanism	D_0	$\delta_{1,2}$	γ_1	γ_2	V_A	$v0\_conv$	dV_C/dz
DR I	6,1	0,34	2,43	2,43	30	0	10
DR II	3,3	0,47	1,8	2,28	23	0	10
DRB-Kol	6,2	0,33	1,93	2,43	36	12	10
DRD	2,9	0,5	1,91	2,4	22	12	10
MRC-Kol	4,4	0,33	2,43	2,43	17	12	10
MRC-Kraich	4,3	0,5	2,25	2,25	40	12	10
PD I	3,1	0,6	2,16	2,16	0	0	0
PD II	1,8	0,5	1,8	2,25	0	0	0
DC	2,5	0,6	2,46	2,46	0	13,5	10
DCR	3,1	0,33	1,92	2,39	30	13,5	10

Table 6.4: Classification of propagation configurations according to the main combinations of physical galactic processes at source: DR (diffusion+reacceleration), DRB-Kol (diffusion+reacceleration+break+$\delta_{Kolmogorov}$), MRC-Kol (minimal+reacceleration+convection+$\delta_{Kolmogorov}$), MRC-Kraich (minimal+reacceleration+convection+δ_{Kraich}), PD (plain+diffusion), DC (diffusion+convection), DCR (diffusion+convection+reacceleration). The configuration tagged with I and II refer to different values for $D_0, \delta, \gamma, v0\_conv$ and dV_c/dz parameters.

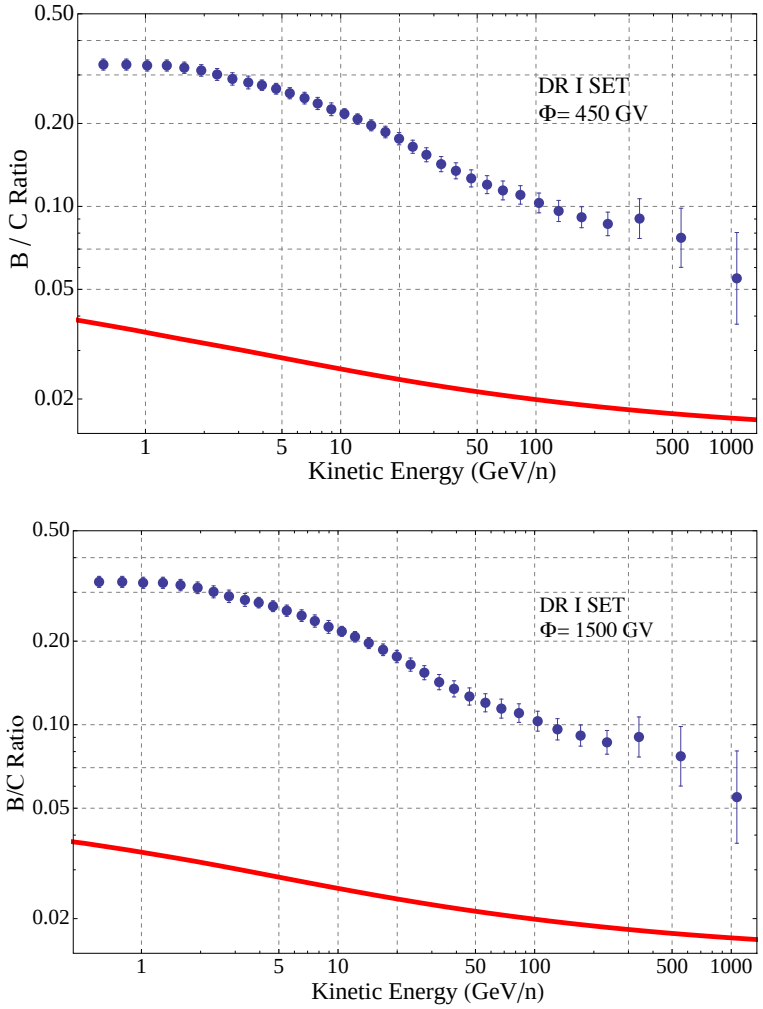

Figure 6.6: B/C ratio for the DRI set (as defined in Table 6.4) with two different solar modulations: 450 MV (upper plot) and 1500 GV (lower plot). As one can see the DR I configuration, for both the solar modulation values, is not capable to reproduce AMS-02 data.

spatial dimensions	2
energy range	$10^2 \div 10^7$ MeV
z	4 Kpc
r_{max}	20 Kpc
DM core radius	1
DM local density	0,35
DM mass	2000
DM annihilation cross section	$3 \cdot 10^{-24}\ cm^{-3}s^{-1}$
DM profile	0
DM e^+, e^- width	300
DM e^+, e^- branching	50
DM $p, \bar{p}$ width	400
DM $p, \bar{p}$ barnching	50

Table 6.5: List of the main propagation scheme parameters maintained unchanged: spatial, energy and DM ones.

Fig. 6.7: here we present a MRCKol set (see Table 6.4). As in the previous plot, the red curve is the GALPROP simulation and the blue dots are the data. Also in this case we show two solar modulation cases, i.e. 450 and 1500 MV. We can observe that also in this set there is a really little variation due to the solar modulation in the low energy range.

Finally we tuned the remaining parameters: the damping constant, the reference rigidity break for injection index the source parameters and the solar modulation (see Table 6.6), making different attempts, for a total amount of 324 runs.

Once obtained all the possible parameter permutations for the different mechanisms considered, we focused on the selection of the best fitting ones. Starting from the usual B/C ratio, we compared all the fluxes and ratios in order to use these multiple constraints to find the most suitable sets, proceeding with their fine tuning.
In Figure 6.8 is shown the Boron over Carbon ratio and the Helium flux for the SET4-MRCKol configuration (see Table 6.4 and 6.6): in this example a 750 MV modulation is used. We can observe that not only in the low energy region, affected by solar modulation, but also in the high energy window there is not good agreement with preliminary data.

In Fig. 6.9 the Carbon and Oxygen fluxes obtained from the SET5-PD II (see Ta-

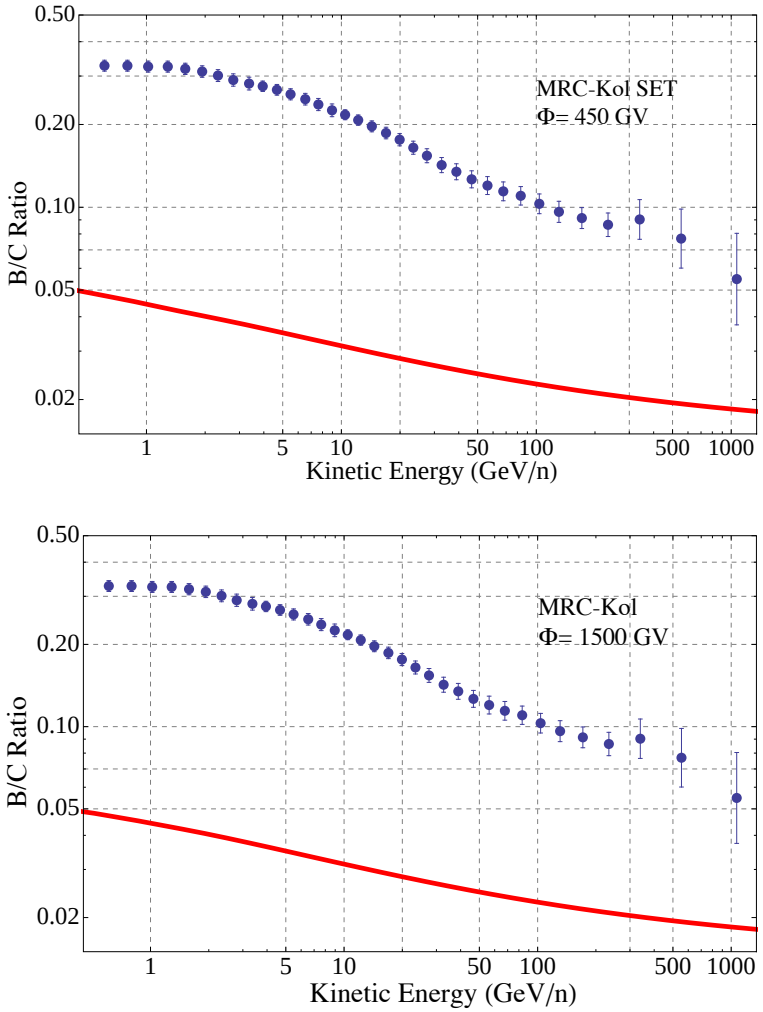

Figure 6.7: B/C ratio for the MRC-Kol set (see Table 6.4) with two different values for solar modulations, 450 MV (upper plot) and 1500 MV (lower plot). We can clearly observe the discrepancy between AMS-02 data and GALPROP simulation.

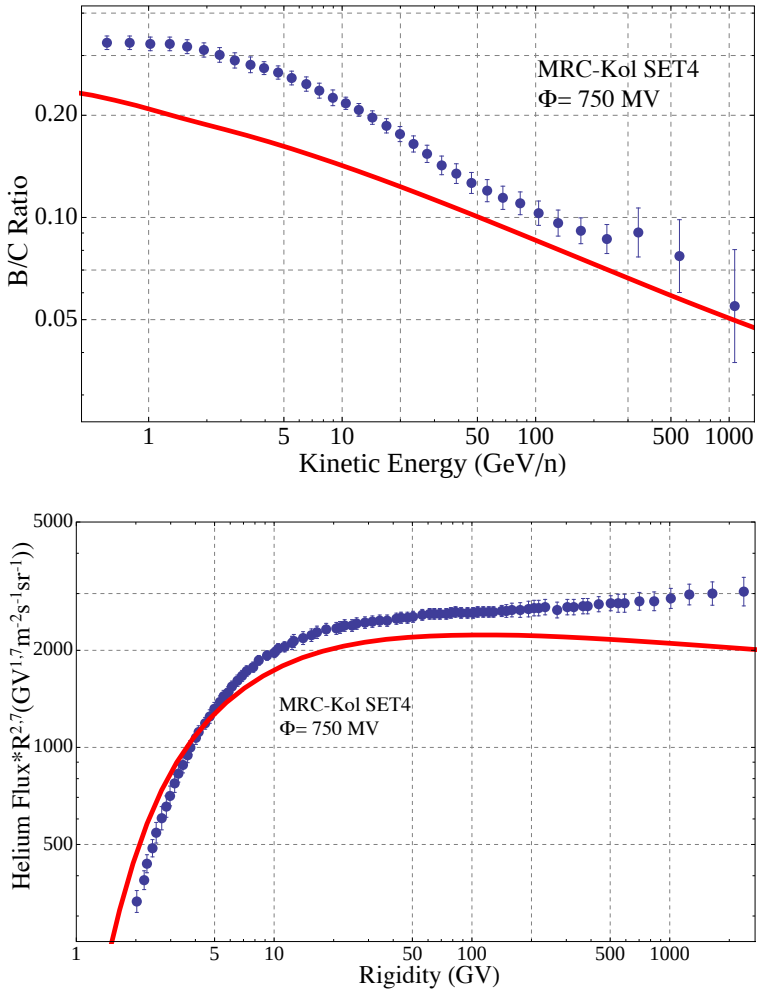

Figure 6.8: B/C ratio (upper plot) and Helium flux (lower plot) for the MRC-Kol SET 04 (see Table 6.4 and 6.6) with a solar modulations of 750 MV. We can clearly observe the discrepancy between AMS-02 data and GALPROP simulation.

parameters	SET 1	SET 2	SET 3	SET 4	SET 5	SET 8
g	$0.0056 \div 0.085$	0,006	0,08	0,85	0,039	0,006
R_0	$10^3, 5 \cdot 10^4$	$10^3, 5 \cdot 10^4$	$10^3, 5 \cdot 10^4$	$10^3, 5 \cdot 10^4$	$10^3, 5 \cdot 10^4$	$10^3, 5 \cdot 10^4$
α	0,5	2	2	2	0,8	0,5
β	1	5	5	5	2	1
ϕ	450,750,1500	750,1500	750,1500	750,1500	750,1500	750,1500

Table 6.6: Different propagation parameters sets. We combined the parameters shown: damping constant (g), R_0, α, β and ϕ (as defined in Chapter 5) with the propagation configuration reported in Table 6.2 i.e. for each SET we tested the configuration DR I, DR II, DRB-Kol, DRD, MRC-Kol, MRC-Kraich, PD I, PD II, DC, DCR.

ble 6.4 and 6.6) with a solar modulation of 750 MV are shown. The last example we propose here, is the one obtained with the DCR set (see Fig. 6.10). In this plot we can observe a really good agreement with the preliminary data, with an improvement in the low energy region w.r.t. the PDII case. We have to notice that here a 1500 MV solar modulation was used, as already said it affects the low energy region.

In the end from the comparison of all fluxes and ratios obtained with the tested sets, we decided to exclude DR, MRC and to select the DCR, PD and DC models. We can see from Figure 6.11 a qualitative disagreement for the DR and MRC sets (upper left and right plots), on the other hand for DCR, PD and DC configurations we observe an overall agreement (middle and lower plots).

Then we focused on the DCR one, going on with its fine tuning; in Table 6.7 the parameters values for this starting DCR set are reported. For the fine tuning of this DCR set we started changing all the propagation scheme parameters combinatorially to understand how strongly each change could modify fluxes and ratios. At the beginning, we divided the scan in eight sets in order to focuse on a defined number of parameters for each set. In the first set we chose to vary some parameters not tested before, such as the ones realted to the galactic magnetic field, the ones related to the gas that form the interstellar medium and the parameters connected to the solution method, used to solve the propagation equation in GALPROP. Along with these, we modified also a new parameter coming from the update version of the software (version 54.r2423), that is the diffusion coefficient in the z direction that gives the user the possibility to switch on an anisotropic diffusion in both r and z directions.

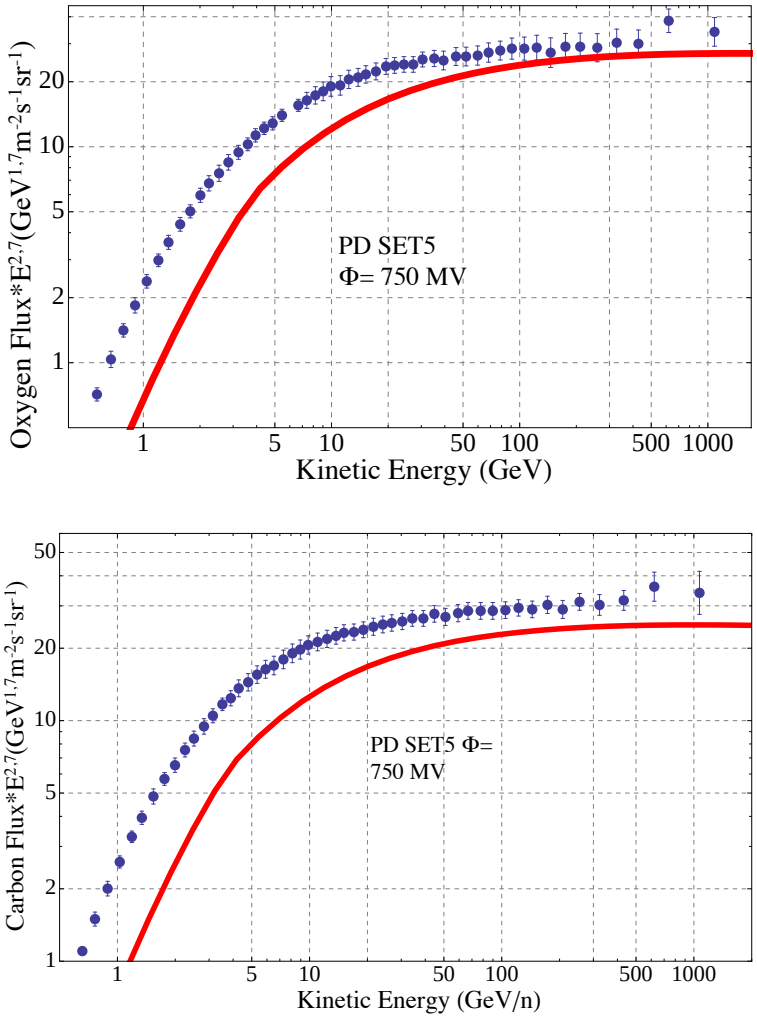

Figure 6.9: Oxygen (upper plot) and Carbon (lower plot) fluxes for the plain diffusion SET5 (see Table 6.4 and 6.6) with a 750 MV solar modulation. Both these sets can't reproduce AMS-02 data in the enrgy range explored.

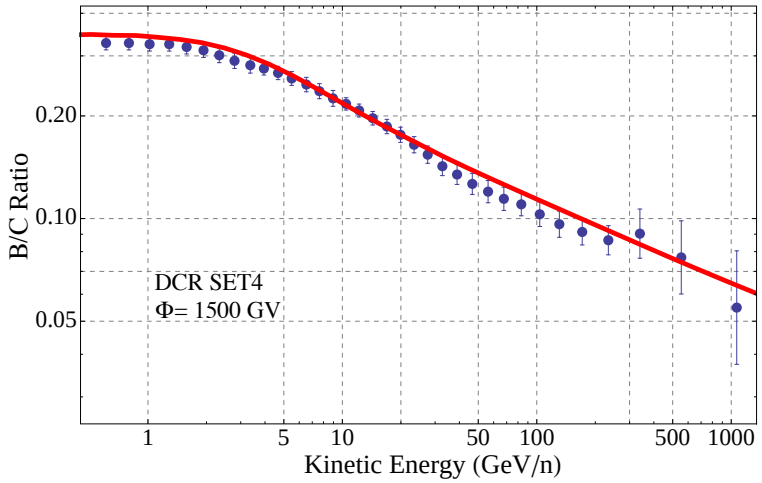

Figure 6.10: B/C ratio flux for the set including diffusion, convection and reacceleration mechanisms and a solar modulation of 1500 MV. We can observe a good agreement with AMS-02 preliminary data.

	DCR Set
z	4
r_{max}	20
γ_1	1,95
γ_2	2,39
D_0	$3{,}4 \cdot 10^{28}$
$\delta_{1,2}$	0,33
V_A	30
v0_conv	13,5
dV_C/dz	10

Table 6.7: DCR propagation configuration obtained from the first selection procedure. We combined the results froma ageometrical scan with different propagation configurations.

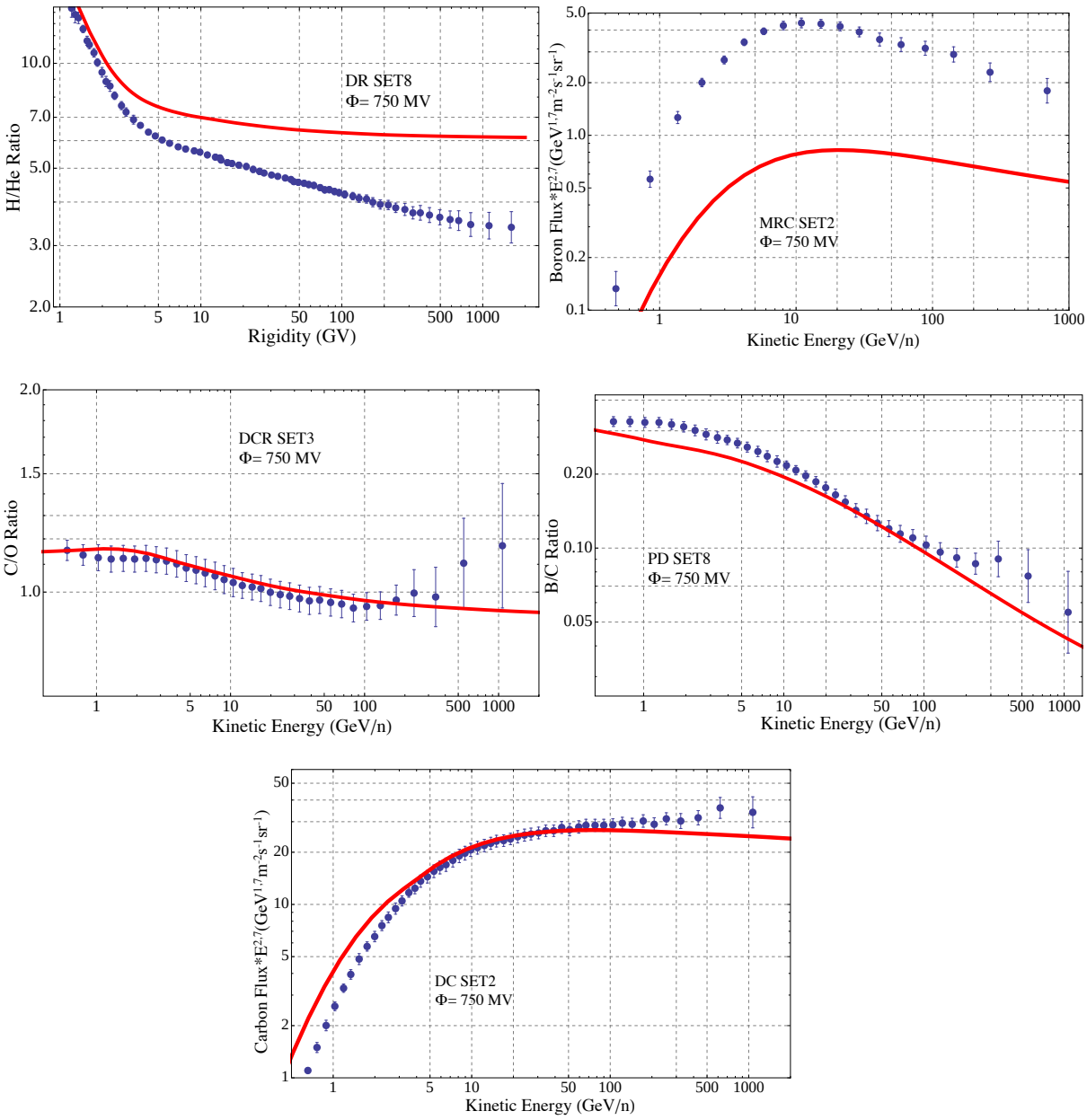

Figure 6.11: In this Figure we can observe different ratios and spectra obtained from different configuration schemes (sketched in Table 6.4 and 6.6): the DR configuration (upper left), the MRC (upper right), the DCR (middle left), the PD (middle right) and the DC (lower plot). For the first two configurations we can observe a qualitative good agreement with AMS-02 preliminary data, while for the last three we can see a different behaviour w.r.t. the data. For this reason we exclude in the following the DCR, PD and DC configurations, focusing in particular on the fine tuning of the DCR propagation configuration.

	DCR final set
z	4,06 Kpc
r_{max}	20 Kpc
$D_0(x)$	4,1 $\cdot 10^{28} cm^2$
$D_0(z)$	4,1 $\cdot 10^{28} cm^2$
$\delta_{1,2}$	0,34
V_A	$27 \div 30$ Kms^{-1}
v0_conv	12 Kms^{-1}
z0_conv	4 Kpc
R_0	10 GeV/n
z_0	0,2 Kpc
α	1,5
β	3
r_0	20 Kpc

Table 6.8: Final propagation configuration for the DCR set, after its fine tuning. The best fit value for the Alfvén velocity was substituted with V_A=16 Kms^{-1} according with the galactic synchrotron constraint suggested by Moskalenko et al.[119].

In the second set we introduced a further scan on the Alfvén velocity, the convection velocity, the injection indices, the diffusion indices and the parameters related to the source spatial distribution. In the third set we focused on the tuning of the injection indices and the diffusion coefficients, also testing plausible values for the solar modulation parameter, varying it from 600 MV up to 900 MV, as indicated by the AMS-02 measurements. We did the same for the next four sets; in particular, in the fourth one, we guessed a lower value for the largest atomic number in the nuclear reaction network, while in the last set we tried various possibilities for the dark matter parameters: this study will be discussed in the detail in the following.
After doing all these tests we compared the obtained results with the AMS-02 data, imposing again multiple constraints between data and GALPROP simulations, in order to achieve a proper best fit. The main parameters values for this sets are listed Table 6.6. Finally in Figure 6.12 we show respectively the Boron and Oxygen fluxes along with the H/He and B/C ratios, all obtained with the final DCR set (see Table 6.8) selected among all the tested set (with a 550 MV solar modulation): as usual the red line corresponds to GALPROP simulation, while blue dots are AMS-02 preliminary data.

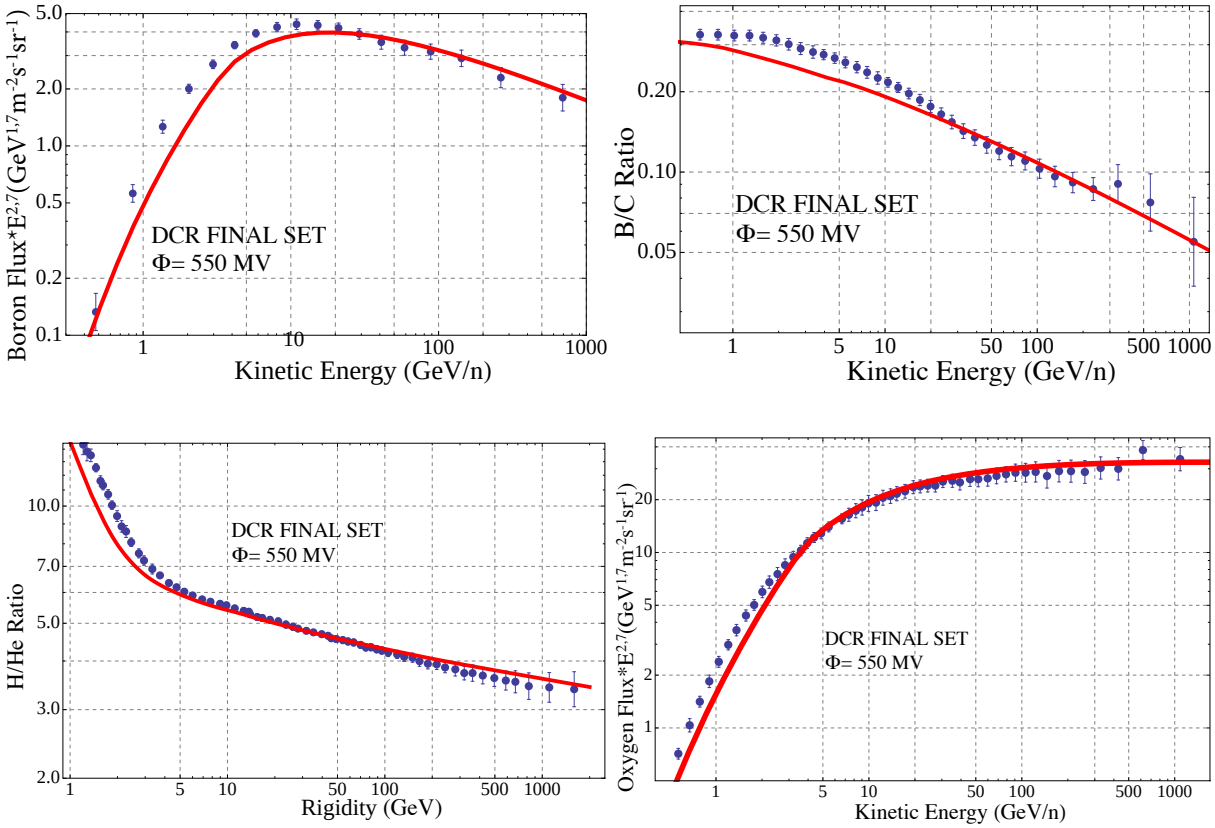

Figure 6.12: B flux (upper left plot), B/C ratio (upper right plot), H/He ratio (lower left plot) and Oxygen flux (lower right plot) all obtained with the DCR final set (described in Table 6.8) and with a solar modulation of 550 MV.

6.2.2 Spectral Indices

Till few years ago the injection index at source was tought to be the same for all protons and nuclei. Nevertheless recent experimental results coming from PAMELA and CREAM suggest that there exists a little difference among them.
In this section we want to explain the way we carried out a study on the specific indices to use for CR nuclei. The starting point for this task is the observation of nuclei fluxes, distinguishing between primary and secondary ones. Here we consider a Kolmogorov diffusion index that is $\delta = 1/3$: this choice is in good agreement with the observed B/C ratio (see Table 6.8). For the injection index γ we asume a mean value of 2,4. The theoretical form we can use to express a primary nucleus flux is

$$\Phi_{primary}(R) \propto R^{-(\gamma+\delta)} \simeq R^{-2,7} \tag{6.1}$$

For secondary nuclei instead we can write

$$\Phi_{secondary}(R) \propto R^{-[(\gamma+\delta)+\delta]} \simeq R^{-3} \tag{6.2}$$

Then we expect a secondary to primary ratio of the form

$$\frac{\Phi_{secondary}}{\Phi_{primary}} \propto \frac{R^{-[(\gamma+\delta)+\delta]}}{R^{-(\gamma+\delta)}} \propto R^{-\delta} \simeq R^{-1/3} \tag{6.3}$$

On the other hand, for primary to primary ratio we obtain

$$\frac{\Phi_{primary1}}{\Phi_{primary2}} \propto \frac{R^{-(\gamma_1+\delta)}}{R^{-(\gamma_2+\delta)}} \propto R^{-(\gamma_1-\gamma_2)} \propto R^{-\Delta\gamma} \tag{6.4}$$

Here $\Delta\gamma$ is the difference between injection indices for different nuclei. If such a ratio reach a plateau we can say that the γs are almost the same; whereas if not we can argue a difference. As stated above here we used a Kolmogorov diffusion index. Moreover the diffusion process is considered to be universal w.r.t. charge Z i.e. it doesn't depend on the nuclear species. For this reason, the origin of discrepancies between the measured power law and the theoretical one should reside in the injection index at source.
At first, in order to evaluate the index variation $\Delta\gamma$, we made an interpolation of the preleminary data. The power law used for this fit can be written as

$$\Phi(R) = C \cdot R^{\Delta\gamma} \tag{6.5}$$

We set up this function in the software Mathematica that automatically extrapolate the desired parameter. This fit was done in the energy region above 15 GeV/n to remove every problem related to solar modulation. In Figure 6.10 we can observe the discussed fit. In this example we show the Carbon flux and the H/He ratio. All

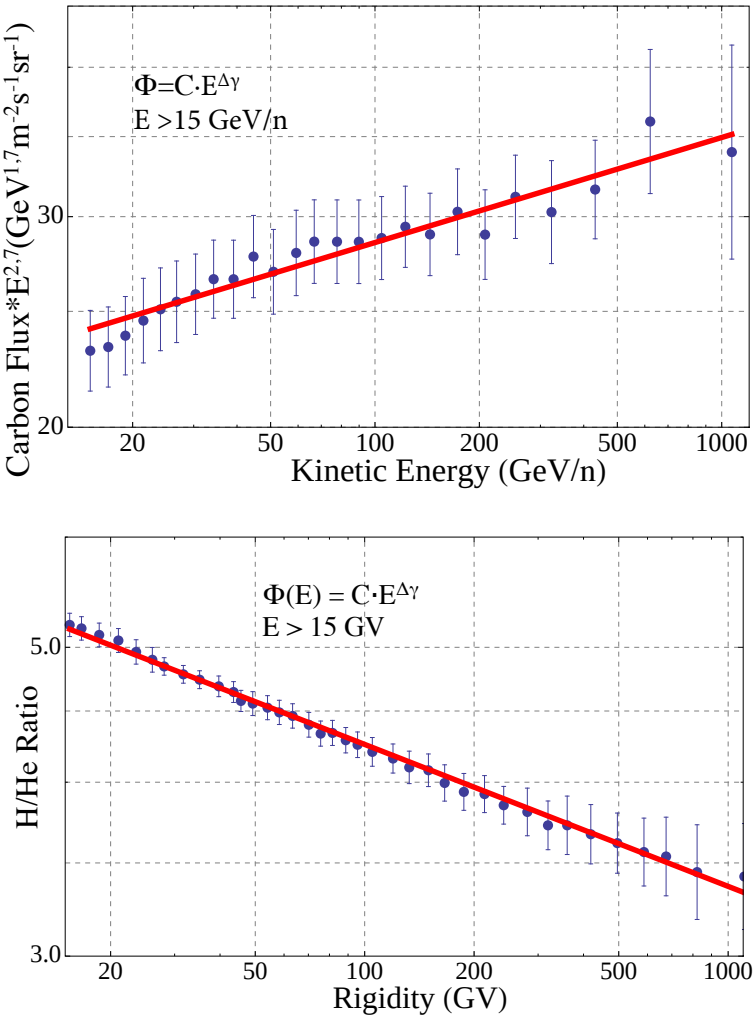

Figure 6.13: Backtracing procedure applied on Carbon flux (upper plot) and H/He ratio (lower plot), using the fit function $\Phi(R) = C \cdot R^{\Delta\gamma}$ on AMS-02 preliminary data. The extrapolation was done using the software Mathematica and led to the corrections for the nuclear injection indexes ($\Delta\gamma$).

	$\Delta\gamma$
p	-0,130
He	0,050
B	-0,227
C	0,088
O	0,101
B/C	-0,281
H/He	-0,125
C/O	-0,021

Table 6.9: Corrections to the nuclei injection indeces with an associated error of 0,005.

	γ
p	2,48
He	2,36
C	2,39
O	2,40
N	2,395
Ne,Mg,Si,Fe	2,395
common	2,395

Table 6.10: Nuclei injection indeces obtained after correction.

the results obtained with this procedure for the $\Delta\gamma$ are sketched in Table 6.9. Once obtained this $\Delta\gamma$ corrections, we applied them to the common index obtaining an index hierarchy to use as an input for GALPROP next propagations. The specific indices obtained after the correction are outlined in Table 6.10.

The possibility to use specific indices is important mainly because all the measured fluxes can be produced by different primary nuclei with different injection indices at source, thus producing a variation in the final flux considered. In Figure 6.14 as example the Boron flux (a secondary nucleus) is shown. We can observe the different contributions to the B flux: the Boron parent nuclei considered here are all propagated with specific indices as reported in Table 6.10. Also primary nuclei can receive contributions from heavier parent nuclei. For these nuclei, we can define the primariness, that is the ratio between the nucleus flux at source and the nucleus flux simulated at the TOA. In Figure 6.15 we show this ratio for Oxygen (lower plot): its primariness

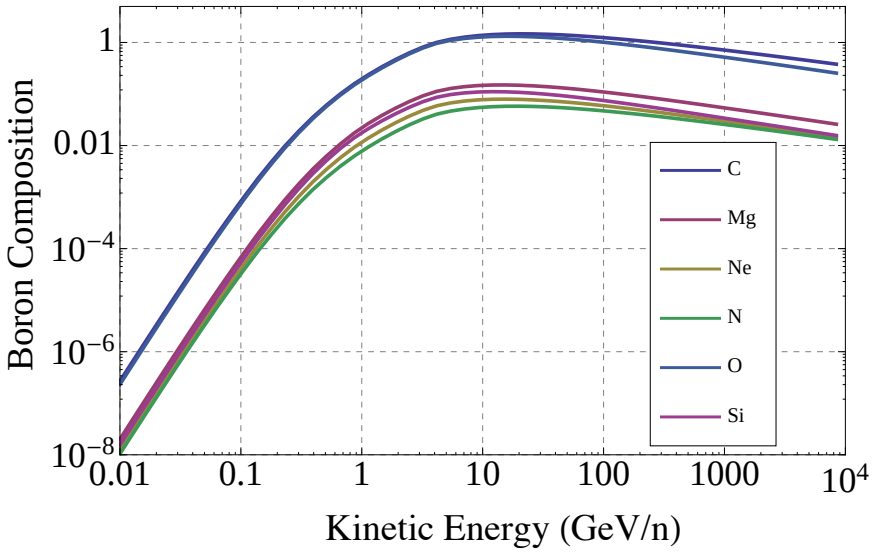

Figure 6.14: Primary nuclei contribution to Boron flux: C (blue curve), O (light blue), Mg (brown), Si (purple), Ne (dark yellow) and N (green line).

varies from 96% to 99% in the 1 GeV-1 TeV range, and for Carbon (upper plot).

As already discussed in Chapter 5, the parameters related to nuclei injection at source are respectively R_0 (that is the reference rigidity associated to the index change), γ_1 i.e. the index below the reference rigidity, and γ_2 that is the index above the reference rigidity. Nevertheless in GALPROP we can't specify the index to use for each nucleus but we have to use the same fixed index for all of them. To bypass this limit, we decided to made single propagations, one for each primary nucleus that has a relevant abundance at source, using for each one its proper index. Using the DCR default set fixed above, we set all the abundances at source equal to zero except for the one of the nucleus of interest; we did the same for charge Z variable, except for the ones from the hydrogen up to the nucleus under investigation. Using the indices shown in Table 6.10 we propagated all the primary nuclei of the reaction network up to the iron.

After obtaining the GALPROP resulting spectra, all the contributions to a single nucleus coming from different primaries were summed up, to obtain the total correct fluxes. In Figure 6.16 some examples of the results obtained for B and B/C are shown. After obtaining all the fluxes with the specific index procedure, we compared them with the ones obtained using a common index, in order to evaluate the degree of variation between the two methods i.e. the error introduced by the unique γ approximation. This result is shown in Figure 6.17: this plots represent specific indeces flux to common indeces flux ratio for Boron (right plot) and Carbon (left plot). In the first case we

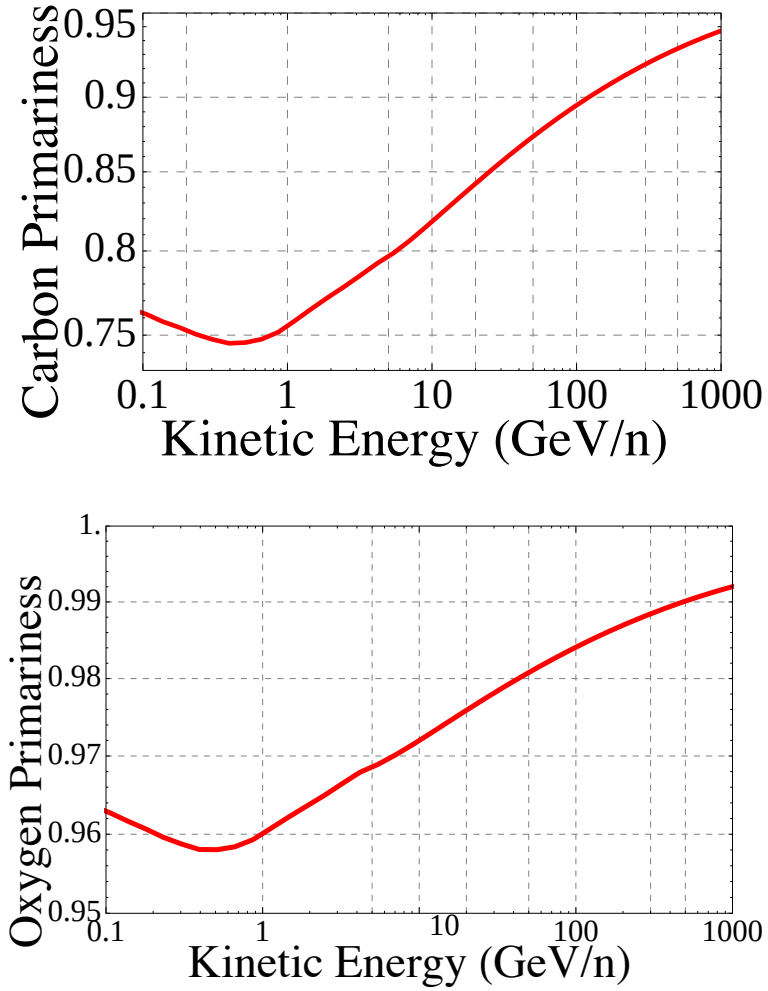

Figure 6.15: Carbon (upper plot) and Oxygen (lower plot) primariness curves, that is the ratio between the nucleus flux at source and the nucleus flux at TOA. We can see that for Carbon it varies from 75% to 95% while for Oxygen it varies from 96% to 99%. From this result we can infer that Oxygen is a completely primary nucleus as it conserves its flux, while the Carbon has a smaller primariness and receives the main contribution to its flux from Oxygen.

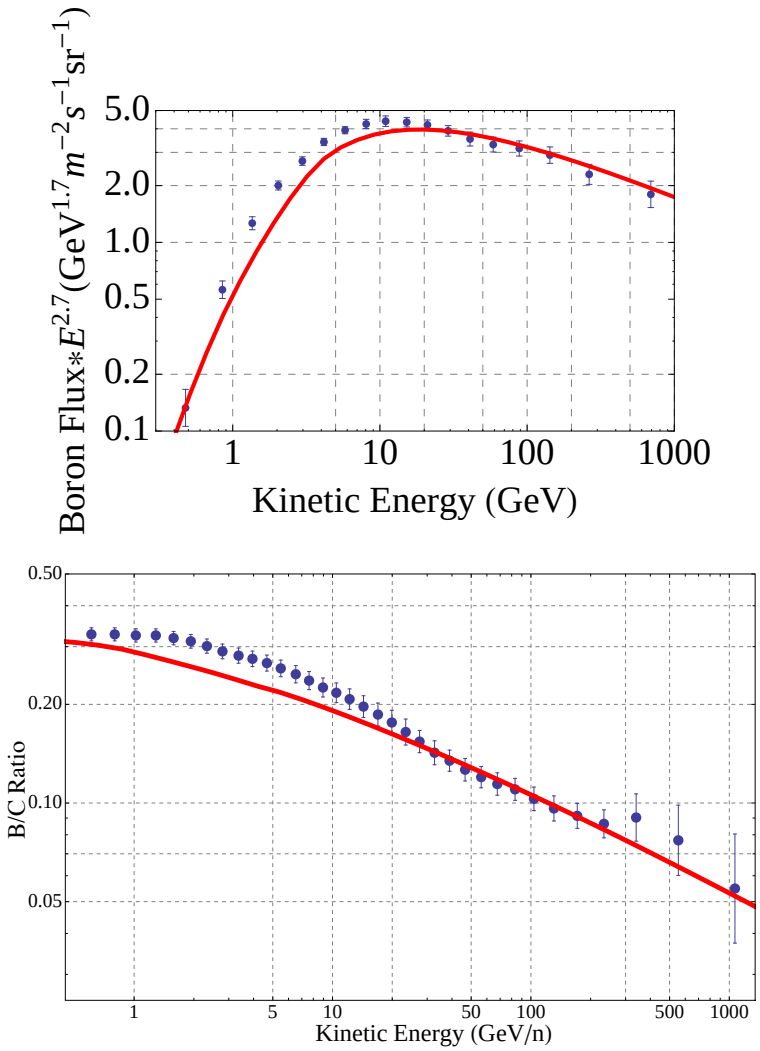

Figure 6.16: Using the specific injection indeces reported in Table 6.10 and the propagation configuration reported in Table 6.8, we obtained the spectra for Boron (upper plot) and the ratio for Boron over Carbon (lower plot).

can observe a really little discrepancy between the two method ($\simeq 10^{-3}$) while in the second case we have a variation of $\simeq 10^{-2}$.

6.2.3 Primary Abundances at Source

In the CR propagation, along with astrophysical uncertainties related to galactic geometry, propagation mechanisms and source distribution, we have to take into account also other kind of uncertainties mainly related to nuclear spallation cross sections, solar modulation and isotopic abundances at source. In the following sections we will explain the study carried out on each one of these uncertainties, showing the importance of the combined effect of all of them on fluxes and ratios.
At first we want to describe the study performed on the last of the above listed uncertainties: the isotopic abundance at source. In GALPROP, for each isotope of each nucleus included in the nuclear reaction chain, we can set a specific abundance at source through the GALPROP file parameter $iso\_abundance\_Z\_A$. Clearly, since we are setting abundance at source, the secondary abundances will be considerd equal to zero.
At the beginning, using the DCR default propagation scheme, we set the abundances according to most recent results avaible [122], to obtain a reference curve for all the fluxes and ratios (He, H/He, B, C, B/C, O, C/O). From the results observed we decided to focus our study on a selection: H,He,C,N,O. For these nuclei we made a scan on a grid, built with a $\Delta = 2\%$, starting from the default value up to a 10% variation. In particular for He,C,N we investigated the behaviour of increasing values from 0% to 10%, while for H and O we considered a gradual decrease ($0 \div 10\%$). All the abundances were modified simultaneously. In Figure 6.18 the result obtained for the Carbon flux is shown, while in Figure 6.19 we show the result for the Boron over Carbon ratio. On the left a set of coloured curves is shown, each one representing a different percentage variation. On the right, instead, a band is shown: the lower curve corresponds to a 2% variation while the upper one corresponds to a 10% variation, so that all the possible variation investigated are considered.

Observing the comparison between preliminary data and the variation band produced, we can say that a good agreement is achieved: this means that non astrophyical uncertainties must be taken into account in the analysis along with astrophysical ones. In Table 6.11 we outline all the abundances adopted to obtain the previous fits. Next to each value we show the limit on the variation considered.

Another way to estimate the uncertainties produced by isotopic abundances on fluxes and ratios is the use of the backtracing procedure. Through this method we can

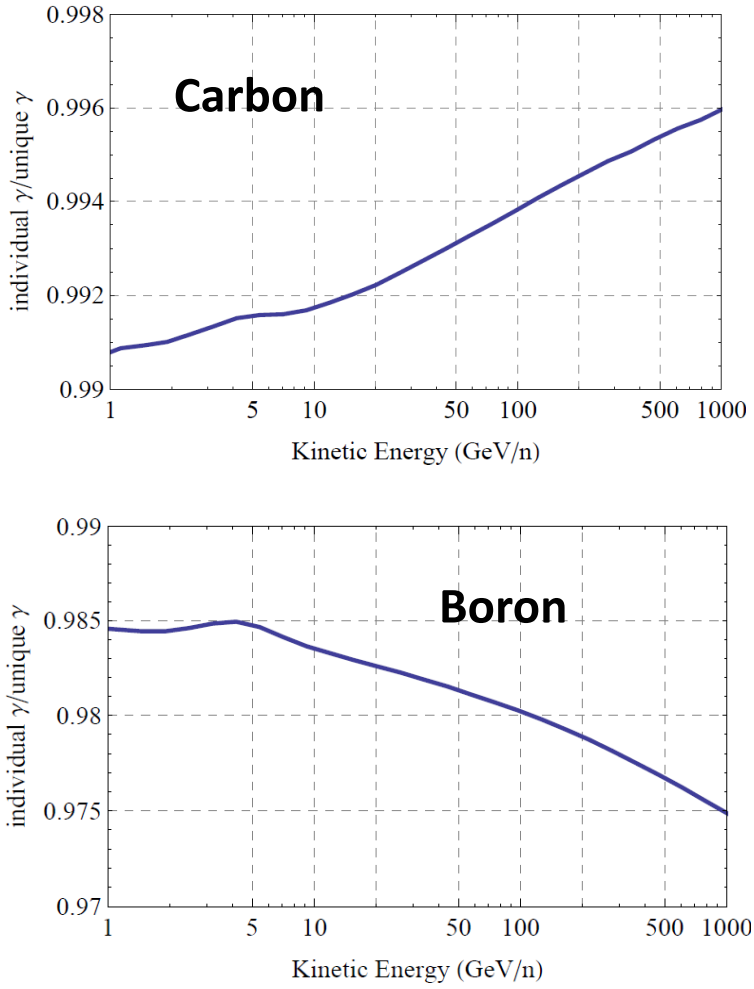

Figure 6.17: These figures represents the comparison between a propagation done with the specific index method and the other done with the common index method for Carbon (upper plot) and Boron (lower plot). We can see that for Carbon the variation between the two methods is $99\% \div 99,6\%$ while for Boron the variation is $97,5\% \div 98,5\%$.

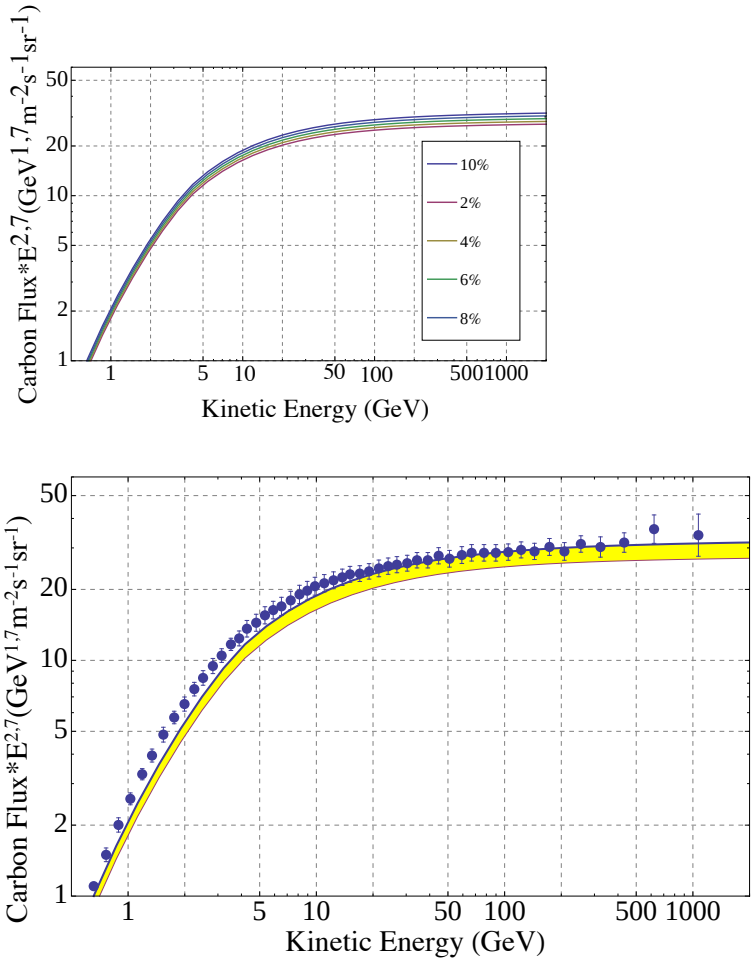

Figure 6.18: Effect of primary abundances at source variation for Carbon flux. The upper plot contains different curves associated to different abundances (from 2% to 10%) fixed in the propagation scheme, while the lower plot shows a the variation band obtained from the lower limit (2%) and the upper limit (10%).

	From	**To**
H	$0{,}954{\cdot}10^6$	$1{,}06{\cdot}10^6$
He	$7{,}199{\cdot}10^4$	$7{,}9189{\cdot}10^4$
C	2819	3100,9
N	182,8	201,08
O	3439,8	3822

Table 6.11: Lower and upper limits considered for the isotopic abundances at source for primary nuclei propagated in GALPROP. For H and O we consider a decreasing variation of Δ=2% while for the others we consider a gradual increasing of Δ=2%.

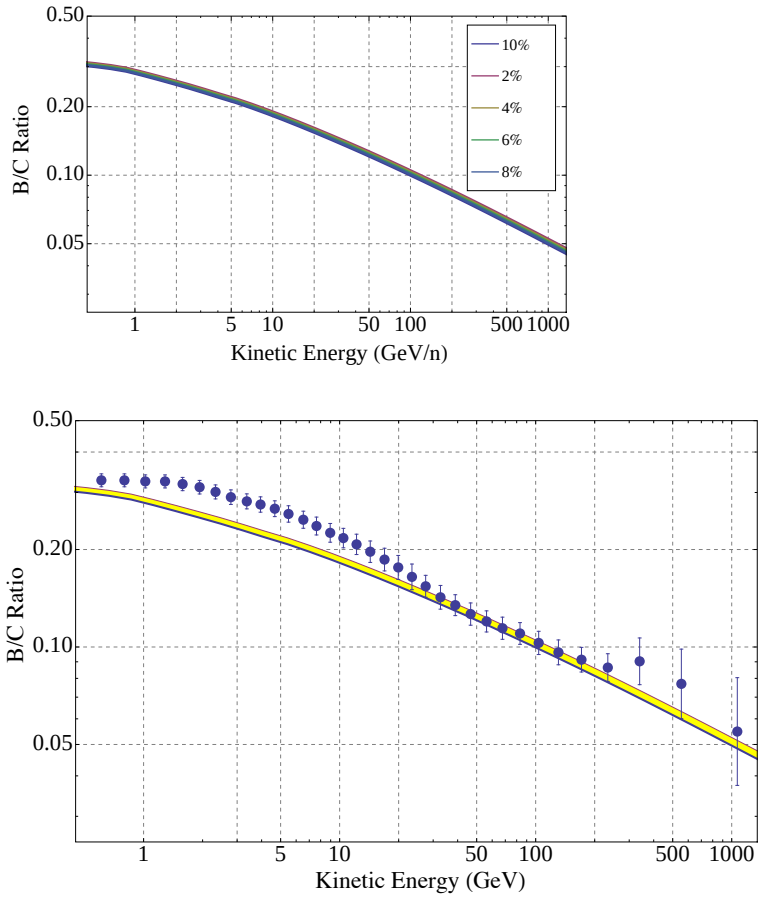

Figure 6.19: Effect of primary abundances at source variation for Boron over Carbon ratio. The upper plot contains different curves associated to different abundances (from 2% to 10%) fixed in the propagation scheme, considering a simultaneous variation of all the selected primary nuclei. The lower plot shows a variation band obtained from the lower limit (2%) and the upper limit (10%).

observe that a $5 \div 10\%$ abundance uncertainty produce a 5% variation on the specific primary nucleus and a few % variation for daughter nuclei. In Figure 6.20 we show the effect of the abundance variation on Boron and Carbon fluxes, considering only the Carbon isotopic abundance variation.

6.2.4 Nuclear Cross Sections

This section is devoted to the study of another source of non astrophysical uncertainties, i.e. the nuclear spallation cross section, that affects fluxes and ratios expecially at low energies.
This uncertainty descends from our poor knowledge about spallation processes that take place during CR propagation through the Galaxy. From the literature we know that the reference uncertainties related to cross sections are of $15 \div 20\%$; they affect in a different way primary and secondary fluxes, along with primary to primary or primary to secondary ratios. For primary fluxes a varition of $15 \div 20\%$ of the cross section produces a variation of $1 \div 2\%$ on the flux. On the other hand for a secondary flux the corresponding variation is $10 \div 12\%$. These values have been obtained with a comparative analyis with GALPROP. In Figure 6.21 we show as example the variation band for H/He rati (upper left plot), B/C ratio (upper right plot), Carbon flux (lower left plot) and on Boron flux (lower right plot), corresponding to a cross section variation of $15 \div 20\%$. The central curve in the band, corresponds to the default fit while the upper and lower curves correspond to the variation of 5% for H/He, 12% for B/C, 5% for Carbon and 12% for Boron respectively.
Another way to investigate the effects of nuclear cross section variation is the tuning of its GALPROP parameter. To be more precise, in GALPROP we have two parameters related to nuclear cross section: $total\_cross\_section$ and $cross\_section\_option$. The first defines the options for determining total fragmentation cross section, while the second includes the options for determining isotopic production cross sections (here experimental data are used whenever available). All the possible values for the above mentioned parameters were investigated combinatorially, to observe the resulting fluxes and ratio produced. In Table 6.12 are sketched the combination used for the different runs.

In Figure 6.22 we show as example the Carbon flux obtained for $total\_cross\_section = 1$ (Wellish and Axen parametrization) and $cross\_section\_option = 012$ (Webber parameterization).
A particular case in the study of non astrophysical uncertainties is represented by the Lithium. Lithium as Boron and Berillium, is a pure secondary CR nucleus, nevertheless

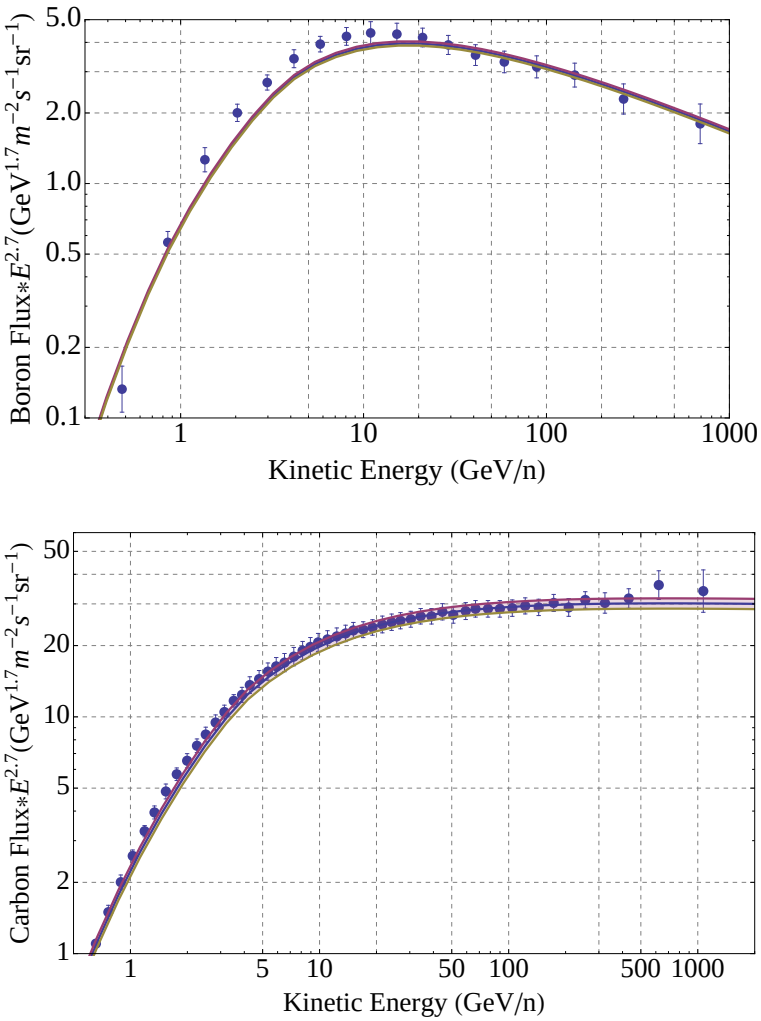

Figure 6.20: Boron (upper plot) and Carbon (lower plot) fluxes obtained from the back-tracing procedure. Using this procedure we can estimate what is the effect of abundances uncertainties at source on the final primary and secondary fluxes. In these plots we show that a abundance uncertainty of $5 \div 10\%$ produce a 5% error on Carbon flux and few % error on Boron one.

total_cross_section	0,1,2
cross_section_option	$000 \div 022, 100 \div 122$

Table 6.12: GALPROP parameters related to nuclear spallation cross section. Here possible values for the two parameters (corresponding to avaible parameterization from literature) are shown.

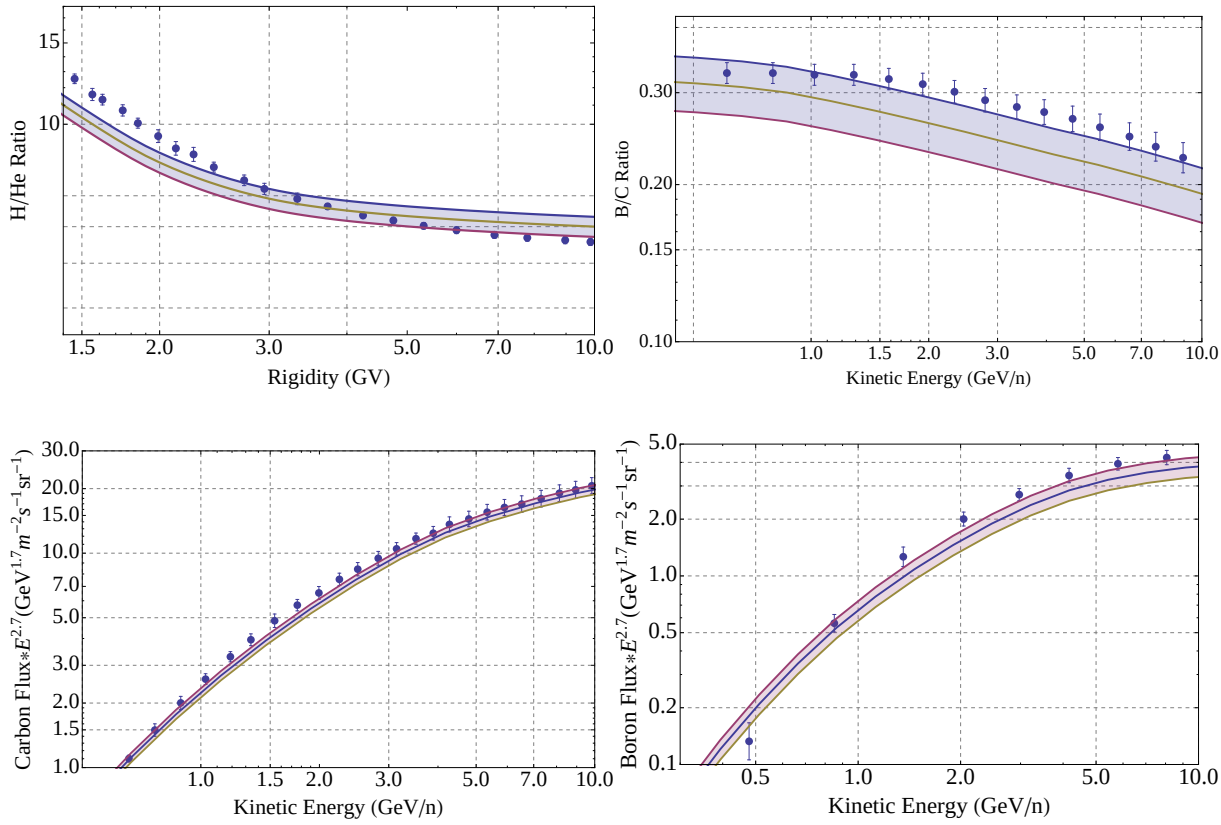

Figure 6.21: H/He ratio (upper left plot), B/C ratio (upper right plot), Carbon flux (lower left plot) and Boron flux (lower right plot) with their cross section uncertainty band. We know from literature that the effect of spallation cross sections uncertainties propagates on final primary and secondary spectra, particularly in the low energy region ($E < 15$ GeV/n). In these plots we show that a cross section uncertainty of $15 \div 20\%$ produce a $1 \div 2\%$ variation on primary fluxes and a 12% variation on secondary ones. Here we consider an uncertainty band of 5% for H/He ratio, 12% for B/C, 2% for C and 12% for B flux. We can observe that applying the uncertainty band, a good agreement with AMS-02 data is achieved, except for the low energy region of the H/He ratio: to this end we must recall what said at the beginning of this chapter i.e. we are using for this ratio the proton measure, that is preliminary and still under investigation by AMS-02 collaboration.

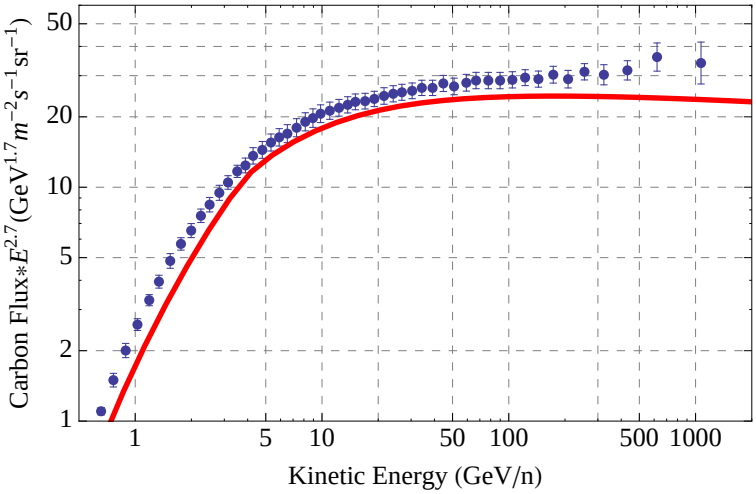

Figure 6.22: Carbon flux obtained modifying the cross section parameters in the propagation scheme, the Wellish-Axen parameterization was used for the total_cross_section while the Webber parameterization was used for the cross_section_option.

our knowledge about its propagation and interaction parameters is extremely poor. For this nucleus both astrophysical and nuclear uncertainties are incredibly high. Indeed, from the experimental observations we can state that this nucleus has a completely anomalous behaviour respect to other CR. In Figure 6.23 preliminary Lithium flux is shown. Both the preliminary data and the fit obtained using the DCR final set are shown. We can see from the plot the complete disagreement between data and fit, as stated above.

6.2.5 Solar Modulation and overall uncertainty

In this section we will discuss about the last of the above mentioned non astrophysical uncertainties: the solar modulation.
As already stated in this work, solar modulation affects cosmic rays near the top of the atmosphere, just before they are revealed by the detector. The uncertainty related to this effect is due to our not exact knowledge of the solar modulation parameterization. Usually we adopt a simplified hypotesis called the force field approximation; using this approximation we can write the energy shift produced by this effect as

$$\frac{E^{TOA}}{A} = \frac{E^{IS}}{A} - \frac{|Z|\,\Phi}{A}$$

where Φ is the solar modulation parameter while IS and TOA stand for interstellar medium and top of the atmosphere respectively. As already discussed the solar modu-

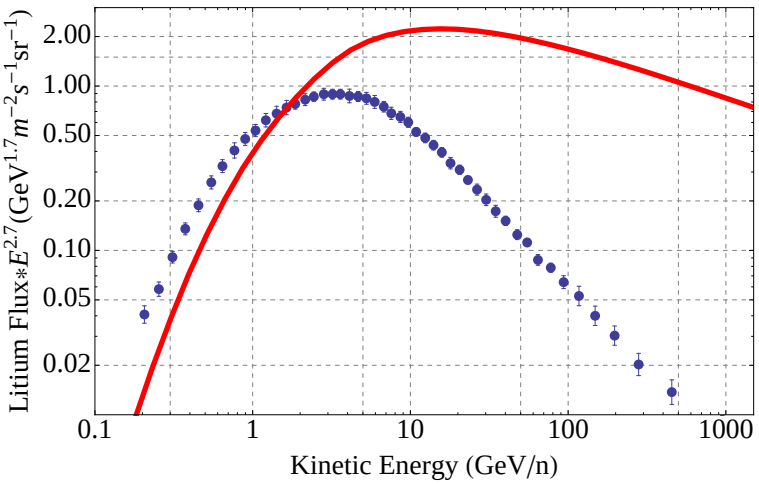

Figure 6.23: Lithium flux, obtained with the DCR final set (see Table 6.8). We can see a complete disagreement w.r.t. AMS-02 data. Astrophysical and nuclear uncertainties are incredibly high for this nucleus and experimental results suggest a completely anomalous behaviour for it.

lation can be introduced in GALPROP with a distinct procedure after the run of the propagation file, in order to obtain the final spectra.
In this study, according with what was done for the isotopic abundance, we made a scan of a solar modulation grid, implemented with Δ= 10 MV steps, exploring the range $\Phi = 500 \div 600$ MV. From literature we know that the uncertainty related to this parameter is about $10 \div 15\%$ and that it affects mainly the low energy region of fluxes and ratios.

In Figure 6.24 is shown the modulation for Boron and Carbon fluxes in the low energy range: the band ends correspond, respectively, to 10% and 15% variations. In Figure 6.25 instead we can observe the results obtained for Oxygen flux and Boron over Carbon ratio.

Finally we decided to study the effect of the three uncertainties, presented above, combined together. The contribution from isotopic abundances is about 5% for primary nuclei and $1 \div 2\%$ for secondary ones, for solar modulation we have to consider a 5% for the low energy region and for nuclear cross section the uncertainty contribution to primary is about 2% while for secondary is 12%. An example of the resulting effect is shown in Figure 6.26 for Boron and Carbon fluxes and for Boron over Carbon ratio.

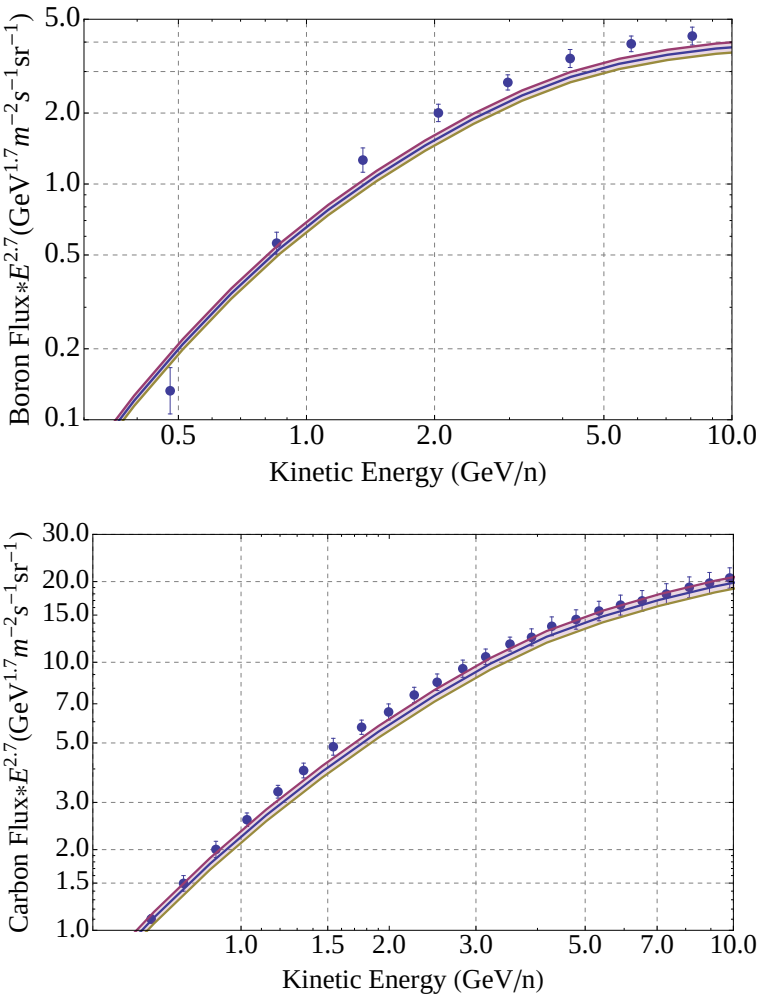

Figure 6.24: Boron (upper plot) and Carbon (lower plot) fluxes with a variation band of 5%. We know from literature that the uncertainty that affects the solar modulation propagates on primary and secondary fluxes, so that a $10\% \div 15\%$ uncertainty on the solar modulation produce a 5% variation on final spectra.

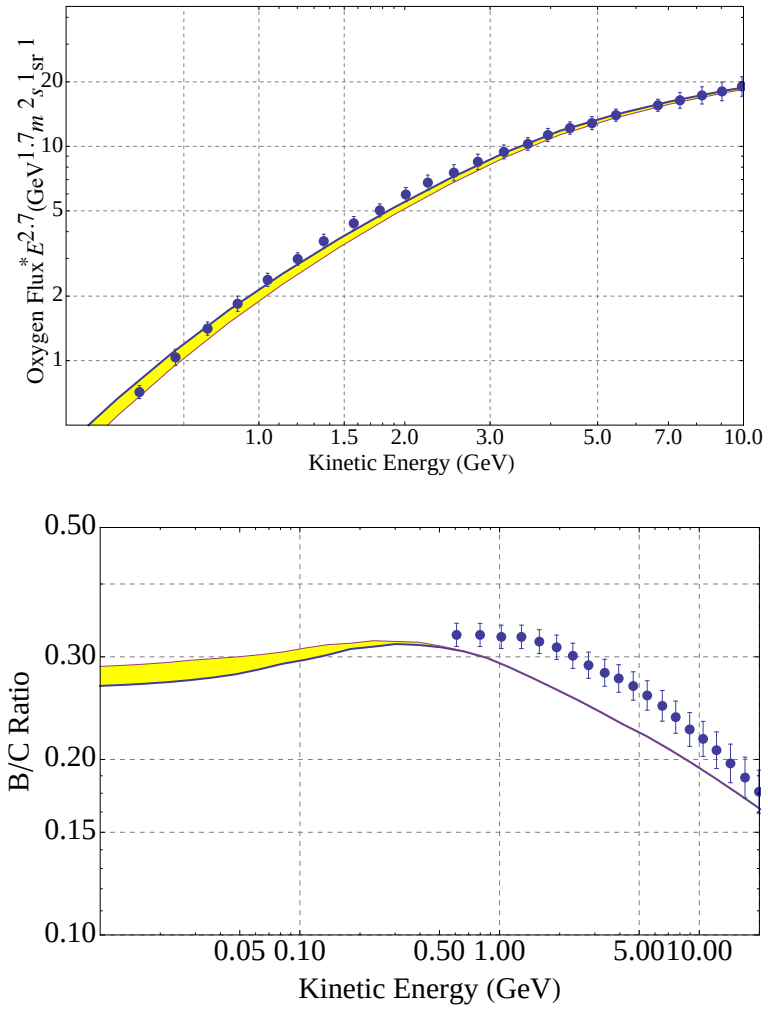

Figure 6.25: Solar modulation uncertainty band for Oxygen flux (upper plot) and B/C ratio (lower plot), obtained from a scan of the solar modulation parameter from 550 up to 600 MV, using 10 MV steps.

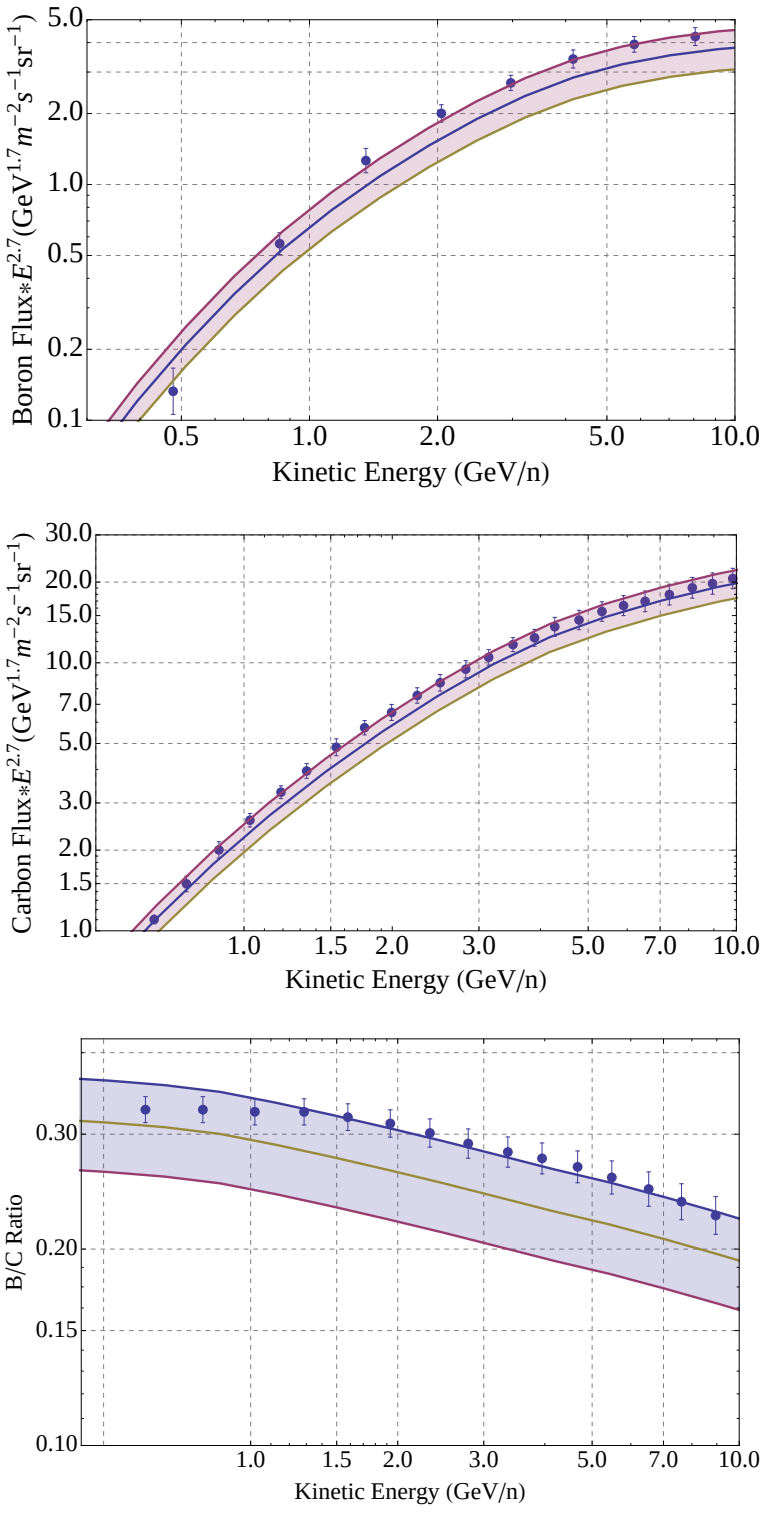

Figure 6.26: Boron (upper plot) and Carbon (middle plot) fluxes and B/C ratio (lower plot) with a total uncertainty band produced summing up all the non astrophysical uncertainties: the one associated to isotopic abundances at source (2% for B and 5% for C), the solar modulation one (5% for both B and C) and the one related to spallation cross section (12% for B and 2% for C). For the B/C ratio in particular we considered a total uncertainty of 16% due to the three mentioned contributions.

nucleus	spectra.txt
Hydrogen (1,2)	01,02
Helium (3,4)	03,04
Lithium (6,7)	19,05
Boron (10,11)	21,07
Carbon (12,13)	08,22
Nitrogen (14)	09
Oxygen (16,18)	10,20

Table 6.13: Nuclei analyzed and their corresponding GALPROP text output. We obtain a different text file for each isotope. To obtain the Carbon total flux for example we sum up the contributions fromC^{12} (text output 08) and C^{13} (text output 22).

6.3 Galprop Results

All the GALPROP simulations were execute using a remote access and subduing parallel jobs to Ravenna pc farm. Computational time needed for a single simulation is about few minutes, for this reason to optimize the procedure we decided to subdue job's tail of almost ten simulation each. Standard output files in GALPROP are read using a dedicated set of routines, this way we obtain as final output text file, more easy to handle with the analysis software we chose. The analysis was done using a second software namely Mathematica. Mathematica is a computational software program based on symbolic mathematics that supplies also a programming language supporting procedural, functional and object oriented constructs (the version used was the eighth). The analysis procedure was achieved using Mathematica notebook. At first we imported all the available AMS data files and put them in a bidimensional array, to make at a later stage a comparison with the GALPROP outputs. Then in the same workspace the GALPROP output files were imported and put in a multidimensional array, separating the energy values from the flux and ratio values. These spectra, which are in MeV and $MeVm^{-2}s^{-1}sr^{-1}$, were then corrected using a 10^{-3} factor for the energies and a $10^{-1,1}$ for the fluxes, to obtain as measurement unit GeV and $GeV^{1,7}m^{-2}s^{-1}sr^{-1}$ respectively. As already stated there was a correspondence between each isotope and its output spectra as outlined in Table 6.13. Using the above table we summed up the contributions coming from different isotopes to obtain the total nucleus flux.

This way we obtained for each nucleus a bidimensional array containing energies and spectra. Then we made a plot putting AMS data and GALPROP fit together, to observe a direct comparison. In Figure 6.27 Helium and Boron fluxes are shown.
In a similar way we obtained the ratios, at first summing up the different contribution from each isotope, then dividing one flux for the other to obtain the final ratio. In Figure 6.28 we can observe the Hydrogen over Helium and the Boron over Carbon ratios. For the Hydrogen and Helium spectra, together with the energy correction, we used the rigidity conversion to make the comparison with AMS data easier, the following relation was used:

$$R = \frac{\sqrt{A \cdot K_n(A \cdot K_n + 2 \cdot M_{nucleus})}}{Z} \tag{6.6}$$

We can observe from the plots that there is a good correspondence between data and the simulation obtained using GALPROP, but it is important to estimate this agreement, this will be done in the next section (using a statistical procedure), where we will discuss the chi-square test.

6.3.1 Chi-Squared Test

As stated above, in this section we want to explain the procedure used to estimate the degree of agremeent between data and GALPROP simulation produced. The method used to this aim is the chi-squared test.
One of the central issue in the analysis procedure of experimental results is the agreement test, between data and simulation. Each time we conduct an analysis we will find some disagreement between data and simulation: what is important is the understanding of this disagreement. In fact, it can originates from a too little statistics or it can derives from a wrong simulation. What we have to do then is to carry out an hypotesis test, fixing a significance level that will discriminate between the correctness or the wrongness of a certain hypotesis. This test won't provide any definite answer, it will just give us the result reliability in the sense of probability.
To test the agreement between a data set and a simulation we have to use an hypotesis test, one of the most used is the Chi−Squared Test. In general we can write the chi−squared as

$$\chi^2 = \sum_{k=1}^{N} \frac{|O_k - E_k|^2}{\sigma^2} \tag{6.7}$$

here O_k are the observed values, E_k are the simulated values and σ is the error asociated to the measured values. So this definition provides a way to test the agreement: if χ^2

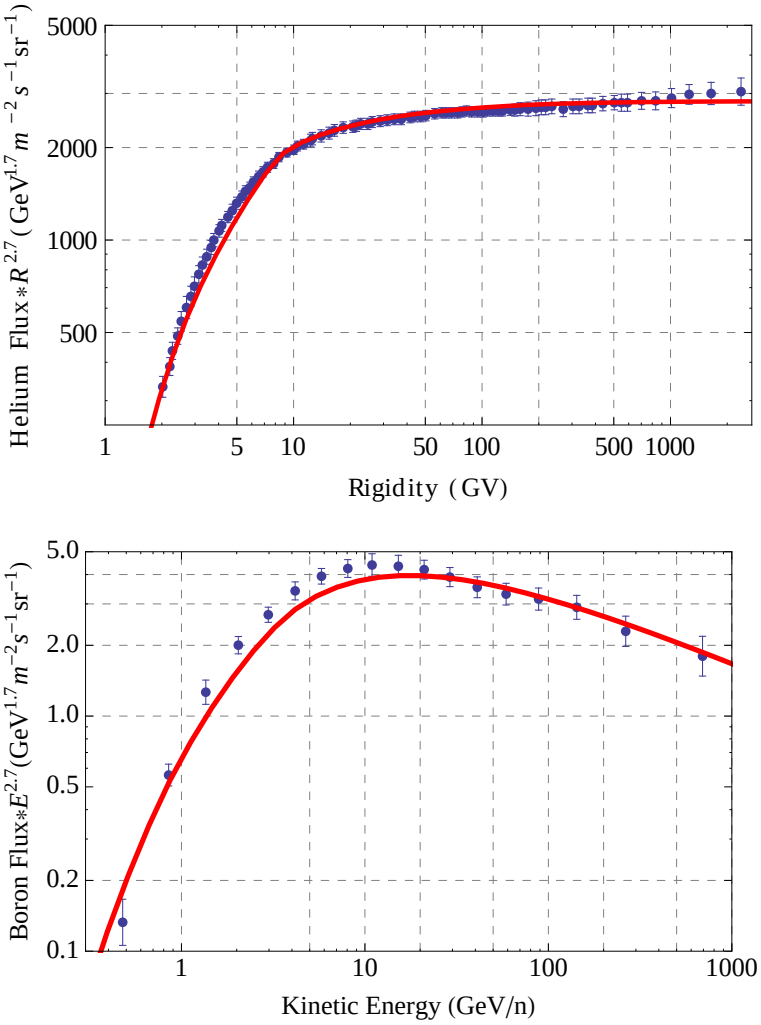

Figure 6.27: Helium (upper plot) and Boron (lower plot) fluxes obtained with the DCR best set (see Table 6.8) tuned from the DCR default set (see Table 6.7). All the spectra produced via GALPROP simulation (red curves) were analyzed and plotted using the software Mathematica to make a comparison with preliminary AMS-02 (blue dots).

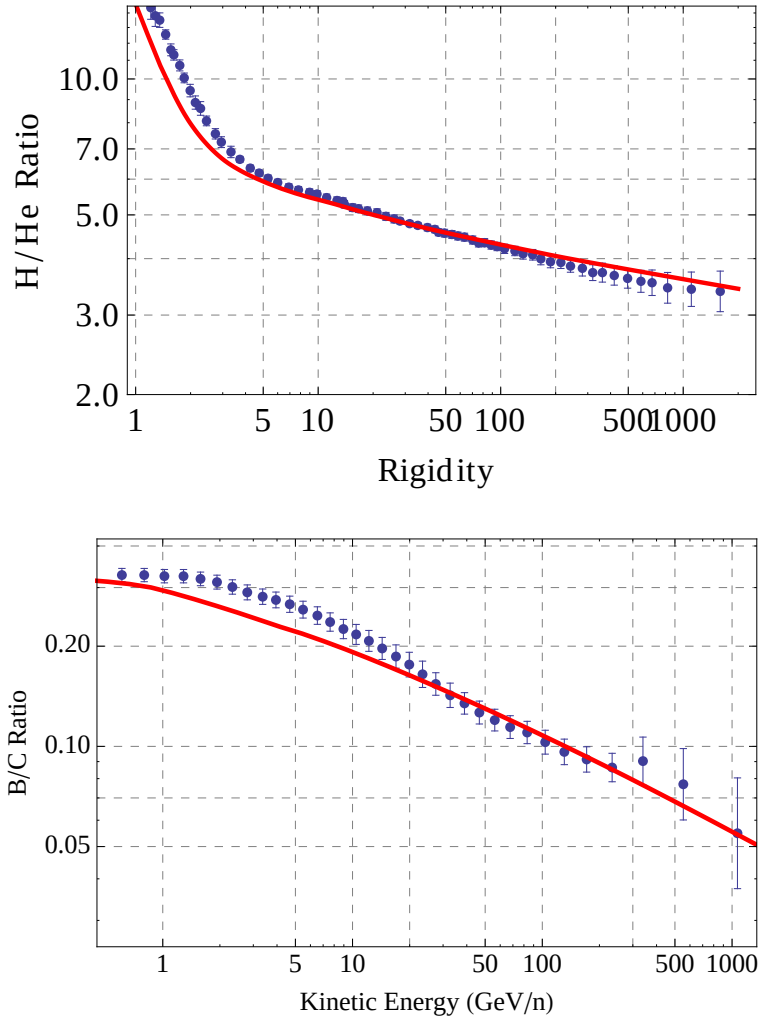

Figure 6.28: Hydrogen over Helium (upper plot) and Boron over Carbon (lower plot) ratios obtained with the DCR best set (Table 6.8). The ratios produced via GALPROP simulation were analyzed and plotted using Mathematica for a comparison with AMS-02 data. In this figure as in the previous one (Fig.6.27) H and He fluxes and their ratio are expressed in Rigidity (see Eq.6.6), according to what found in literature.

is near N then we can say there is a good agreement, if χ^2 is higher then N there isn't agreement. Beside this definition a more common one is used, that is

$$\tilde{\chi^2} = \frac{\chi^2}{d} \tag{6.8}$$

This is called reduced chi-squared and d stands for the degree of freedom that can be defined as the number of data available minus the number of constraints calculated from the data. In this case there is good agreement for a $\tilde{\chi^2} \simeq 1$. Along with these definition, what we need is a quantitative measurement of the agreement. Moreover we need to fix a value to separate the agreement region from the disagreement one. This is achieved studying the χ^2 as a random variable; for this variable we can study a probability distribution that can be written as

$$f_N(\chi) = \frac{1}{2^{N/2}\Gamma(N/2)}\chi^{N/2-1}e^{-\chi/2} \tag{6.9}$$

Where N are the degrees of freedom and the function exists only for positive χ^2. This way we obtain a chi-probability that can be written as

$$P(\tilde{\chi^2} \geq \tilde{\chi^2_O}) = ...\% \tag{6.10}$$

where the Significance Level (S.L.) is fixed so that, if our chi-probability is higher then the S.L., we can state we have a good agreement, otherwise we don't. The S.L. is dependent on the analysis done and must always be declared.
What we did in our analysis, was to evaluate the chi-squared for all the available points using the relation

$$\chi^2 = \frac{\left|\Phi_{GALPROP} - \Phi_{AMS-02\_DATA}\right|^2}{\sigma^2} \tag{6.11}$$

Then we summed up every point contribution to obtain the total chi-squared value

$$\chi^2_{TOT} = \sum^{Numberofpoints} \chi^2 \tag{6.12}$$

Using the above defined $f_N(\chi)$ we evaluated the chi-squared distribution, using for N the number of available points. Finally we evaluated the cumulative density function for $f_N(\chi)$ or p-value

$$P(\chi^2 \leq \chi^2_O) = CDF(f_N(\chi)) \tag{6.13}$$

to obtain in the end

$$P(\chi^2 \geq \chi^2_O) = 1 - P(\chi^2 \leq \chi^2_O) \tag{6.14}$$

that is the chi-squared probability.
This procedure was repeated for all the nuclei and ratios available that is: $\bar{p}/p$, He,

nuclei	chi-probaility
$\bar{p}/p$	0,99
He	0,99
H/He	0,99
B	0,96
C	0,96
B/C	0,95
O	0,98
C/O	0,99

Table 6.14: P-value obtained using the Chi-Square test for the comparison between AMS-02 preliminary data and GALPROP results for $\bar{p}$/p,He,H/He,B,C,B/C,O,C/O. Our significance level was set at 95%.

H/He, B,C, B/C, O, C/O, thus obtaining for each one a specific chi-probability. Our significance level is set at 95%. According to the multi-fit method adopted in this work we also evaluate the total chi-probability, by summing up all the chi-probability contributions from different fluxes and ratios and then divided for the number of contributions considered.
In Table 6.14 all the chi-probability calculated for the high energy region (E>10 GeV) are listed.

The total chi-probability obtained with the multi-fit is 0.6013, for a S.L. fixed at 95%. A complete description of the results obtained at the end of this analysis is reported in Fig. 6.29 where all the simulation obtained with the final DCR set (see Table 6.15) are shown for a comparison with the preliminary AMS-02 data declared at the beginning of this chapter.

6.4 Dark Matter Physics with GALPROP and PPPC4DMID

In this last section we want to describe the use of the best set found in the previous analysis to compute some DM signals, referring to its indirect research in the $\bar{p}/p$ and $\bar{p}$ flux production. As already discussed before, for DM candidates we can write the following decay or annihilation reaction

$$\chi\chi \longrightarrow q, l, W, Z, g, \gamma \longrightarrow \gamma, p, \bar{p}, e^+, e^-, \nu, D, \bar{D} \tag{6.15}$$

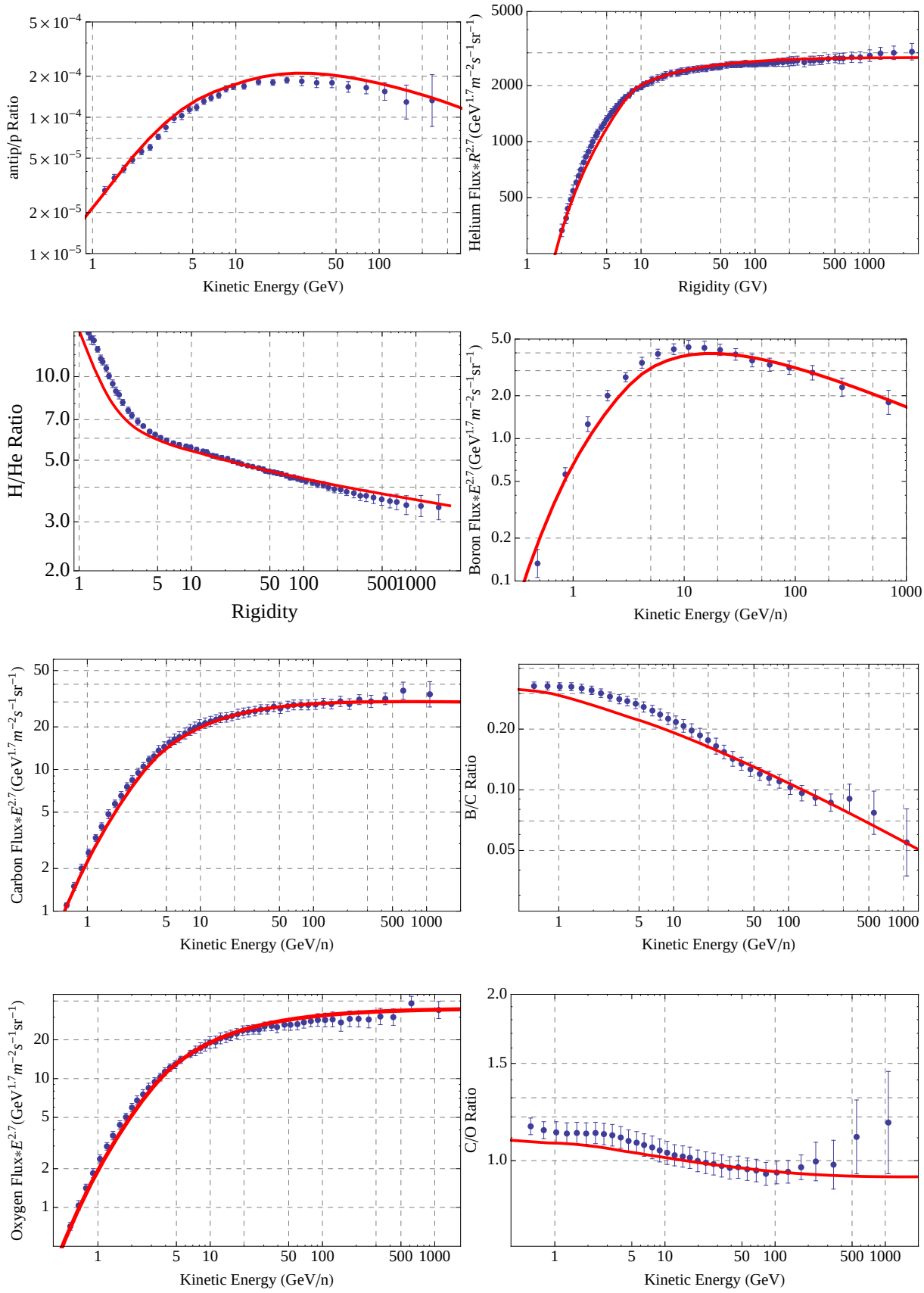

Figure 6.29: Final comparison between AMS-02 data and spectra produced in GALPROP using the DCR final set.

	DCR FINAL SET
z[kpc]	$4,06^{+0,4}_{-0,8}$
$r_{max}[kpc]$	20^{+20}_{-0}
$D_0(x)[cm^{-2}s^{-1}]$	$4,1^{+0,2}_{-0,4}$
$D_0(z)[cm^{-2}s^{-1}]$	$4,1^{+0,2}_{-0,4}$
δ	$0,34^{+0,3}_{-0,2}$
$V_A[kms^{-1}]$	16^{+14}_{-6}
$v0\_conv[kms^{-1}]$	12^{+1}_{-2}
$dV_C/dz[kms^{-1}kpc^{-1}]$	$10^{+0,0}_{-2,5}$
$z0\_conv[kpc]$	$4,0^{+0,0}_{-0,2}$
R_0[GeV/n]	10^{+1}_{-1}
z_0[kpc]	$0,2^{+0,2}_{-0,0}$
α	$1,5^{+0,1}_{-0,5}$
β	3^{+0}_{-1}
r_0[kpc]	20^{+0}_{-5}

Table 6.15: Final DCR configuration. Here we report the main propagation parameters with their values and the associated error.

parameter	values
Halo	NFW, Iso,Evans, alternative
Mass[GeV]	300,500,700,1000,1500
Set	MIN,MED,MAX
$\sigma[cm^3s^{-1}]$	$10^{-23}, 10^{-24}, 10^{-25}, 10^{-26}$

Table 6.16: In table are reported the four parameters tuned along with their different values: the parameterization for the DM halo, the DM mass, the propagation scheme adopted and the thermal cross secion. All the values reported were combinatorially tested and compared with data.

Halo	NFW
Mass	1500 GeV
Set	MED
σ	$10^{-23}cm^3s^{-1}$

Table 6.17: DM GALPROP parameters values used in the best fit propagation scheme (DCR best fit). These parameters were fixed with the values reported in table during the DCR propagation scheme fine tuning.

So what we will analyze in order to observe some indirect production are final states fluxes written above.

In Chapter 3 we said that GALPROP provides different parameter associated to dark matter: tuning these parameters we can simulate some DM production in the Galaxy and studying the final fluxes produced we can observe some indirect hints. In this work we concentrate our attention on four parameters tuning them according to different values (see Table 6.16): here MIN, MED, MAX stand for the previous defined default sets (see Table 6.2) while the first line of the table contains some possible halo models (we will return on them later), the second line contains possible DM masses and in the last line possible DM annihilation cross section are written. For the GALPROP DM simultaion we tuned only these parameters, all the remaining ones were fixed according to what found in the previous work, i.e. the DCR best fit set. Indeed in the first phase of our analysis we concentrated our study on parameters that were mainly related to geometry and propagation mechanisms. We didn't tune DM parameters and their values were fixed according to what reported in Table 6.17

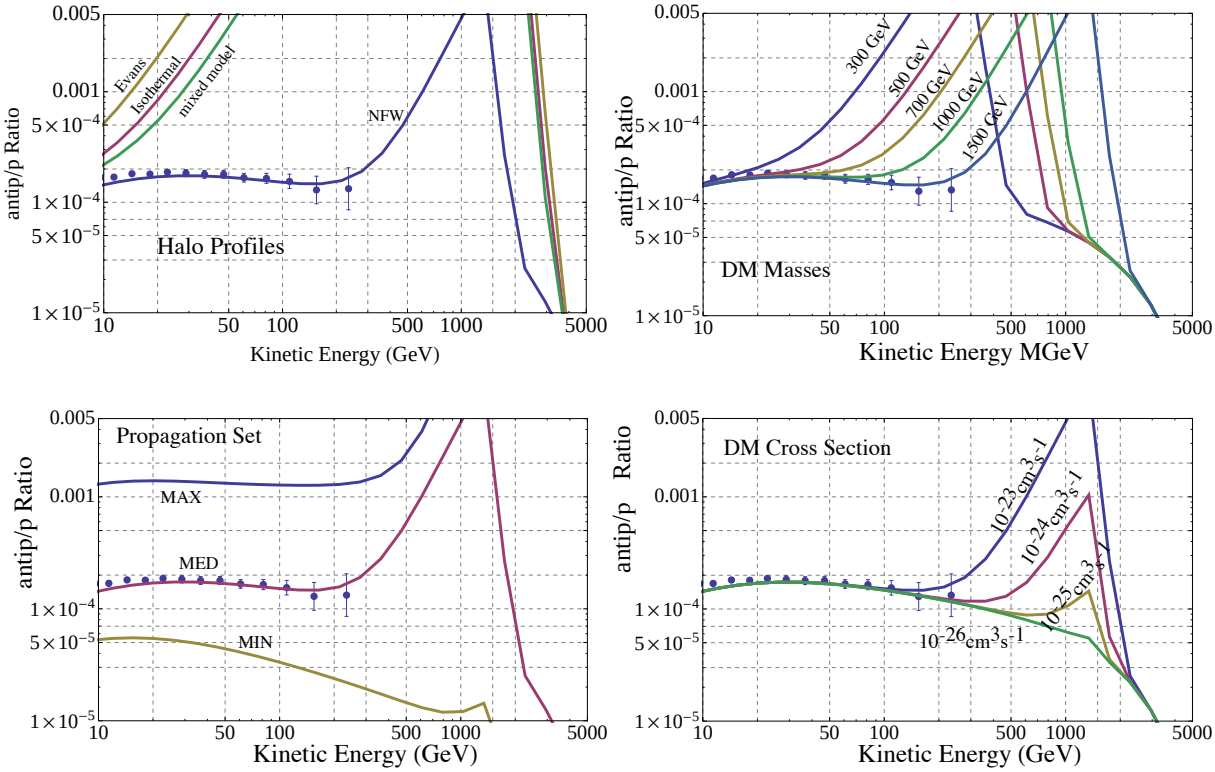

Figure 6.30: Comparison between different values for the tunable parameters associated to DM production in GALPROP: DM halo profile (upper left), DM mass (upper right), propagation set (lower left) and DM annihilation cross section (lower right). The fixed set used a NFW halo profile, a 1500 GeV mass, a $10^{-23} cm^3 s^{-1}$ crosse section and a MED propagation set.

where the halo profile, according to the Navrro-Frank-White, can be written as

$$\rho_{NFW}(r) = \rho_s \frac{r_s}{r}(1 + \frac{r}{r_s})^{-2} \tag{6.16}$$

So, starting from this set, we combinatorially varied the previous mentioned parameters. Some explicative results are shown in Figure 6.30.

In the first line (upper left plot) the comparison between four possible halo models is shown: the blue line refers to the Navarro-Frank-White (NFW) configuration, the purple line to the Isothermal, the yellow one to the Evans and the green one to an alternative mixed model. We can observe that the most suitable configuration is the one obtained with the NFW model. The upper right plot instead represents the comparison between different DM masses: the blue curve corresponds to a 300 GeV mass, the purple one to 500 GeV, the yellow one to 700 GeV, the green one to 1000 GeVand finally the light blue one to the heaviest mass of 1500 GeV. In the lower left plot we show the comparison between the MIN (yellow), the MED (purple) and the MAX

(blue) propagation sets; the MED set shows the best agreement. Finally the lower right plot shows the annihilation cross section variation from 10^{-26} to 10^{-23} $cm^3 s^{-1}$: for all the values considered we obtain a good agreement with preliminary data.
In this study, along with GALPROP, we used another simulation software that is Poor Particle Physicist Cookbook for Dark Matter Indirect Detection (PPPC 4 DM ID)[142]. This software provides ingredients and recipes for computing signals of Dark Matter annihilation and decays in the Galaxy and beyond. For each DM channel the energy spectra of $e^{\pm}, \bar{p}, \bar{d}, \gamma, \nu$ at production can be generated and computed with high statistic simulations. Propagation functions for charged particles in the Galaxy for several DM distributions profiles and sets of propagation are also available. Using these propagation functions, we can obtain the energy spectra for $e^{\pm}, \bar{p}$ and $\bar{d}$ at the Earth position. All the results obtained this way are available in numerical form and can be directly used for the analysis. We will describe more in detail this software properties and structure in the following.

6.4.1 The PPPC4DMID Software

Cosmology and astrophysics provide several convincing evidences of the existence of Dark Matter [143,144,145]. The observation that some mass is missing to explain the internal dynamics of galaxy clusters and the rotations of galaxies dates back respectively to the '30s and the '70s [146]. The observations from weak lensing [147], for instance in the spectacular case of the so-called 'bullet cluster' [148], provide evidence that there is mass where nothing is optically seen. More generally, global fits to a number of cosmological datasets (Cosmic Microwave Background, Large Scale Structure and also Type Ia Supernovae) allow to determine very precisely the amount of DM in the global energy-matter content of the Universe at $\Omega_{DM}h^2 = 0.1199 \pm 0.0027$ [181]. All these signals pertain to the gravitational effects of Dark Matter at the cosmological and extragalactical scale. Searches for explicit manifestation of the DM particles that are supposed to constitute the halo of our own galaxy (and the large scale structures beyond it) have instead so far been giving negative results, but this might be on the point of changing.
Indirect searches for Dark Matter aim at detecting the signatures of the annihilations or decays of DM particles in the fluxes of cosmic rays, intended in a broad sense: charged particles (electrons and positrons, protons and antiprotons, deuterium and antideuterium), photons (gamma rays, Xrays, synchrotron radiation), neutrinos. Pioneering works have explored this as a promising avenue of discovery since the late

70's: gamma rays from annihilations were first considered in [150,151,152] and then revisited in [153], antiprotons in [154,155] and then more systematically in [155,156], positrons in [157], antideuterons have been first discussed in [158,159,160], radio-waves from synchrotron radiation from DM in [161,162,163] and later in [164], extragalactic gamma rays have been first discussed in [166]. Inverse Compton gamma rays from DM have been only relatively recently considered as a possible signal. In general, a key point of all these searches is to look for channels and ranges of energy where it is possible to beat the background from ordinary astrophysical processes. This is for instance the basic reason why searches for charged particles focus on fluxes of antiparticles (positrons, antiprotons, antideuterons), much less abundant in the Universe than the corresponding particles.

A well spread theoretical prejudice wants the DM particles to be thermal relics from the Early Universe. They were as abundant as photons in the beginning, being freely created and destroyed in pairs when the temperature of the hot plasma was larger then their mass. Their relative number density started then being suppressed as annihilations proceeded but the temperature dropped below their mass, due to the cooling of the Universe. Finally the annihilation processes also froze out as the Universe expanded further. The remaining, diluted abundance of stable particles constitutes the DM today. As it turns out, particles with weak scale mass ($\simeq$ 100 GeV $\div$ 1 TeV) and weak interactions could play the above story remarkably well, and their final abundance would automatically be the observed Ω_{DM}. While this is not of course the only possibility, the mechanism is appealing enough that a several GeV to some TeV scale DM particle with weak interactions (WIMP) is often considered as the most likely DM candidate.

In any case, this mass range (TeVish DM) has the best chances of being thoroughly explored in the near future by charged particle and photon observatories, also in combination with direct DM searches (aiming at detecting the nuclear recoil produced by a passing DM particle in ultralow background underground detectors) and, possibily, production at LHC collider. It is therefore the focus of our attention.

Supposing therefore that anomalous features are detected in the fluxes of cosmic rays, it will be crucial to be able to 'reverse engineer' them to determine which Dark Matter is at their origin. Moreover, it will be useful to be able to quickly compute which other associated signals are implied by a possible positive detection and have to be looked for in other channels. Only via a cross correlation of multi messenger signals a putative detection of DM will be confirmed or disproved. More generally, in order to compute the predicted signatures of a given model of Dark Matter, a number of particle physics

and astrophysics ingredients are needed. These ingredients are what PPC4DMID aims to provide.

For the galactic distribution of Dark Matter in the Milky Way several possibilities are considered. The Navarro, Frenk and White (NFW) profile (peaked as r^{-1} at the Galactic Center (GC)) is a traditional benchmark choice motivated by N-body simulations. The Einasto [167,168] profile is emerging as a better fit to more recent numerical simulations; the shape parameter α varies from simulation to simulation, but 0.17 seem to emerge as a central, fiducial value, that is adopted. Cored profiles, such as the truncated Isothermal profile or the Burkert profile, might be instead more motivated by the observations of galactic rotation curves, but seem to run into conflict with the results of numerical simulations. On the other hand, profiles steeper than NFW had been previously studied by Moore and collaborators [169].

As long as a convergent determination of the actual DM profile is not reached, it is useful to have at disposal the whole range of these possible choices when computing Dark Matter signals in the Milky Way. The functional forms of these profiles can be written as:

$$\rho_{NFW}(r) = \rho_s \frac{r_s}{r}(1 + \frac{r}{r_s})^{-2} \tag{6.17}$$

$$\rho_{Ein}(r) = \rho_S e^{-frac2\alpha[(\frac{r}{r_s})^{\alpha}-1]} \tag{6.18}$$

$$\rho_{Iso}(r) = \frac{\rho_s}{1 + (r/r_s)^2} \tag{6.19}$$

$$\rho_{Bur}(r) = \frac{\rho_s}{(1 + r/r_s)(1 + (r/r_s)^2)} \tag{6.20}$$

$$\rho_{Moo}(r) = \rho_s (\frac{r_s}{r})^{1,16}(1 + \frac{r}{r_s})^{-1,84} \tag{6.21}$$

Numerical DM simulations that try to include the effects of the existence of baryons have consistently found modified profiles that are steeper in the center with respect to the DM only simulations. Most recently, was found such a trend resimulating the haloes of [167,168]: steeper Einasto profiles (smaller α) are obtained when baryons are added. To account for this possibility in the software a modified Einasto profile is included (it is denoted as EinastoB, EiB in short in the following) with an α parameter of 0.11. All profiles assume spherical symmetry and r is the coordinate centered in the Galactic Center.

Next, the parameters r_s (a typical scale radius) and ρ_s (a typical scale density) that enter in each of these forms must be determined. Instead of taking them from the individual simulations, they can be fixed by imposing that the resulting profiles satisfy the findings of astrophysical observations of the Milky Way. Namely, it is required:

- The density of Dark Matter at the location of the Sun $r_{\odot} = 8.33$ kpc was determined to be $\rho_{\odot} = 0.3\ GeV/cm^3$. This is the canonical value routinely adopted in the literature, with a typical associated error bar of $\pm$ 0.1 GeV/cm^3 and a possible spread up to 0.2 $\longrightarrow$ 0.8 GeV/cm^3. Recent computations have found a higher central value and possibly a smaller associated error, still subject to debate.

- The total Dark Matter mass contained in 60 kpc (i.e. a bit larger than the distance to the Large Magellanic Cloud, 50 kpc) to be $M_{60} \equiv 4.7 \cdot 10^{11}\ M_{\odot}$. This number is based on the recent kinematical surveys of stars in SDSS. Here the upper edge of their 95% C.L. interval is adopted, to conservatively take into account that previous studies had found somewhat larger values.

The parameters and the profiles adopted in PPC4DMID do not differ much (at most 20%) from the parameter often conventionally adopted in the literature, so that the results obtained can be quite safely adopted for many cases.
As well known, the profiles differ most in the inner part of the galactic halo, close to the galactic center, while they are quite self-similar above a few Kpc, and in particular around the location of the Earth. As a consequence, DM signals from the inner Galaxy (e.g. gamma ray fluxes from regions a few degrees around the GC) will be more sensitive to the choice of profile than DM signals that probe the local environment (e.g. the fluxes of high energy positrons, produced at most a few kpc away from the Earth) or that probe regions distant from the GC (e.g. gamma rays from high latitudes).

We have to notice that in the software the potential contribution from galactic DM substructures are not considered. It is well known that the Cold DM paradigm predicts DM halos to contain in a hierarchical fashion a copious number of subhalos, something which is clearly demonstrated by high resolution N-body simulations. Most often this is taken into account via an effective overall boost factor that multiplies the fluxes. In reality, however, the phenomenological implications of substructure are more complicated than that. Indeed, the intensity and morphology of the DM annihilation signal is highly sensitive to the way the substructure mass function and the subhalo concentration parameters are extrapolated down to several orders of magnitude below the actual resolution of the numerical simulations. As an effect of propagation and, as a consequence, of the different galactic volumes that contribute to the signal at Earth, the boost factor can be energy dependent and is in general different for different species (e.g. positrons vs antiprotons). Moreover, in models in which the DM annihilation rate is enhanced by the Sommerfeld effect there are claims that the contribution from

substructures might outweigh the DM annihilation signal from the smooth main halo alone. The gamma ray signal of DM annihilation from the Galaxy with a simply modeled population of subhalos is presented in [171].
In PPC4DMID DM annihilations (parameterized by the DM DM cross section σv) and decays are considered (described by the DM decay rate $\Gamma = 1/\tau$) into the following primary channels:

$$e^+e^-, \mu^+\mu^-, \tau^+\tau^-$$

$$q\bar{q}, c\bar{c}, b\bar{b}, t\bar{t}, \gamma\gamma, gg$$

$$W^+W^-, ZZ$$

$$hh$$

$$\nu\bar{\nu}$$

$$VV \longrightarrow 4e, 4\mu, 4\tau$$

where q = u,d,s denotes a light quark and h is the Standard Model (SM) Higgs boson, with its mass fixed at 125 GeV [171]. The last three channels denote models in which the annihilation or decay first happens into some new (light) boson V which then decays into a pair of leptons.
The particles produced in Dark Matter annihilation/decay are provided with parton showers and hadronization, in such a way to obtain the fluxes of $e^{\pm}, \bar{p}, \bar{d}, \gamma, \nu(\bar{\nu})$ at the production point. To this goal, the two most widely used Monte Carlo simulation programs are used: Pythia (version 8.135), already used in most DM studies carried out so far, and Herwig (version 6.510). In fact, the algorithms implemented in Herwig and Pythia are quite different, in both parton showers and hadronization, which makes compelling the employment of both codes for the sake of comparing and estimating the Monte Carlo uncertainty on a prediction.
The fluxes of $e^{\pm}, \bar{p}, \bar{d}, \gamma, \nu(\bar{\nu})$ are therefore computed, in a large range of DM masses $M_{DM} = 5$ GeV $\longrightarrow$ 100TeV, by using the Pythia event generator, and provide them in numerical form on the website [166], both in the form of Mathematica interpolating functions and numerical tables. Such computing power demanding results have been obtained using the EU Baltic Grid facilities.
Some specifications on these fluxes are in order. About all fluxes: The fluxes obtained include EW corrections, as discussed above. However, in [166] are provided, for comparison, all the spectra before EW corrections.
About γray fluxes: the fluxes include only the prompt emission and not the secondary radiation (e.g. due to Inverse Compton processes). Furthermore, we must recall that

prompt emission means all photons in final state showers or hadron decays as given by Pythia, including those from (IR-enhanced model independent) QED and EW bremsstrahlung. But further contributions to prompt emission can come from other three body final states such as internal bremsstrahlung: these can only be computed in the framework of a precise DM model because one needs to know the higher order QED annihilation/decay diagram. These are not included.

About fluxes of antideuterons: They are computed taking into account the jet structure of the annihilation products scale with the cube of the uncertain coalescence parameter, fixed to p_0 =160 MeV [173].

About fluxes of neutrinos and anti-neutrinos: The ones provided here are the neutrino spectra at production; the corresponding fluxes at detection are affected by oscillations (if travelling in vacuum, such as for neutrinos from DM annihilations/decays at the Galactic Center) and/or by interactions with matter (if e.g. from DM annihilations/decays in the center of the Sun). The fluxes at detection of neutrinos having traveled in vacuum from a distant astrophysical source can be obtained taking into account average oscillations with the formula

$$P(\nu_l \longrightarrow \nu_{l'}) = P(\bar{\nu_l} \longrightarrow \bar{\nu_{l'}}) = \sum_{i=1}^{3} |V_{li} V_{l'i}|^2 \tag{6.22}$$

where i runs over neutrino mass eigenstates, and the elements $|V_{li}|$ of the neutrino mixing matrix can depend on its unknown CP violating phases. The case of neutrinos from the center of the Sun is more complicated. Finally, we must recall that neutrinos detected after having crossed the Earth can experience additional oscillation effects.

Having at disposal the energy spectra of charged particles per annihilation at production, as generated by MonteCarlos, one next needs to consider where these fluxes of particles are produced in the galactic halo and how they propagate to the Earth.

For simplicity, the propagation formalism for electrons or positrons, for antiprotons and for antideuterons is presented separately. In the latter case, only a few trivial changes have to be implemented with respect to antiprotons.

In general one ends up with a convenient form for the propagated fluxes in terms of a convolution of the spectra at production with a propagation function that encodes all the intervening astrophysics.

One of the final state we are going to analyze is the antiproton flux. The propagation of antiprotons through the galaxy is described by a diffusion equation: the number density of antiprotons per unit energy $f(t, \bar{x}, K) = dN_{\bar{p}}/dK$ vanishes on the surface of the cylinder at $z = \pm L$ and r=R; $K = E - m_p$ is the $\bar{p}$ kinetic energy, conveniently used instead of the total energy E (a distinction which is of course not particularly

relevant when one looks at fluxes originating from TeV scale DM, i.e. at energies much larger than the proton mass m_p, but important for the low energy tails and in the case of small DM masses). The diffusion equation for f can be written as

$$\frac{\partial f}{\partial t} - \kappa(K) \cdot \nabla^2 f + \frac{\partial}{\partial z}(sign(z) f V_{conv}) = Q - 2h\delta(z)(\Gamma_{ann} + \Gamma_{non-ann}) f \qquad (6.23)$$

where

- the pure diffusion term can be written as $\kappa(K) = \kappa_0 \beta (p/GeV)^\delta$, where $p = (K^2 + 2m_p K)^{1/2}$ and $\beta = v_{\bar{p}}/c$ are the antiproton momentum and velocity.
- The V_{conv} term corresponds to a convective wind, assumed to be constant and directed outward from the galactic plane, that tends to push away $\bar{p}$ with energy $E \leq 10\ m_p$.
- Q is the source term due to DM DM annihilations or DM decay and depends on K.
- The first part of the last term describes the annihilations of p^- on interstellar protons in the galactic plane with rate $\Gamma_{ann} = (n_H + 4^{2/3} n_{He}) \sigma^{ann}_{\bar{p}p}$, where n$\simeq 1/cm^3$ is the hydrogen density, n$\simeq$0.07 n is the Helium density and $\sigma^{ann}_{\bar{p}p}$ is given by [174,175]

$$\sigma^{ann}_{\bar{p}p}[mb] = 661(1 + 0,0115 K^{-0,774} - 0,984 K^{0,0151}) \qquad K < 15,5 GeV \quad (6.24)$$

$$\sigma^{ann}_{\bar{p}p}[mb] = 36 K^{-0,5} \qquad K \geq 15,5 GeV \qquad (6.25)$$

  The second part, similarly, describes the interactions on interstellar protons in the galactic plane in which the $\bar{p}$ do not annihilate but lose a significant fraction of their energy. Technically, one should keep them in the flux, with a degraded energy: they are referred to as "tertiary antiprotons". Instead a simplifying approximation is adopted, they are treated as if they were removed from the flux. The cross section associated to the whole last term of equation is then the sum of $\sigma^{inel}_{p\bar{p}} = \sigma^{ann}_{p\bar{p}} + \sigma^{non-ann}_{p\bar{p}}$. It is given in [175] as

$$\sigma^{inel}_{p\bar{p}}(K) = 24,7(1 + 0,584 K^{-0,115} + 0,856 K^{-0,566}) \qquad (6.26)$$

  (at large energies this expression has to be replaced by a better approximation).

- The effect of "tertiary antiprotons" is neglected. It can be reincluded in terms of an absorption term proportional to a different $\sigma^{non-ann}$, and of a reinjection term Q^{tert} proportional to the integrated cross section over f(K). The effect of tertiaries is mainly relevant at low energies K $\leq$ few GeV.

- Finally diffusive reacceleration is not included. It does not play a major role for $\bar{p}$ at the high energies, say larger than tens of GeV. It can instead affect the spectrum at GeV energies, and it can be reintroduced in an effective way by adding an effective energy loss coefficient and/or modifying the energy dependance of the spatial diffusion coefficient.

Assuming again steady state conditions, the first term in the diffusion equation vanishes, and the equation can be solved analytically. In the no tertiaries approximation, the solution for the antiproton differential flux at the position of the Earth $\frac{d\Phi_{\bar{p}}}{dK(K,\bar{r}_{\odot})} = \frac{v_{\bar{p}}}{4\pi f}$ acquires a simple factorized form

$$\frac{d\Phi_{\bar{p}}}{dK(K,\bar{r}_{\odot})} = (\frac{\rho_{\odot}}{M_{DM}})^2 R(K) \sum_f \frac{1}{2} < \sigma v >_f \frac{dN_{\bar{p}}^f}{dK} \qquad annihilation \tag{6.27}$$

$$\frac{d\Phi_{\bar{p}}}{dK(K,\bar{r}_{\odot})} = (\frac{\rho_{\odot}}{M_{DM}}) R(K) \sum_f \Gamma_f \frac{dN_{\bar{p}}^f}{dK} \qquad decay \tag{6.28}$$

The f index runs over all the annihilation channels with antiprotons in the final state, with the respective cross sections or decay rates; this part contains the particle physics input. The function $R(K)$ encodes all the astrophysics of production and propagation. There is such a propagation function for annihilations and for decays for any choice of DM galactic profile and for any choice of set of propagation parameters. $R(K)$ can be written for all these cases in terms of a fit function

$$log_{10}[R(K)/Myr] = a_0 + a_1\kappa + a_2\kappa^2 + a_3\kappa^3 + a_4\kappa^4 + a_5\kappa^5 \tag{6.29}$$

with $\kappa = log_{10}K/GeV$.

Finally, for completeness the average solar modulation effect must be mentioned, although it is mainly relevant for non-relativistic $\bar{p}$: the solar wind decreases the kinetic energy K and momentum p of charged cosmic rays such that the energy spectrum $d\Phi_{\bar{p}\oplus}/dK_{\oplus}$of antiprotons that reach the Earth with energy K and momentum p(sometimes referred to as Top of the Atmosphere 'ToA' fluxes) is approximatively related to their energy spectrum in the interstellar medium, $d\Phi_{\bar{p}}/dK$,

$$\frac{d\Phi_{\bar{p}\oplus}}{dK_{\oplus}} = \frac{p_{\oplus}^2}{p^2}\frac{d\Phi_{\bar{p}}}{dK} \tag{6.30}$$

$$K = K_{\oplus} + Ze\phi_F \tag{6.31}$$

$$p^2 = 2m_pK + K^2 \tag{6.32}$$

The so called Fisk potential ϕ_F parameterizes in this effective formalism the kinetic energy loss. A value of $\phi_F = 0.5$ GV is characteristic of a minimum of the solar cyclic

parameters	values
Halo	NFW, Iso, Bur, Eib, Moo, Ein
Mass $[GeV]$	300, 500, 700, 1000, 1500
Set	MIN,MED,MAX
$\sigma[cm^3 s^{-1}]$	$10^{-23}, 10^{-24}, 10^{-25}, 10^{-26}$

Table 6.18: In table are reported the PPPC4DMID parameters associated to DM production: DM halo profile parameterization, DM mass, propagation scheme and DM thermal annihilation cross section. We assigned the outlined values to the written parameters in a combinatorially way and then compared the results obtained with AMS-02 data.

activity, corresponding to the period in which most of the observations have been done in the second half of the 90s and at the end of the years 2000s. Applying the above described formalism one can obtain resulting fluxes of charged cosmic rays from DM as they would be observed at Earth.
Applying the recipe described above is straightforward to compute the fluxes of antiprotons at Earth, for a given choice of halo profile and propagation parameters.
Corrections for solar modulation aren't considered. It is apparent that the choice of propagation parameters (MIN, MED or MAX) affects in a relevant way the final result, up to a couple of orders of magnitude, even if the spectral shapes are not sensibly modified. The choice of the DM halo profile, instead, has a limited impact and it is barely visible for the decay case. This is already evident of course in the little variations of the halo function and can be traced back to the fact that the decay signal, being proportional to the first power of the DM density, is mainly sensitive to the local DM halo, where the profiles do not differ sensibly.
Using the above functions provided by PPPC4DMID, we repeated the same procedure used for the GALPROP DM simulations, varying all the possible parameters in the allowed range, as outlined in Table 6.18

As for GALPROP also in this case we concentrate the analysis on the $\bar{p}$ flux. In Figure 6.31 some results obtained with PPPC4DMID are shown.

From the results shown in this section, we can infer a qualitative constraint for the dark matter mass: not to be in conflict with the AMS-02 preliminary data, the

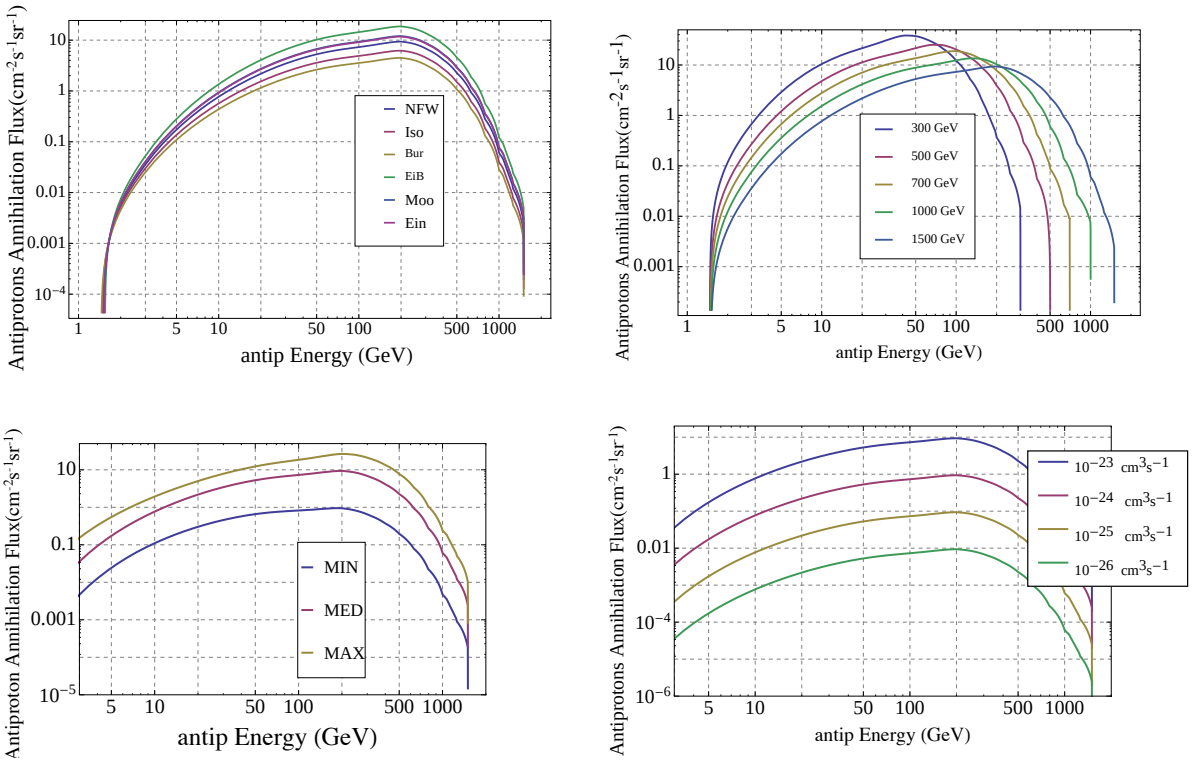

Figure 6.31: In these figures we show how DM parameters can be varied in PPPC4DMID. Starting from a default set of values for the DM parameter (Navarro-Frank-White halo profile, MED propagation set, $\sigma = 10^{-3} cm^3 s^{-1}$ and a 1500 Gev mass) we varied a fixed parameter according to the values reported in Table 6.18. The upper left plot shows the possible DM halo profiles, in the upper right plot DM masses are shown, in the lower right plot we can observe the possible propagation sets and finally the lower right plot shows the possibile thermal cross section for DM annihilation.

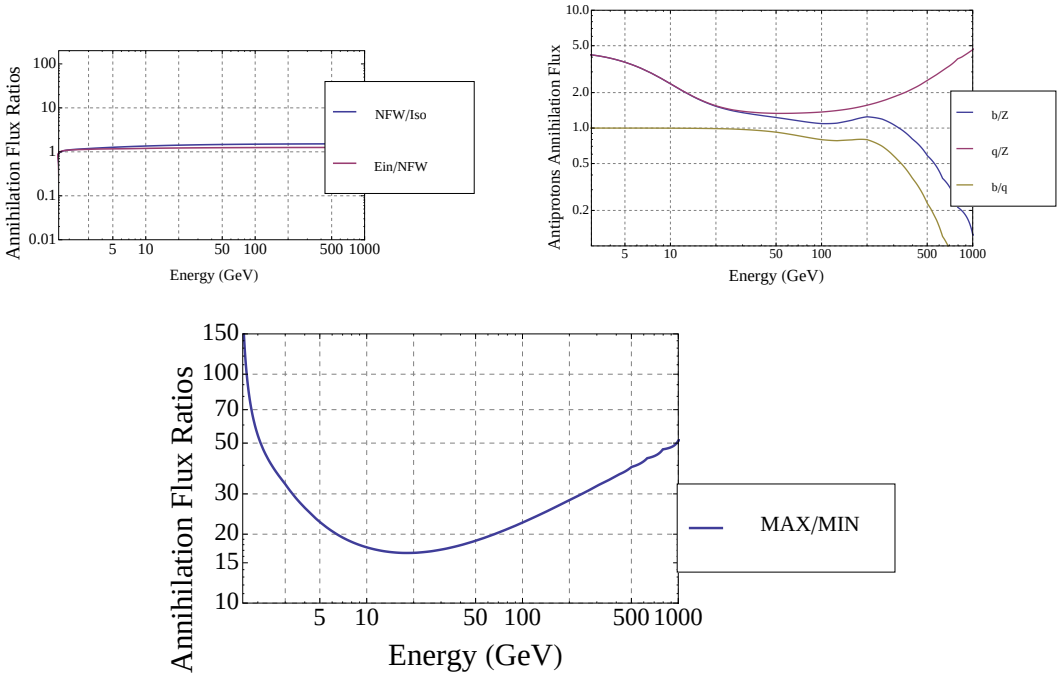

Figure 6.32: Comparison between different parameter ratios associated to DM production in PPPC4DMID: DM halo profile ratio (upper left plot), DM annihilation channel ratio (upper right plot) and propagation set ratio (lower plot). From these plots we can conclude that the uncertainties related both to DM halo profile and DM annihilation channel are quite small, contrary the most relevant uncertainty is the one associated to the propagation set considered: we are able to reduce it by an average factor of about 50, as we can see from the lower plot reported in figure, where an energy range up to 1000 GeV is considered.

mass must be heavier than 0,5 TeV (Fig.6.30 lower right). Moreover we showed how different DM physical conditions, such as halo and cross section, can produce useful signal for DM indirect detection in different possible channels. Finally, observing the propagation set ratio (Fig.6.32 lower plot), the annihilation channel ratios (Fig.6.32 upper right plot) and the halo profile ratios (upper left plot), we can notice that the uncertainties related both to DM halo profile and DM annihilation channel are quite small, the most relevant uncertainty is the one coming from astrophysics and associated to the propagation set, this is the most difficult to remove. Nevertheless we are able to reduce this uncertainty by an average factor of about 50, as we can see from Figure 6.32 (lower plot).

Chapter 7

Conclusion

The Alpha Magnetic Spectrometer (AMS-02) installed aboard of the International Space Station is properly acquiring data from May 19th 2011. AMS-02 gives unique opportunities for the primary cosmic radiation study up to TeV energy range, along with the possible observation of dark matter indirect signals. In this work, after a brief description of the origin and propagation of cosmic rays, explained using different possible models, we focused on the description of the main dark matter properties: according to the here presented models, DM should be a supersymmetric particle or a Kaluza-Klein particle or a particle as the ones presented in the Little Higgs and in the Scalar Singlet models, with a Tev-ish mass. These particles could be able to produce an enhancement in antiparticle fluxes such as positrons and antiprotons. The 1 TeV energy scale defined above is exactly the AMS-02 research window, so that AMS-02 will be able to put some constraints on dark matter parameters such as annihilation cross section, annihilation channels and the mass range, using the measurements obtained from nuclei ratios and fluxes and finally using these results to exclude or corroborate previously described DM models. In chapter 6 we deal with CR nuclei fluxes and ratios, describing the procedure used to select a parameter set for the CR propagation with the Galprop software. Moreover we analyzed the non astrophysical uncertainties, such as primary abundances at source, nuclear cross sections and solar modulation: precisely taking into account these uncertainties can improve the GALPROP fitting procedure of AMS-02 preliminary data. Finally in the last section, we showed how one can use the results obtained with the best fit Galprop simulation to predict dark matter signals, studying the antiproton over proton ratio and the antiproton flux. We want here to underline that the aim of the study done at the beginning of this work, focused on the selection of a propagation set for CR, was not only related to the possibility of fixing some values for propagation parameters, but was done also to the aim of

use this result for DM indirect search: indeed as already discussed, the main indirect search channel is related to an excess in $e^+, \bar{p}$ fluxes and their related ratios, a good knowledge of the processes these particles undergo during their propagation, can help us to obtain their final spectra. This study was done using not only Galprop but also a second software that is PPPC4DMID: for the simulation we used different annhilation channels and masses along with halo profile and cross sections. Finally we compared the results obtained with the two software showing how one can use the preliminary AMS-02 data to reject or accept some DM parameter values. To further improve the propagation set here adopted and to better fix DM constraints, new AMS-02 data in the high energy region could be useful, along with the reduction of the high energy measurements error bars. Nevertheless we want here to notice that great improvements were done in CR physics: AMS-02 data have an unprecedent resolution and binning with respect to previous exeperiments, such as CREAM and ATIC, as shown in Figure 7.1 [178].

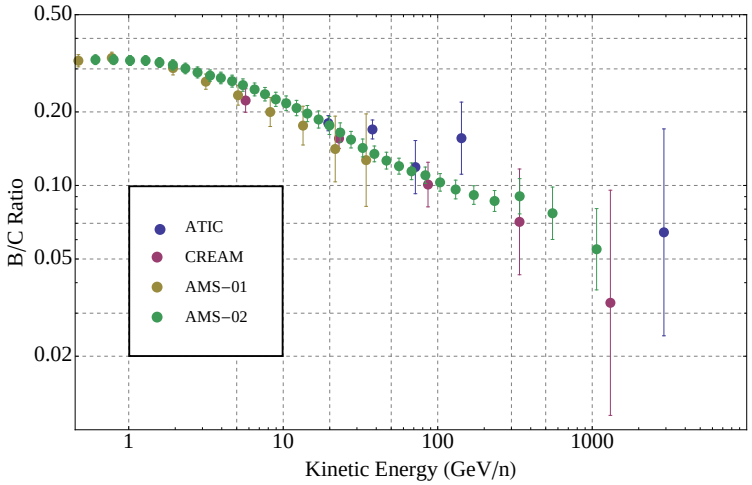

Figure 7.1: *The Boron over Carbon ratio as a function of kinetic energy. Previous measurements from ATIC, CREAM and AMS-01 are shown along with the AMS-02 data.*

Bibliography

[1] F. Giovacchini, *Cosmic Rays Anti-Deuteron Flux Sensitivity of the AMS-02 Detector*, Thesis, 2007

[2] G. Carminati, *Study of diffuse flux of high energy neutrinos through showers with the ANTARES neutrino telescope*, Thesis, 2010

[3] D. Lynden-Bell, *Galactic Nuclei as Collapsed Old Quasars*, Nature **223** 690-694, 1969

[4] T. Stanev, *High Energy Cosmic Rays*, Springer, 2002

[5] CERN website, *http://home.web.cern.ch/about/physics/cosmic-rays-particles-outer-space*

[6] T.K. Gaisser, *Cosmic Rays and Particle Physics*, Cambridge University Press, 1990

[7] G. Jungman et al., *Supersymmetric Dark Matter*, Phys. Rep. **267**, 2006

[8] E.N. Parker, *The Passage of Energetic Charged Particles through Interplanetary Space*, Planet. Space. Sci. **13**, 1965

[9] A.M. Hillas, *Comsic Rays: Recent Progress and some Current Questions*, arXiv:astro-ph/0607109, 2006

[10] C. Amsler et al., *Review of particle physics*, Phys. Lett. B **667**, 2008

[11] V.S. Berezinsky et al., *Astrophysics of Cosmic Rays*, North-Holland, 1990

[12] J.A. Simpson et al., *Cosmic-Ray 26Al and Its Decay in the Galaxy*, Ap. J. **497** L85, 1998

[13] V.L. Ginzburg et al., *Cosmic ray astrophysics (history and general review)*, Phys-Usp **39** 2 155,1996

[14] M.S. Longair, *High Energy Astrophysics*, Cambridge University Press, 1993

[15] E. Fermi, *On the Origin of the Cosmic Radiation*, Phys. Rev. **75** 1169, 1949

[16] V.L. Ginzburg et al., *The Origin of Cosmic Rays*, Macmillan, 1964

[17] M. Simon, *The interpretation of radioactive isotopes in the cosmic radiation and the link between the diffusion halo model and the leaky box model*, Frascati Physics Series **29** 119-136, 2002

[18] A.W. Strong et al., *Propagation of Cosmic-Ray Nucleons in the Galaxy*, Ap. J. **509** 212, 1998

[19] D. Maurin et al., *Cosmic Rays below Z=30 in a Diffusion Model: New Constraints on Propagation Parameters*, Ap.J. **555** 585, 2001

[20] D. Maurin et al., *New results on source and diffusion spectral features of Galactic cosmic rays: B/C ratio*, A&A **394** 1039, 2002

[21] W.R. Webber et al., *Total charge and mass changing cross sections of relativistic nuclei in hydrogen, helium and carbon targets*, Phys. Rev. C **41** 520, 1990

[22] U. Heinbach et al., *Propagation of Galactic Cosmic Rays under Diffusive Reacceleration*, Ap. J. **441** 209, 1995

[23] S.A. Stephens et al., *Models of Galactic cosmic-ray propagation*, Ap. J. **505** 266-277, 1998

[24] F.C. Jones, *Examination of the 'leakage-lifetime' approximation in cosmic-ray diffusion*, Phys. Rev. **2** 2787, 1970

[25] D. Grasso et al., *CR electrons and positrons: what we have learned in the latest three years and future perspectives*, arXiv:1110.6626v2, 2011

[26] A. W. Strong et al., *Galprop explanatory supplement*, 2011

[27] M. Perelstein et al., *Remarks on calculation of positron flux from galactic dark matter*, Phys. Rev. D **82** 043505, 2010

[28] F. Donato et al., *Galactic Cosmic Ray Nuclei as a Tool for Astroparticle Physics*, arXiv:astro-ph/0212111, 2002

[29] J. W. Mitchell et al., *Precise measurements of the cosmic ray antiproton spectrum with BESS including the effects of solar modulation*, A.S.R **35** 1 135-141, 2005

[30] M. Boezio et al., *The cosmic-ray antiproton flux between 0.62 and 3.19 GeV measured near solar minimum activity*, Ap. J. **487** 415, 1997

[31] P. Bobik et al., *Proton and antiproton modulation in the heliosphere for different solar conditions and AMS-02 Measurements Prediction*, arXiv:1012.3086, 2010

[32] D. Grandi, *A tracing model for the Earth magnetosphere: the effect on Cosmic Ray access to a space detector*, Thesis

[33] M. Duranti, *Measurement of the Atmospheric Muon Flux on Ground with the AMS-02 Detector*, Thesis

[34] D.F. Smart, *A review of geomagnetic cutoff rigidities for earth-orbiting spacecraft*, A.S.R. **36** 10 2012–2020, 2005

[35] D.F. Smart et al., *A study of vertical cutoff rigidities using sith degree simulations of geomagnetic field*, J. Geophys. Res. **70** 4117, 1965

[36] C.Z. Stormer, *The Polar Aurora*, Oxford University Press, 1955

[37] N. Olsen et al., *Orsted initial field model*, Geophys. Res. Lett. **27** 3607, 2000

[38] N. Masi, *The Dark Matter Search. The AMS-02 Experiment*, Lambert Academic Publishing-Berlin, 2013

[39] C. Nipoti, *http://urania.bo.astro.it/nipoti/didattica/astrofisica*

[40] S. Weinberg, *Gravitation and Cosmology: Principles and Applications of the General Theory of Relativity*, Wiley, 1972

[41] S. Perlmutter et al., *Measurements of* Ω *and* Λ *from 42 high redshift supernovae*, Ap. J. **517** 565-586, 1999

[42] A.G. Riess et al., *Observational evidence from supernovae for an accelerating Universe and a cosmological constant*, Ap. J. **116** 1009-1038, 1998

[43] S. Weinberg, *The Quantum Theory of Fields*, Cambridge University Press, 1996

[44] G. Bertone, *Particle Dark Matter: Observations, Models and Searches*, Cambridge University Press, 2010

[45] J.L. Feng, *Dark Matter Candidates from Particle Physics and Methods of Detection*, arXiv:1003.0904, 2010

[46] P.D. Serpico, *Astrophysical models for the origin of the positron "excess"*, Ap. Phys. **39,40** 2–11, 2011

[47] F. Sannino et al., *Technicolor dark matter*, Phys. Rev. D **80** 037702, 2009

[48] F. Sannino et al., *Ultra Minimal Technicolor and its Dark Matter TIMP*, arXiv:0809.0713, 2008

[49] F. Sannino et al., *Dark Matter from new Technicolor Theories*, Phys.Rev. D **74** 095008, 2006

[50] S. Tulin et al., *Hylogenesis: A Unified Origin for Baryonic Visible Matter and Antibaryonic Dark Matter*, Phys.Rev.Lett. **105** 211304, 2010

[51] L. Papantonopoulos, *The Invisible Universe Dark Matter and Dark Energy*, Springer, 2007

[52] J. Terning, *Modern Supersymmetry; Dynamics and Duality*, Oxford University Press, 2006

[53] B.S. Acharya et al., *Non-thermal dark matter and the moduli problem in string frameworks*, J. Hep. **06** 064, 2008

[54] A. Masiero et al., *Neutralino Dark Matter Detection in Split Supersymmetry Scenarios*, Nuc. Phys. B **712** 1–2 86–114, 2004

[55] J. Olzem, *Signatures of SUSY Dark Matter at the LHC and in the Spectra of Cosmic Rays*, arXiv:0704.3943, 2007

[56] S.P. Martin, *A Supersymmetry Primer*, arXiv:hep-ph/9709356, 1997

[57] L. Randall et al., *General Analysis of Antideuteron Searches for Dark Matter*, arXiv:1006.0983, 2010

[58] G. Bertone et al., *Particle Dark Matter Evidence, Candidates and Constraints*, arXiv:hep-ph/0404175, 2004

[59] H.C. Cheng, *Kaluza-Klein Dark Matter*, Phys. Rev. **89** 21, 2002

[60] G. Servant et al., *Is the lightest Kaluza-Klein particle a viable dark matter candidate?*, Nuc. Phys B **650** 391-419, 2003

[61] D. Hooper et al., *Kaluza-Klein dark matter and the positron excess*, Phys. Rev. D **70** 115004, 2004

[62] K. Cheung et al., *Cosmic positron and antiproton constraints on the gauge-Higgs Dark Matter*, arXiv:1007.0282, 2010

[63] D. Hooper et al., *The PAMELA and ATIC Signals From Kaluza-Klein Dark Matter*, arXiv:0902.0593, 2009

[64] C.R. Chen et al., *Kaluza-Klein Dark Matter After Fermi*, arXiv:0908.4317, 2009

[65] G. Belanger et al., *Dirac Neutrino Dark Matter*, doi:10.1088/1475-7516/2008/01/009, 2007

[66] K. Kadota et al., *Heavy Right-Handed Neutrinos and Dark Matter in the νCMSSM*, arXiv:0909.3075, 2009

[67] K. Agashe et al., *Warped Unification, Proton Stability and Dark Matter*, Phys. Rev. Lett. **93** 231805, 2004

[68] G. Servant et al., *Baryon Number in Warped GUTs*, arXiv:hep-ph/0411254, 2004

[69] M. Perelstein, *Little Higgs Models and their Phenomenology*, Prog. Part. and Nuc. Phys. **58** 1 247–291, 2005

[70] M. Schmaltz et al., *Little Higgs review*, arXiv:hep-ph/0502182, 2005

[71] D. Tseliakhovich, *Dark Matter in the Little Higgs Models*, Carleton University, 2008

[72] M. Perelstein et al., *Indirect Detection of Little Higgs Dark Matter*, Phys. Rev. D **75** 083519, 2007

[73] M. Asano, *Cosmic Positron Signature from Dark Matter in the Littlest Higgs Model with T-parity*, arXiv:hep-ph/0602157, 2006

[74] S. Dodelson et al., *Sterile Neutrinos as Dark Matter*, arXiv:hep-ph/9303287, 1993

[75] K. Abazajian, *Production and Evolution of Perturbations of Sterile Neutrino Dark Matter*, Phys. Rev. D **73** 063506, 2006

[76] J.T. Ruderman et al., *General Neutralino NLSP at the Early LHC*, arXiv:1103.6083, 2011

[77] T. Han et al., *Higgs sector in a U(1) extension of the minimal supersymmetric standard model* Phys. Rev. D **70** 115006, 2004

[78] T. Delahaye et al., *Cosmic-ray antiproton constraints on light singlino-like dark matter candidates*, arXiv:1108.1128, 2011

[79] A. Barrau et al., *Antideuterons as a probe of primordial BH*, arXiv:astro-ph/0207395, 2002

[80] P.H. Frampton, *Looking for Intermediate-Mass Black Holes*, arXiv:0907.1646, 2009

[81] G. Boudoul et al., *Some aspects of primordial black hole physics*, arXiv:astro-ph/0212225, 2002

[82] A.L. Chavda et al., *Ultra High Energy Cosmic Rays from decay of Holeums in Galactic Halos*, arXiv:0806.0454, 2008

[83] L.K. Chavda et al., *Dark matter and stable bound states of primordial black holes*, arXiv:gr-qc/0308054, 2003

[84] L.K. Chavda et al., *Black hole immunity theorem and dark matter*, arXiv:physics/0406159, 2004

[85] R.H. Sanders, *The Dark Matter Problem: A Historical Perspective*, Cambridge University Press, 2010

[86] O. Adriani et al., *New Measurement of the Antiproton-to-Proton Flux Ratio up to 100 GeV in the Cosmic Radiation*, Phys. Rev. Lett. **102** 051101, 2009

[87] V. Bindi, A. Contin, N. Masi, L. Quadrani, F. Palmonari et al., *The AMS-02 time of flight (TOF) system: construction and overall performances in space*, Proc. 33rd ICRC, 2013

[88] V. Bindi, A. Contin, N. Masi, L. Quadrani, F. Palmonari et al., *First Result from the Alpha Magnetic Spectrometer on the International Space Station:Precision Measurement of the Positron Fraction in Primary Cosmic Rays of 0.5–350 GeV*, Phys. Rev. Lett. **110** 141102, 2013

[89] V. Bindi, A. Contin, N. Masi, A. Oliva, F. Palmonari, L. Quadrani, A. Tiseni, *The time of flight detector of the AMS-02 experiment on the international space station*, Nuc. Instr. Meth. A **718**, 2013

[90] A. Basili, V. Bindi, D. Casadei, G. Castellini, A. Contin, A. Kounine, M. Lolli, F. Palmonari, L. Quadrani, *The TOF-ACC flight electronics for the fast trigger and*

time of flight of the AMS-02 cosmic ray spectrometer, Nuc. Instr. Meth. A **707**, 2013

[91] F. Palmonari, V. Bindi, A. Contin, N. Masi and L. Quadrani, *Search for Dark Matter in Cosmic Rays with the AMS-02 space spectrometer*, doi:10.1088/1742-6596/335/1/012066, 2011

[92] V. Bindi, D. Casadei, G. Castellini, F. Cindolo, A. Contin, F. Giovacchini, C. Guandalini, G. Laurenti, G. Levi, M. Lolli, L. Quadrani, F. Palmonari, C. Sbarra, A. Zichichi, *The scintillator detector for the fast trigger and time of flight (TOF) measurement of the space experiment AMS-02* Nuc. Instr. Meth. A **623** 968 - 981, 2010

[93] V. Bindi, *The alpha magnetic spectrometer AMS-02: Soon in space* Nucl. Instr. Meth. A **617** 462-463, 2010

[94] F. Palmonari, *The search for Cosmic Antimatter* Il Nuovo Saggiatore **25** 1-2 13-23, 2009

[95] A. Tiseni, *Misura del Rate di Protoni con AMS-02*, Thesis, 2012

[96] L. Quadrani, *Assembly and space qualification of the scintillator detector LTOF for the AMS-02 spectrometer*, Thesis, 2007

[97] V. Bindi, *Development and performances of the SFEC card for the TOF apparatus*, Thesis, 2006

[98] AMS-02 website, *http://www.ams02.org/what-is-ams/tecnology/*

[99] L. Arruda et al., *Particle identification with the AMS-02 RICH detector search for dark matter with antideuterons*, arXiv:0710.0993, 2007

[100] V. Vagelli, *Identification of positrons and electrons in the cosmic radiation with the electromagnetic calorimeter ECAL for the AMS-02 experiment*, Thesis, 2011

[101] C. Sbarra, *Astroparticle Physics with AMS-02*, 2005

[102] W.R. Leo, *Techniques for Nuclear and Particle Physics Experiments*, Springer, 1983

[103] K. Kleinknecht, *Detectors for Particle Radiation*, Cambridge University Press, 1998

[104] P. Von Doetinchem et al., *Performance of the AMS-02 Transition Radiation Detector*, Nuc. Instr. Meth. **558** 2 526–535, 2006

[105] A. Lebedev, *The AMS-02 electronics system*, 29th ICRC, 2005

[106] J.B. Birks, *The theory and practice of Scintillation Counting*, Pergamon Press, 1964

[107] M. Pato, *Pinpointing Cosmic Ray Propagation With The AMS-02 Experiment*, doi:10.1088/1475-7516/2010/06/022, 2010

[108] M.Pato *Propagation of galactic cosmic ray and the AMS-02 experiment*, 29th ICRC 3 5356, 2008

[109] F. Spada, *Antimatter and Dark Matter search in space with AMS-02*, 2008

[110] K. Lübelsmeyer et al., *Upgrade of the Alpha Magnetic Spectrometer (AMS-02) for long term operation on the International Space Station (ISS)*, NIM A **654** 639-648, 2011

[111] J. Alcaraz et al., *The alpha magnetic spectrometer silicon tracker: Performance results with protons and helium nuclei*, NIM A **593** 376-398, 2008

[112] B. Alpat et al., *The internal alignment and position resolution of the AMS-02 silicon tracker determined with cosmic-ray muons*, NIM A **613** 207-217, 2010

[113] F. Cadoux et al., *The AMS-02 electromagnetic calorimeter*, Nuc. Phys. B **113** 159, 2002

[114] Th. Kirn et al., *The AMS-02 TRD: a detector designed for space*, Bari Workshop, 2001

[115] T. Bruch et al., *The Anti-Coincidence Counter shield of the AMS tracker*, NIM A **572** 505-507, 2007

[116] V. Bindi et al., *Time of flight readout system of the AMS-02 experiment* 29th ICRC, 2005

[117] L. Quadrani et al., *Optimization of time of flight of the AMS-02 experiment*, 29th ICRC, 2005

[118] R. Martelli, *Studio e simulazione delle caratteristiche dei fotomoltiplicatori "fine-mesh" per l'esperimento spaziale AMS-02*, Thesis, 2002

[119] A.W. Strong et al., *Diffuse Galactic Continuum Gamma Rays: A Model Compatible with EGRET Data and Cosmic-Ray Measurements*, Ap. J. **613** 956, 2004

[120] A.W. Strong et al., *A new determination of the extragalactis diffuse gamma-ray background from EGRET data*, Ap. J. **613** 962, 2004

[121] A.W. Strong et al., *The distribution of cosmic-ray sources in the Galaxy, γ-rays and the gradient in the CO-to-H_2 relation*, A&A **422** L47, 2004

[122] A.W. Strong et al., *Cosmic-ray propagation and interactions in the galaxy*, Ann. Rev. Nucl. Part. Sci. **57** 285, 2007

[123] A.W. Strong et al., *The GALPROP Cosmic-Ray Propagation Code*, Proc. 31st ICRC, 2009

[124] A.E. Vladimirov et al., *GALPROP WebRun: an internet-based service for calculating galactic cosmic ray propagation and associated photon emission*, arXiv:1008.3642, 2010

[125] K.Z. Stanek et al., *Distance to M31 with the Hubble Space Telescope and Hipparcos Red Clump Stars*, Ap. J. **503** L131, 1998

[126] D.R. Alves, *K-Band Calibration of the Red Clump Luminosity*, Ap. J. **539** 732, 2000

[127] A. Lukasiak et al., *The isotopic composition of cosmic-ray beryllium and its implication for the cosmic ray's age*, Ap. J. **423** 426, 1994

[128] M.A. Gordon et al., *The radial distribution of CO, H_2, and nucleons*, Ap. J. **208** 346, 1976

[129] P. Cox et al., *Principal heating sources of dust in the galactic disk*, A& A **155** 380, 1986

[130] M. Prouza et al., *The Galactic magnetic field and propagation of ultra-high energy cosmic rays*, arXiv:astro-ph/0307165, 2003

[131] N. Grevesse et al., *Standard Abundances*, ASP Conf. Series **99** 117, 1996

[132] C. Heiles, *Turbulence and Magnetic Fields in Astrophysics*, Ap. J. **462** 316, 1996

[133] D.S. Mathewson et al., *Polarization observations of 1800 stars*, Royal Astronomical Society, 1970

[134] A.W. Strong et al., *GALPROP Explanatory Supplement*, 2014

[135] V.S. Ptuskin et al., *Transport of relativistic nucleons in a galactic wind driven by cosmic rays*, A&A **321** 434, 1997

[136] J. Cordes et al., *The galactic distribution of free electrons*, Nature **354** 121, 1991

[137] S. Matarrese et al., *Dark Matter and Dark Energy: A Challenge for Modern Cosmology*, Springer, 2011

[138] E.S. Seo et al., *Stochastic reacceleration of cosmic rays in the interstellar medium*, Ap. J. **431** 705, 1994

[139] A. W. Strong et al., *Gradient model analysis of EGRET diffuse Galactic emission*, A&A Lett. **308** L21, 1996

[140] G.R. Farrar, *The Galactic magnetic field and ultrahigh-energy cosmic ray deflections*, doi:10.1016/j.crhy.2014.04.002, 2014

[141] J.P. Vallee, *Observations of the Magnetic Fields inside and outside the Milky Way, starting with Globules ($\simeq$1 parsec), Filaments, Clouds, SuperBubbles, Spiral Arms, Galaxies, Superclusters, and ending with the Cosmological Universe's Background Surface (at $\simeq$8 Teraparsecs)*, Fund. Cosmic Phys. **19** 1, 1996

[142] M. Cirelli et al., *PPPC 4 DM ID: A Poor Particle Physicist Cookbook for Dark Matter Indirect Detection*, arXiv:1012.4515, 2012

[143] M.C. Beck et al., *A new prescription for the random magnetic field of the Milky Way*, arXiv:1409.5120, 2014

[144] G. Bertone, *Gamma-Ray Constraint on Galactic Positron Production by MeV Dark Matter*, Phys. Rept. **405** 279, 2005

[145] J. Einasto, *Dark Matter*, arXiv:0901.0632, 2009

[146] F. Zwicky, *Cosmic rays from supernovae*, Phys. Acta **6** 110, 1933

[147] R. Massey et al., *Dark matter maps reveal cosmic scaffolding*, Nature **445** 286, 2007

[148] D. Clowe, *A direct empirical proof of the existence of dark matter*, Ap. J. **648** L109, 2006

[149] E. Komatsu et al., *Bullet cluster: a challenge to ΛCDM cosmology*, arXiv:1001.4538, 2010

[150] J.E. Gunn et al., *Some astrophysical consequences of the existence of a heavy stable neutral lepton*, Ap. J. **223** 1015, 1978

[151] F.W. Stecker, *Gamma ray constraint on dark matter reconsidered*, Ap. J. **223** 1032, 1978

[152] Y.B. Zeldovich et al., *Searching for TeV dark matter by atmospherical Cherenkov techniques*, Nucl. Phys. **31** 664, 1980

[153] J.R. Ellis et al., *Cosmic ray constraint on the annihilation of relic particles in the galactic halo*, Phys. Lett. B **214** 403, 1988

[154] J. Silk et al., *High-energy neutrinos from the Sun and cold dark matter*, Phys. Rev. Lett. **53** 624, 1984

[155] F.W. Stecker et al., *Galactic Antiprotons from Photinos*, Phys. Rev. Lett. **55** 2622, 1985

[156] S. Rudaz et al., *Some astrophysical consequences of the existence of a heavy stable neutral lepton*, Ap. J. **325** 16, 1988

[157] M.S. Turner et al., *Positron line radiation as a signature of particle dark matter in the halo*, Phys. Rev. D **42** 1001, 1990

[158] F. Donato et al., *Antideuterons as a signature of supersymmetric dark matter*, Phys. Rev. D **62** 043003, 2000

[159] H. Baer et al., *Collider and dark matter seraches in models with modulus-anomaly mediated SUSY breaking*, JCAP 0512 008, 2006

[160] F. Donato et al., *Constraints on WIMP Dark Matter from the High Energy PAMELA $\bar{p}/p$ data*, Phys. Rev. D **78** 043506, 2008

[161] V.S. Berezinsky et al., *High Energy Gamma-Radiation from the Galactic Center due to Neutralino Annihilation*, Phys. Lett. B **325** 136, 1994

[162] P. Gondolo, *Either neutralino dark matter or cuspy dark halos*, Phys. Lett. B **494** 181, 2000

[163] G. Bertone et al., *Gamma-ray and radio tests of the $e^{\pm}$ excess from DM annihilation*, MNRAS **326** 799, 2001

[164] R. Aloisio et al., *Neutralino Annihilation at the Galactic Ceneter Revisited*, arXiv:astro-ph/0402588, 2004

[165] L. Bergstrom et al., *Spectral gamma-ray signatures of cosmological dark matter annihilations*, Phys. Rev. Lett. **87** 251301, 2001

[166] PPPC-4-DM-ID website, *www.marcocirelli.net/PPPC4DMID.html*

[167] A.W. Graham et al., *Empirical Models for Dark Matter Halos. Nonparametric Construction of Density Profiles and Comparison with Parametric Models*, Astron. J. **132** 2685, 2006

[168] J.F. Navarro et al., *The Diversity and Similarity of Simulated Cold Dark Matter Halos*, arXiv:0810.1522, 2008

[169] J. Diemand et al., *Convergence and scatter of cluster density profiles*, arXiv:astro-ph/0402267, 2004

[170] G. Hutsi et al., *Implications of the Fermi-LAT diffuse gamma-ray measurements on annihilating or decaying Dark Matter*, arXiv:1004.2036, 2010

[171] The ATLAS Collaboration, *Observation of a new particle in the search for the Standard Model Higgs boson with the ATLAS detector at the LHC*, arXiv:1207.7214, 2012

[172] The CMS Collaboration, *Observation of a new boson at a mass of 125 GeV with the CMS experiment at LHC*, arXiv:1207.7235, 2012

[173] M. Kadastik et al., *Enhanced anti-deuteron Dark Matter signal and the implications of Pamela*, Phys. Lett. B **683** 248, 2010

[174] L.C. Tan et al., *Calculation of the equilibrium antiproton spectrum*, J. Phys. G **9** 227, 1983

[175] J. Hisano et al., *Heavy wino-like neutralino dark matter annihilation into antiparticles*, Phys. Rev. D **73** 055004, 2006

[176] M. Kachelrieβ et al. *B/C ratio and the PAMELA positron excess*, Phys.Rev. D **87** 047301, 2013

[177] A. Obermeier et al., *Galactic propagation of cosmic rays and the B/C ratio*, 32nd ICRC, 2011

[178] N. Tomassetti, *Measurement of the Cosmic Ray B/C Ratio with the AMS-01 Experiment*, arXiv:1009.1908, 2010

[179] L. Visinelli et al., *Axion cold dark matter in view of BICEP2 results*, arXiv:1403.4594v2, 2014

[180] D.J.E. Marsh et al., *Tensor Detection Severely Constrains Axion Dark Matter*, arXiv:1403.4216v3, 2014

[181] P.A.R. Ade et al., *Planck 2013 results. XVI. Cosmological parameters*, , 2013

[182] Sito internet, www.universe-review.com

[183] NASA web page, www.nasa.gov

[184] Sito internet, www.astronomia.com

[185] Sito internet, www.ishtar.df.unibo.it

[186] A. Morselli, *GALPROP Tutorial*, 2008

[187] N. Tomassetti, *Measurement of the B/C Ratio in Cosmic Rays with the AMS-01 Experiment*, Thesis, 2008

[188] Sito internet, www.accms04.physik.rwth-aachen.de

[189] E. Orazi, *GALPROP Tutorial*, 2006